NUMERICAL MODELS OF STARBURST GALAXIES: GALACTIC WINDS AND ENTRAINED GAS

Ryan Tanner

A dissertation submitted to the faculty at the University of North Carolina at Chapel Hill in partial fulfillment of the requirements for the degree of Doctor of Philosophy in the Department of Physics and Astronomy.

Chapel Hill
2016

Approved by:

Gerald Cecil

Fabian Heitsch

Charles Evans

Daniel Reichart

Christian Iliadis

ABSTRACT

Ryan Tanner: Numerical Models of Starburst Galaxies: Galactic Winds and Entrained Gas
(Under the direction of Gerald Cecil)

My three-dimensional hydro-dynamical simulations of starbursts examine the formation of starburst-driven superbubbles over a range of driving luminosities and mass loadings that determine superbubble growth and wind velocity; floors of both 10 and 10^4 K are considered. From this I determine the relationship between the velocity of a galactic wind and the characteristics of the starburst. I find a threshold for the formation of a wind, above which the wind speed is not affected by grid resolution or the temperature floor of the radiative cooling employed. Optically bright filaments form at the edge of merging superbubbles, or where a cold dense cloud has been disrupted by the wind. Filaments formed by merging superbubbles will persist and grow to > 400 pc in length if anchored to and fed from a star forming complex. For galaxies viewed edge on I use total emission from the superbubble to infer the wind velocity and starburst properties such as thermalization efficiency and mass loading factor. Using synthetic absorption profiles I probe different temperature regimes and measure the velocity of the cold, warm and hot gas phases. I find that the cold and warm gas entrained in the wind move at a much lower velocity than the hot gas, with some of the cold gas in the filaments hardly moving with respect to the galaxy. The absorption profiles show that the velocity of the hot galactic outflow does not depend on the star formation rate (SFR), but the velocity of the warm gas does. The velocity of the warm gas scales as SFR^{δ} until the wind velocity reaches 80% of the analytic terminal wind speed. The value of δ depends on the atomic ionization with a lower value for low ionization, and a higher value for higher ionization.

PREFACE

My intention when I started this was to have a summer project, and then later find something to study for my dissertation. But what was supposed to be short foray into starburst simulations turned into several years of working, reading, and generally failing to fix my code. I estimate that I have used somewhere around 250 years worth of computation time with very little of that actually making it into the finished product. So what is presented here represents many failures, false starts and, quite frankly, mistakes on my part to produce viable research. I have learned a lot, but mostly I have learned what I do not know.

I wish to thank Gerald Cecil who was not satisfied with giving me a "summer" project, but handed me something that ultimately became this dissertation. I also wish to thank Fabian Heitsch for putting up with me and never giving up on that one annoying grad student who managed to make every mistake in the book and never seemed to understand what he was doing.

I am especially grateful to my wife Marcelaine and my children, Kevin, Heidi and Ann Marie.

"The earth rolls upon her wings, and the sun giveth his light by day, and the moon giveth her light by night, and the stars also give their light, as they roll upon their wings in their glory, in the midst of the power of God. Unto what shall I liken these kingdoms, that ye may understand? Behold, all these are kingdoms, and any man who hath seen any or the least of these hath seen God moving in his majesty and power." - Joseph Smith

TABLE OF CONTENTS

LIST OF TABLES

LIST OF FIGURES

LIST OF ABBREVIATIONS AND SYMBOLS

CSF	Continuous Star Formation
FWHM	Full width half maximum
HWHM	Half width half maximum
IR	Infrared
kpc	Kiloparsec
pc	Parsec
SIB	Single Instantaneous Burst
SFR	Star Formation Rate
SMR	Static Mesh Refinement
SN	Supernova
ULIG	Ultra luminous infrared galaxies
UV	Ultraviolet
$n_{\rm halo}(0,0)$	Central halo density
$n_{\rm disk}(0,0)$	Average density in starburst
$T_{\rm halo}$	Halo temperature
$T_{\rm disk}$	Average disk temperature
σ_t	Turbulence parameter for disk
$e_{\rm disk}$	Rotation ratio (disk)
$e_{\rm halo}$	Rotation ratio (halo)
$R_{\rm sb}$	Starburst radius
$H_{\rm sb}$	Starburst height
$\Phi_{\rm disk}(r,z)$	Gravitational potential of the galactic disk

$\Phi_{\rm SS}(r,z)$	Gravitational potential of the stellar bulge
$\Phi_{\rm tot}(r,z)$	Total stellar gravitational potential
$\mathcal{L}$	Total radiative energy rate
Γ	Radiative heating rate
Λ	Radiative cooling rate
$P(r,z)$	Gas pressure
G	Newton's gravitational constant
$v_\phi(r,z)$	Azimuthal velocity
$M_{\rm ss}$	Stellar spheroid mass
$M_{\rm disk}$	Stellar disk mass
$M_\star$	Stellar mass
r_0	Stellar spheroid radial scale size
a	Disk radial scale size
b	Disk scale size
$z_{\rm rot}$	Rotational scale height
v_A	Analytic wind velocity
v_w	Actual wind velocity
ξ	Wind scaling factor
$\dot{E}$	Total energy injection rate
$\dot{M}$	Total mass injection rate
$\dot{E}_{SN+SW}$	Total energy injection rate from SN and stellar winds
$\dot{M}_{SN+SW}$	Total mass injection rate from SN and stellar winds
ϵ	Termalization efficiency

β	Mass loading factor
Δ	Emission ratio
v_{ch}	Velocity channel
Δv_{ch}	Velocity channel resolution
$\tau(v_{ch})$	Optical depth along a velocity channel
$\kappa(v_{ch})$	Absorption coefficient
$N(v_{ch})$	Column density
$a(v_{ch})$	Absorption coefficient per atom
m_e	Mass of an electron
$\Delta\nu_{1/2}$	Gaussian HWHM
f	Oscillator strength
$H(v_{ch})$	Voigt profile
c	Speed of light
k_B	Boltzmann's constant
m	The atomic mass of an ion
ν_0	The frequency of the line center
$I(v_{ch})$	Intensity for a single velocity channel
$I_0(v_{ch})$	Initial intensity for a single velocity channel
$v_{\rm cen}$	Velocity at mid point of FWHM of absorption line
v_{90}	Velocity where absorption line return to 90% of continuum
δ	Scaling factor for velocity and SFR
$\Sigma_{\rm SFR}$	SFR density

CHAPTER 1: Background

A galactic wind is a key phase in the gas feedback cycle of galaxies (Heckman et al. 1990; Shapiro et al. 1994; Aguirre et al. 2001). Yet, uncertainties in the coupling between the galactic wind to the multi-phase interstellar medium (ISM) obscures how galaxy structure determines the evolution of the wind as its flow alters the ISM. Models cannot yet fully predict how often and under what circumstances galactic winds form, and their ultimate impact on galactic evolution.

Chevalier & Clegg (1985) made the first analytic model of how stellar winds from multiple stars can merge to alter the ISM completely. Over the first few Myr of a starburst, OB star winds inflate bubbles of hot, low density, metal enriched gas. Expanding bubbles shock and compress the ISM, then merge as a "superbubble" of radius > 0.1 kpc (Dawson 2013) that is powered first by OB and WR-star winds then SNe II. The superbubble can expand to exceed the scale height of the galaxy, potentially "blowing out" its metal-enriched gas into the low density halo (the "champagne effect", Tenorio-Tagle 1979) to form a galactic wind.

Observations beginning in the 1990s established galactic winds as ubiquitous phenomena associated with star-forming galaxies (Heckman et al. 1993; Bland-Hawthorn 1995; Dahlem 1997; Heckman et al. 2000). These observations focused on optical emission lines images and spectroscopy (Heckman et al. 1993). Optical imagery helped to establish the physical morphology of galactic winds and spectroscopy provided the kinematics and warm plasma diagnostics. While emission traced the interaction of the warm ISM with the hot wind, absorption lines probed the interaction between warm and cold gas and the hot wind (Heckman et al. 2000). X-ray emission, first observed in M82 (Watson et al. 1984), would also become important for identifying galactic outflows and measuring wind energetics (Fabbiano 1988; Fabbiano et al. 1990; Heckman et al. 1993, 1995). While some studies of galactic winds focused on X-ray emission (Strickland & Stevens 2000; Strickland & Heckman 2009), Bland-Hawthorn (1995) predicted that multi-band observations of galactic winds would become standard in characterizing galactic winds, and Veilleux et al. (2005) have shown that subsequent multi-band studies are important in characterizing the galactic wind.

More recent observations (Martin et al. 2012; Arribas et al. 2014; Rubin et al. 2014; Chisholm et al. 2015) continued to show that galactic winds are ubiquitous for star forming galaxies. Galactic winds are detected in 45% (Martin et al. 2012), 74% (Chisholm et al. 2015), and 66% (89% for face on, 45% for edge on galaxies) (Rubin et al. 2014) of star forming galaxies surveyed. Outflow kinematics are typically measured using UV

absorption lines such as: Mg II and Fe II (Rubin et al. 2014), Si II, Si III, Si IV and O I (Chisholm et al. 2015, 2016), and Na D (Heckman et al. 2000; Martin 2005).

Heckman et al. (2000) found that starburst galaxies whose Na D absorption line is dominated by the ISM typically exhibited outflow velocities of > 100 km s^{-1}, with maximum velocities ranging from $300 - 700$ km s^{-1} and were able to map outflow gas up to 10 kpc from the galactic center. They concluded that dense clouds in the ISM with a velocity at the galaxy systemic velocity is being disrupted by the galactic wind, and that the ablated gas is being accelerated up to the terminal wind velocity.

Martin (2005) investigated the relationship between outflow velocities, as measured by the Na D lines, and the SFR. She found that the maximum wind velocity correlates as SFR$^{1/3}$, and that stellar luminosity suffices to accelerate cool outflows to the terminal velocity. Martin noted that the covering fraction of the cold gas is not complete, which indicates that it is not a continuous fluid but is broken into clouds or shells.

Rubin et al. (2014) extended previous work using Mg II and Fe II absorption lines to find that outflows are detected for all ranges of $M_\star$, SFR and $\Sigma_{\rm SFR}$ studied. Interestingly they found no evidence of a minimum threshold for $\Sigma_{\rm SFR}$. This indicates that galactic winds can still form in galaxies with extremely low SFR densities. Although outflows are detected for all parameter ranges, a correlation is only found between outflow velocity and $M_\star$. These findings are both consistent with and conflict with previous work (Weiner et al. 2009; Chen et al. 2010; Heckman et al. 2011; Martin et al. 2012).

Conversely Chisholm et al. (2015) found correlations between $M_\star$ and SFR, but not with $\Sigma_{\rm SFR}$, using Si II absorption lines. They found a weak correlation between SFR and maximum velocity, but a slightly stronger correlation between SFR and the velocity as measured by the line center. In agreement with Rubin et al. (2014), Chisholm et al. (2015) found that there is no minimum $\Sigma_{\rm SFR}$ at which outflows are created.

Various models and simulations have been used to investigate the effect of different parameters on starburst driven galactic winds. Mac Low & McCray (1988) showed that the blowout likelihood is proportional to the mechanical luminosity of the starburst, and inversely proportional to the ISM pressure and disk scale height. Suchkov et al. (1994) concluded that galactic wind development depends on the nature of mass and energy injection in the starburst region. Silich et al. (1996) found that lower average densities in a non-uniform ISM increased bubble size, and also that an increase in mass loading decreases the interior temperature of the superbubble. Tenorio-Tagle et al. (1999) found that a superbubble blowout into the inter-galactic medium (IGM) depends heavily on the power of the nuclear starburst. Strickland & Stevens (2000) studied how ISM distribution, starburst characteristics and mass loading affect X-ray emission, and mass and energy transport into the IGM by the galactic wind. Fujita et al. (2009) and Strickland & Heckman (2009) simulated starbursts with different mass loadings and mechanical luminosities and determined the relationship to mass flow rates and galactic wind terminal velocities. Cooper et al. (2008) found that a

blowout is channeled by the scale height, density, and pressure of the ambient disk ISM. Melioli et al. (2013) investigated the dependence of galactic wind evolution on the environment at the base of the galactic wind and determined that optical filament formation depends on the clumpiness of the starburst region. Creasey et al. (2013) argued that higher gas surface density and lower gas fraction should make faster galactic winds.

Most simulations of starburst driven galactic winds have included radiative cooling, but have rarely examined the effects of cooling below 10^4 K. Early work by Mac Low & McCray (1988); Mac Low et al. (1989); Suchkov et al. (1994) and Silich et al. (1996) approximated cooling with a power-law relation down to 10^5 K. Subsequent studies have used the cooling tables of (Sutherland & Dopita 1993; Raymond et al. 1976; Sarazin 1986) down to 10^4 K. Strickland & Stevens (2000), and Sutherland & Bicknell (2007) addressed X-ray emission but not emission from cold gas and thus did not include cooling below 10^4 K. Strickland & Heckman (2009) used post processing to calculate emission but did not include cooling in their simulations. Cooper et al. (2008) considered Hα emission and X-rays, but were matching optical data. Creasey et al. (2013) argued that energy loss below 8,000 K is insignificant and does not affect galactic wind formation. Joung & Mac Low (2006) used a parameterized cooling curve (Dalgarno & McCray 1972) below 10^4 K to examine formation of cold dense clouds near supernovae. Fujita et al. (2009) found that cooling below 10^4 K does not affect gas outflow kinematics.

Evidently, the effect of low temperature cooling has not been thoroughly explored, therefore my dissertation considers the effects of cooling below 10^4 K on wind dynamics and content. My simulations tested these expectations over the first few Myr following a single instantaneous starburst. For consistency with previous studies of starbursts (Cooper et al. 2008; Strickland & Heckman 2009; Melioli et al. 2013), I fixed the galaxy size and shape at M82 values to focus on a set of parameters which include: the energy injection rate, the mass loading rate, radiative cooling, grid resolution, star formation rate (SFR), starburst radius, thermalization efficiency, and mass loading factor. In this dissertation I will show relationships between the outflow velocity, outflow emission, and these parameters.

Galactic winds are traced by filamentary optical (Bland & Tully 1988; Veilleux et al. 1994; Shopbell & Bland-Hawthorn 1998; Devine & Bally 1999) and X-ray emission (Strickland et al. 1997, 2002); and molecular (Walter et al. 2002) and atomic (Rupke et al. 2002, 2005) absorption. Structures in the emitting bands are tightly correlated, e.g. Cecil et al. (2002) combined *Chandra*, *HST*, and *VLA* datasets to characterize the environment and emitting filament towers of the galactic wind in NGC 3079. Those authors conclude that the towers form at the edge of the starburst and are remnants of the ISM propelled by the starburst, not from condensed wind. To determine how filaments can be used as tracers of wind dynamics I therefore consider filaments over temperatures that span X-ray to molecular emission.

CHAPTER 2: Code and Setup

2.1 Numerical Methods

I integrate numerically the inviscid hydrodynamical equations with the public Athena code (Stone et al. 2008). Section 2.4 describes my modifications to improve code stability as large pressure and density variations are encountered during cooling to low temperatures. The setup described here has been published in Tanner et al. (2016).

2.2 Gravitational Potential and Initial Velocity Field

Following Cooper et al. (2008) and Strickland & Stevens (2000) I model the stellar gravitational potential as a combined disk and bulge. The disk, with mass $M_{\rm disk}$, radial scale size a, and vertical scale size b is modeled as a Plummer-Kuzmin potential (Miyamoto & Nagai 1975)

$$\Phi_{\rm disk}(r,z) = -\frac{GM_{\rm disk}}{\sqrt{r^2 + (a + \sqrt{z^2+b^2})^2}} \tag{2.1}$$

The spheroidal bulge $\Phi_{\rm ss}(R)$ is modeled as a King model,

$$\Phi_{\rm ss}(R) = -\frac{GM_{\rm ss}}{r_0}\left[\frac{\ln\left[(R/r_0)+\sqrt{1+(R/r_0)^2}\right]}{(R/r_0)}\right], \tag{2.2}$$

with $R = \sqrt{r^2+z^2}$, radial scale size r_0, and mass $M_{\rm ss}$. The total potential is $\Phi_{\rm tot} = \Phi_{\rm disk} + \Phi_{\rm ss}$ using Equations 2.1 and 2.2. I neglect the contribution of the dark matter halo because my simulation only covers the central 1 kpc. In that region matter is baryon dominated (McMillan 2011). The disk gas is initially rotating at azimuthal velocity

$$v_\phi(r,z) = e_{\rm disk}\exp(-|z|/z_{\rm rot})\left(r\frac{\partial\Phi_{tot}(r,0)}{\partial r}\right)^{1/2} \tag{2.3}$$

Here $e_{\rm disk}$ is the ratio azimuthal to Keplerian velocity. Table 2.2 lists simulation parameter values. The parameters have been chosen to match the rotation curve of M82 (Strickland & Stevens 2000; Cooper et al. 2008). All boundaries in the simulation box are outflow boundaries. Any gas that reaches a boundary due

to the initial rotation is lost.

2.3 Gas Thermal Balance

The Athena code implements thermal physics as an external source term in the total energy equation. To range over the $10 < T < 10^8$ K anticipated in my simulations, I combined tabulated cooling curves for solar metallicity (Sutherland & Dopita 1993) with the low-temperature photoelectric heating (eq. 2.5) and cooling (eq. 2.6) of Koyama & Inutsuka (2002) based on Wolfire et al. (1995), with appropriate corrections by Inoue et al. (2006). Kim & Ostriker (2015) have used a similar implementation of heating and cooling in Athena. The rate of energy change (Field 1965) is

$$\mathcal{L} = n(\Gamma - n\Lambda(T)). \tag{2.4}$$

with heating

$$\Gamma = \begin{cases} 2 \times 10^{-26} \text{ erg cm}^{-3} \text{ s}^{-1} & : T < 10^4 \text{ K} \\ 0 & : T > 10^4 \text{ K} \end{cases} \tag{2.5}$$

and cooling where $T < 10^4$ K

$$\frac{\Lambda(T)}{\Gamma} = 10^7 \exp\left(\frac{-118400}{T + 1000}\right) + 0.014\sqrt{T}\exp\left(\frac{-92}{T}\right) \text{cm}^3. \tag{2.6}$$

For 10^4 < T < $10^{8.5}$ K, I use piecewise power-law fits to the tabulated cooling for collisional ionization equilibrium at solar metallicity from Sutherland & Dopita (1993). Although I do not anticipate temperatures above 10^8 K, for completeness I include emission through bremsstrahlung above $T > 10^{8.5}$ K using (Rybicki & Lightman 1986)

$$\Lambda = 2.1 \times 10^{-27} T^{1/2} n^2 Z^2. \tag{2.7}$$

Figure 2.1 shows the combined cooling curves. I use Eq. 2.4 to calculate cell emissivity and sum radiative losses along a chosen column to calculate gas emission. I separate emission into bands for cold gas, Hα, soft X-ray, mid X-ray and hard X-ray emission. Table 2.1 gives temperature ranges for the bands.

For series M (see Section 2.8 for a description of model series) I run all models twice with different cutoff temperatures where cooling is applied: first with cooling only applied when gas temperature > 10^4 K, then with cooling applied down to 10 K. In both cases I impose a temperature floor at 10 K. For models with cooling cut off at 10^4 K the gas can cool adiabatically below that but no radiative cooling is applied.

Table 2.1: Definition of gas temperature ranges

Band	Range
Cold Gas	$<$ 1e2 K
Warm Low	1e2-1e3 K
Warm High	1e3-5e3 K
Hα	5e3-4e4 K
Hot UV	4e4 K - 0.5 keV
Soft X-Ray	0.5-3.0 keV
Mid X-Ray	3.0-10.0 keV
Hard X-Ray	$>$ 10.0 keV

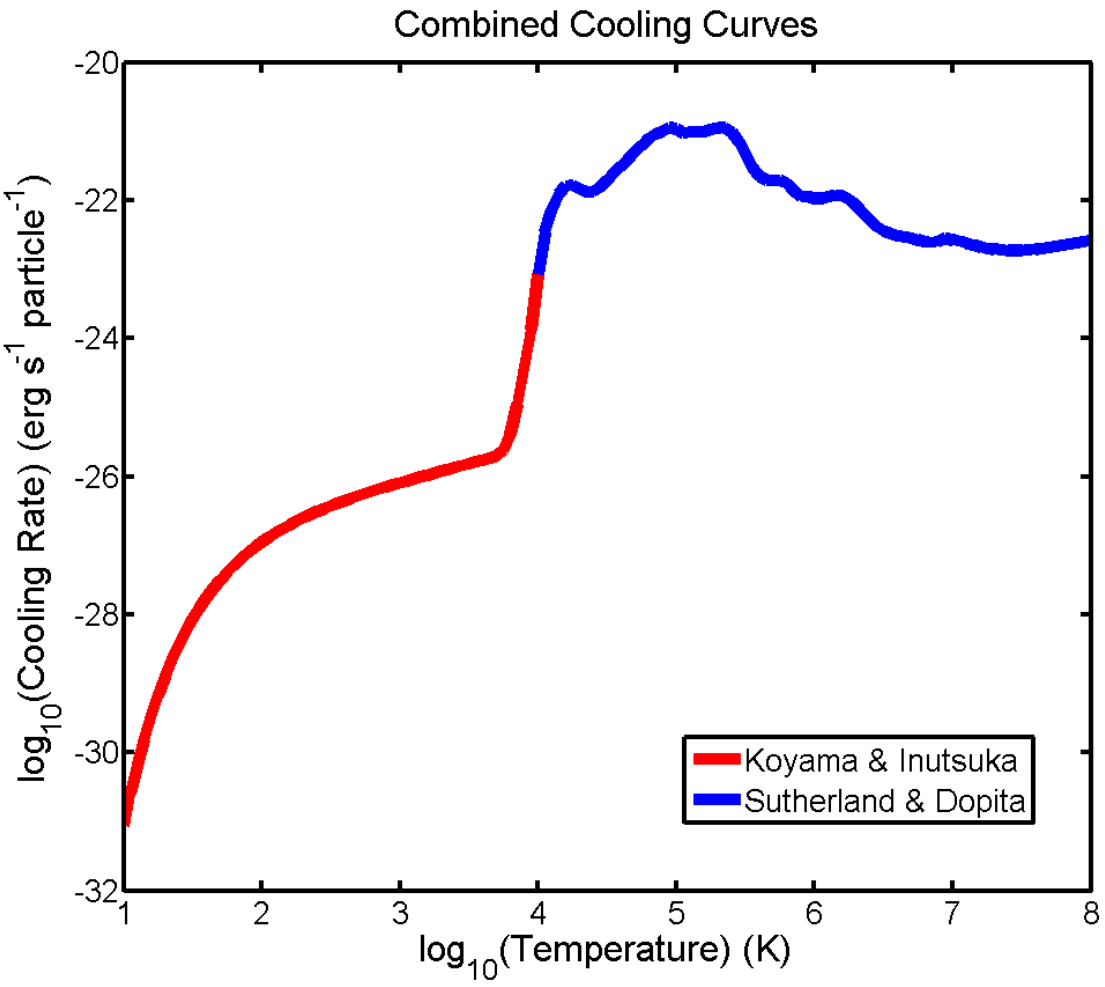

Figure 2.1: Combined cooling curves from Sutherland & Dopita (1993) and Koyama & Inutsuka (2002).

2.4 Base Code Modifications

In this section I detail the modifications I made to Athena. My code can be found on my website[1].

2.4.1 Cooling in Athena

Athena handles radiative cooling by adding an external source term given by Equation 2.4 to the energy equation within the CTU integrator. As noted in Section 2.3 I use tabulated data from Sutherland & Dopita (1993) and fit piecewise power-law functions, that I calculated using MATLAB's polyfit function, to the tabulated cooling (Figure 2.2). Between 10^4 and 10^5 K I use a 10th order polynomial. Between 10^5 and 10^6 K I use a 10th order polynomial. Between 10^6 and 10^7 K I use a 8th order polynomial. Between 10^7 and $10^{8.5}$ K I use a 5th order polynomial. Above $10^{8.5}$ K I use Equation 2.7 to calculate the emission.

Substantial T and pressure gradients in my simulations require modification to improve the accuracy of the cooling step by sub-cycling a 2/3rd order adaptive step-size integrator (Bogacki & Shampine 1989), as follows. For each cell at each time step, ΔT is calculated using a single pass through the Bogacki-Shampine method. If the difference between the 2nd and 3rd order results exceeds 10% or if the method returns a non-physical result (i.e. < 0 K or a NaN) then ΔT for the cell is recalculated using an adaptive step subroutine. Otherwise, I keep the result from the first pass.

As the cooling step ends I check if the calculated ΔT deviates the cell from its radiative equilibrium T at its current density. I calculate the equilibrium temperature at different densities using root finding methods in MATLAB, then I fit the equilibrium temperature using piecewise functions with a 5th order polynomial for densities below 1.0 particles cm^{-3}, and another 5th order polynomial for densities above 1.0 particles cm^{-3} (Figure 2.3). Both fits were found using the function polyval in MATLAB. I also impose a 10 K floor to ensure a physical result.

2.4.2 Kinetic Flux Vector Splitting

I add a backup way to calculate fluxes for the 1-5 cells (out of $6 \times N^3$ flux calculations) in a single time step where the normal calculation using the hllc solver returned a non-physical result (i.e. a NaN for the density or momentum). The fall-back algorithm, Kinetic Flux Vector Splitting (Mandal & Deshpande 1994), solves the collisionless Boltzmann equation. While more diffusive, it stabilizes at rarely encountered, extreme gradients. Because very few cells are affected, the overall diffusiveness of the code does not change.

[1] http://user.physics.unc.edu/∼rjtanner/data/code/

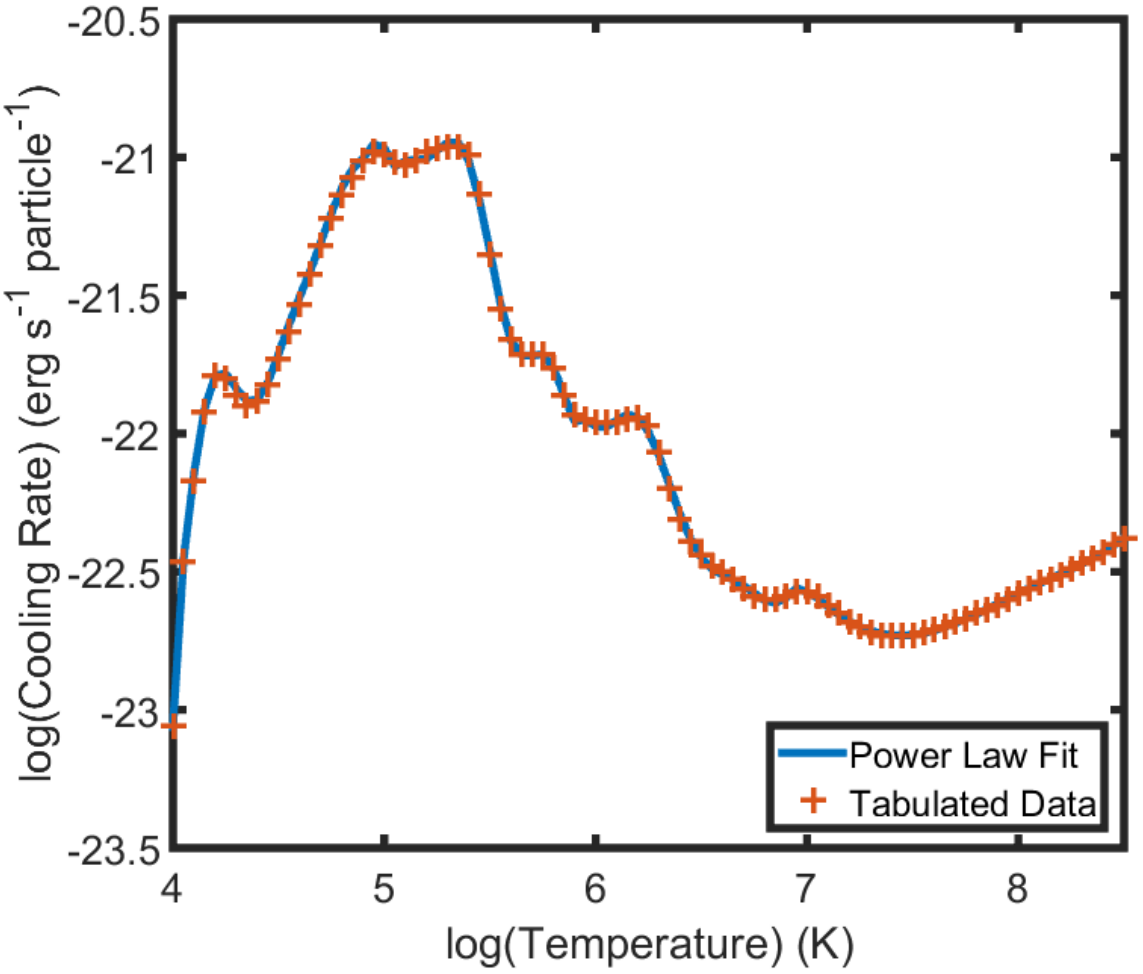

Figure 2.2: Comparison of Sutherland and Dopita tabulated cooling values and my piecewise power-law fit.

2.4.3 Integrator Modifications

My simulations encountered a few cases where the reconstructed density at the cell walls where negative. This typically happens when there are extreme differences density over a small number of cells (e.g. a low density, then high density, then low density). While Athena does check for negative densities after the reconstruction phase in the integrator, it applies a density floor in such a way that super-luminal speeds are calculated when the integrator calculates the fluxes at the cell boundaries. To avoid this problem, I use a first-order (piece-wise constant) interpolation over density when the higher order methods return negative density.

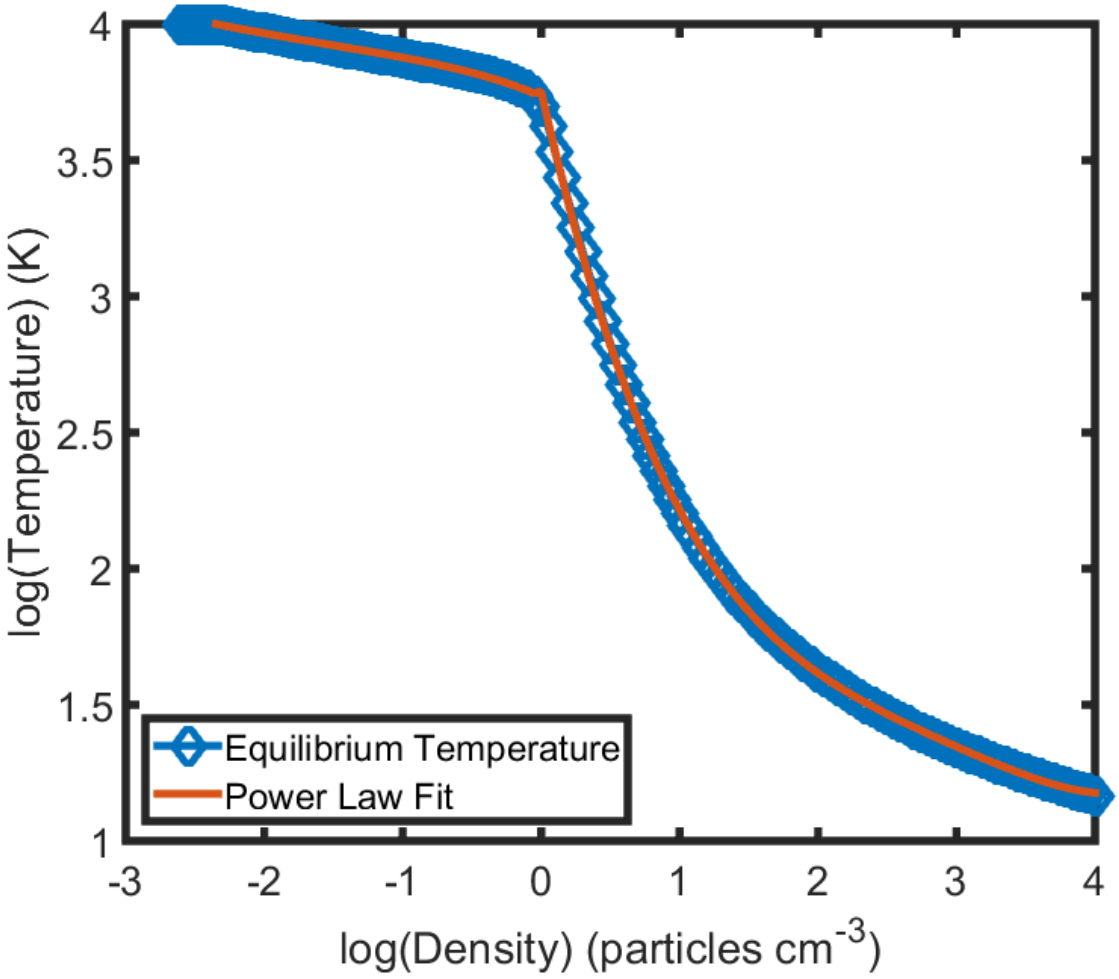

Figure 2.3: Comparison of calculated equilibrium temperatures and my piecewise power-law fit.

2.5 Initial Conditions of the ISM

To generate a realistic initial ISM, I multiply a smooth background against a fractal density distribution to mimic embedded clouds.

2.5.1 Smooth ISM

Densities in the computational domain are a combination of halo and disk distributions given by

$$n_{\rm halo}(r,z) = n_{\rm halo}(0,0) \times \exp\left[-\frac{\Phi_{\rm tot}(r,z) - e^2_{\rm halo}\Phi_{\rm tot}(r,0) - (1-e^2_{\rm halo})\Phi_{\rm tot}(0)}{c^2_{\rm s,halo}}\right], \tag{2.8}$$

$$n_{\rm disk}(r,z) = n_{\rm disk}(0,0) \times \exp\left[-\frac{\Phi_{\rm tot}(r,z) - e^2_{\rm disk}\Phi_{\rm tot}(r,0) - (1-e^2_{\rm disk})\Phi_{\rm tot}(0)}{\sigma^2_t + c^2_{\rm s,disk}}\right], \tag{2.9}$$

central density $n(0,0)$, sound speed $c_{s,disk} = \sqrt{k_B T_{disk}/m_H}$ that sets the scale height of each density profile, and $e_{\rm disk,halo}$ the ratio of azimuthal to Keplerian velocity. The turbulence parameter σ_t helps to form a thick disk without raising its temperatures artificially (see Cooper et al. 2008).

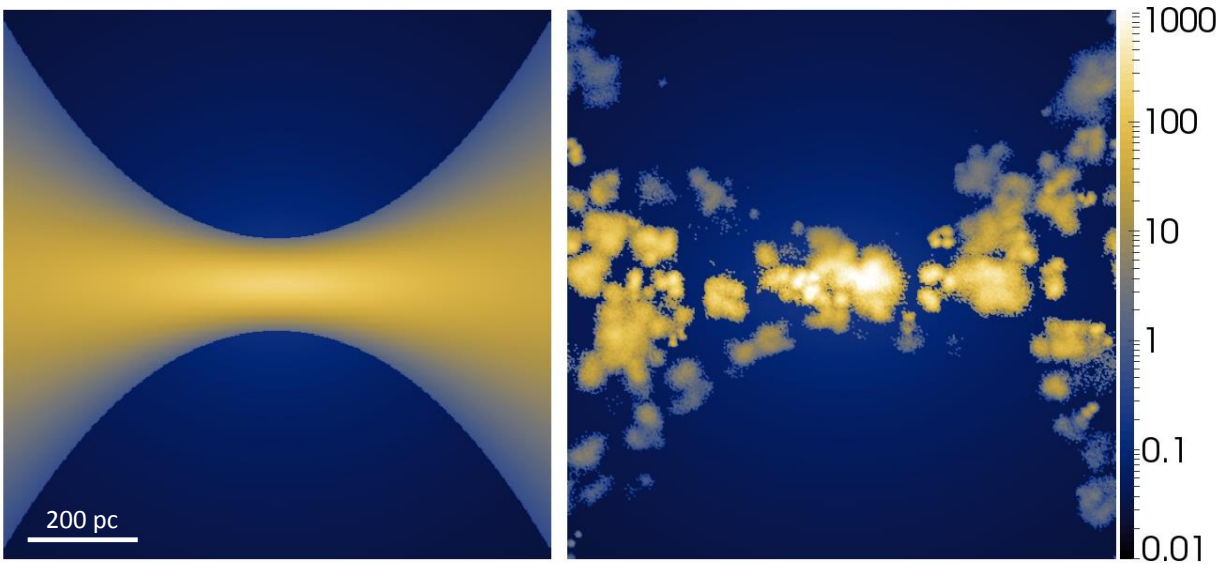

Figure 2.4: XZ plane slice of gas density ($n(r,z)$ in cm^{-3}) scaled logarithmically. *Left:* Smooth disk before adding fractal clouds. *Right:* The disk with fractal clouds.

2.5.2 Fractal Clouds

A "cloudy" ISM is mimicked by a fractal density distribution, multiplied against the smooth background disk density

$$n(r,z) = n_{\rm halo}(r,z) + n_{\rm disk}(r,z)N(r,z) \tag{2.10}$$

with $N(r,z)$ the fractal density fraction of each grid cell. To make a fractal density distribution I generate a set of individual fractal clouds following Mathis et al. (2002, §2) with modifications. I repeat the Mathis et al. approach for a single fractal cloud n_c times (see below), but with the constraint that first-level points must fall a distance of $\geqslant L/4$ from the edge of the box. I place each cloud within the computational domain and repeat for n_c fractal clouds with a scale length chosen at random between $50 < L < 150$ pc. Each cloud is placed semi-randomly on the computational grid to avoid excessive overlap. To set n_c, I repeat until the average fractal density of the grid equals the density of a single cloud.

For models with cooling applied only when $T > 10^4$ K, I set the disk pressure using $P_{\rm disk}(r,z) = n_{\rm disk}(r,z)c^2_{\rm s,disk}$. For models with cooling applied down to $T > 10$ K, the heating/cooling function sets the disk to thermal equilibrium (see §2.3). In this case the disk pressure is $P_{\rm disk}(r,z) = n_{\rm disk}(r,z)k_B T_{\rm TE}$. In

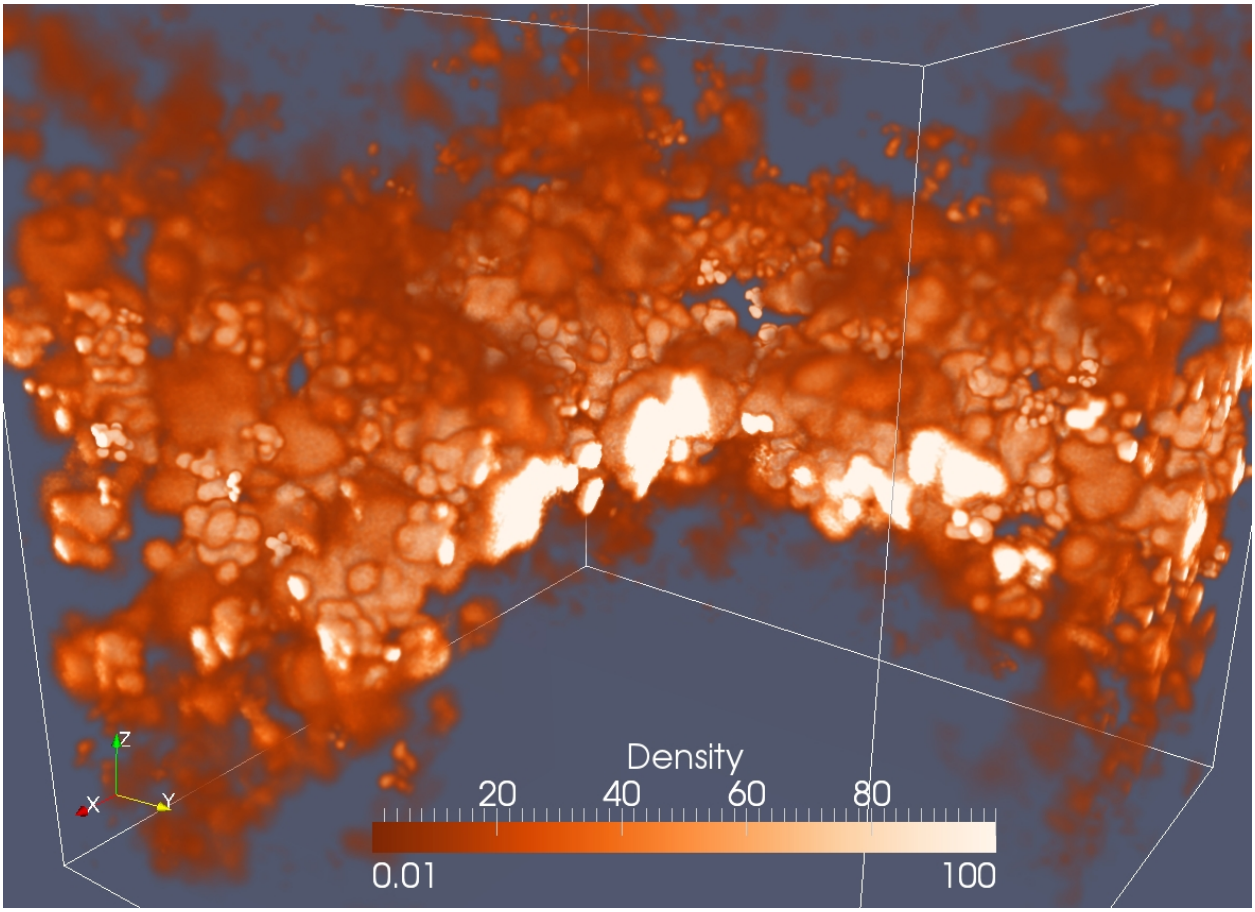

Figure 2.5: 3D cutaway of the density ($n(r,z)$ in cm^{-3}).

both cases when $T > 3 \times 10^4$ K, cells are set to halo densities and pressures only. This prescription is given as,

$$P(r,z) = \begin{cases} n_{\rm halo}(r,z)c^2_{\rm s,halo} + P_{\rm disk}(r,z) & : \ < 3 \times 10^4 \text{ K} \\ n_{\rm halo}(r,z)c^2_{\rm s,halo} & : \ > 3 \times 10^4 \text{ K} \end{cases} \tag{2.11}$$

I use the adiabatic exponent 5/3 and mean molecular weight 1.

I generated two files containing fractal points with 512^3 grid cells. The first file initialized all models that employed a single grid resolution across the domain. The fractal distribution was coarsened for lower resolution models so that the same initial density distribution was used for simulation with a single grid resolution. The second file was generated in the same way but with a higher average fractal density; it was used to initialize all simulations that employed static mesh refinement.

Table 2.2: Parameters used for simulation setup.

Symbol	Value	Property
Parameters used for initial gas distribution.		
$n_{\rm halo}(0,0)$	0.2 particles/cm^3	Central halo density
$n_{\rm disk}(0,0)$	100 particles/cm^3	Average density in starburst
$T_{\rm halo}$	5.0×10^6 K	Halo temperature
$T_{\rm disk}$	1.0×10^4 K	Average disk temperature
σ_t	60 km s^{-1}	Turbulence parameter for disk
$e_{\rm disk}$	0.95	Rotation ratio (disk)
$e_{\rm halo}$	0.00	Rotation ratio (halo)
Parameters used for the starburst.		
$R_{\rm sb}$	150 pc	Starburst radius
$H_{\rm sb}$	60 pc	Starburst height
Parameters used for the gravitational potential.		
$M_{\rm ss}$	$6 \times 10^8 M_\odot$	Stellar spheroid mass
$M_{\rm disk}$	$6 \times 10^9 M_\odot$	Stellar disk mass
r_0	350 pc	Stellar spheroid radial scale size
a	150 pc	Disk radial scale size
b	75 pc	Disk scale size
$z_{\rm rot}$	500 pc	Rotational scale height

Table 2.3: Grid set up for SMR models. Nx, Ny, and Nz are the number of cells in each direction. idisp, jdisp, and kdisp are the displacements measured in number of cells of that level from the base level. See the Athena documentation for more information.

Base Level		First Level		Second Level	
Nx	64	Nx	68	Nx	128
Ny	64	Ny	68	Ny	128
Nz	64	Ny	112	Ny	160
idisp	N/A	idisp	30	idisp	64
jdisp	N/A	jdisp	30	jdisp	64
idisp	N/A	kdisp	16	kdisp	96

2.6 Static Mesh Refinement

Athena can employ static mesh refinement (SMR) to increase grid resolution in predesignated regions in the domain. This allows for higher resolution where needed, while decreasing the total number of processors for a single simulation, thereby enabling more extensive parameter studies. Each level of refinement doubles the resolution.

When I employ SMR, I use two levels of refinement with both covering the center of the base grid in the x and y directions, and extending to the +z boundary, as shown in Figure 2.6. This allows for high resolution in the starburst and wind region directly above the starburst. In Section 2.8 I indicate models with SMR. Table 2.3 gives the grid set up for my SMR models.

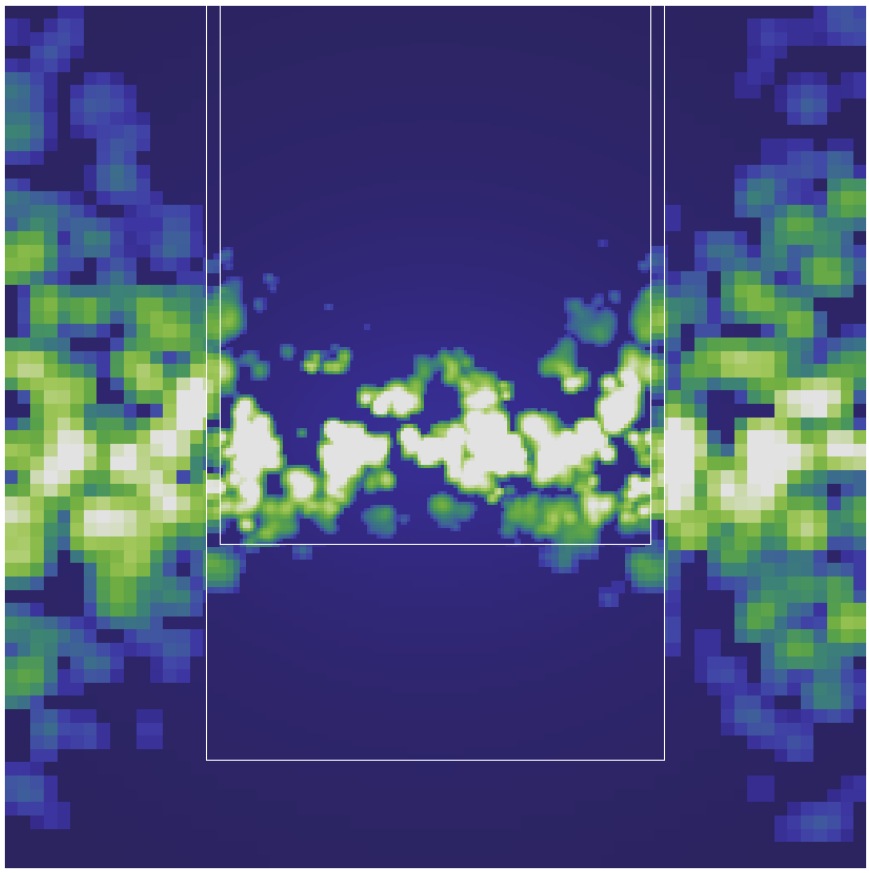

Figure 2.6: XZ plane slice of gas density ($n(r, z)$ in cm^{-3}) scaled logarithmically. White lines indicate SMR levels of refinement.

2.7 Starburst

I model a spheroidal central starburst using

$$1 > \frac{(x^2 + y^2)}{(R_{\rm sb}^2)} + \frac{(z^2)}{(H_{\rm sb}^2)}, \tag{2.12}$$

of radius $R_{\rm sb}$ and height $H_{\rm sb}$. At each time step I inject mass and energy into the starburst volume at rates $\dot{M}$ and $\dot{E}$. Each cell in the starburst region is injected with mass and energy proportional to that cell's fraction of the total initial ISM mass within the starburst volume. At each timestep I calculate the change in the mass (dM) and energy (dE) of each cell inside the starburst using

$$\frac{dE}{dtdV_{cell}} = \frac{\dot{E} n_{ini}}{\int n_{ini} dV_{SB}} \tag{2.13}$$

$$\frac{dM}{dtdV_{cell}} = \frac{\dot{M} n_{ini}}{\int n_{ini} dV_{SB}}. \tag{2.14}$$

Here dV_{cell} is the cell volume, n_{ini} is the initial density of the cell. To avoid a sharp boundary between the starburst and the ISM I apply a *tanh* profile to n_{ini} in the following way.

$$n_{ini} = n(r,z)\left(0.5\frac{1.0-\tanh\left(r-R_{\rm sb}\right)}{R_{\rm sb}/4}\right)\times\left(0.5\frac{1.0-\tanh\left(|z|-H_{\rm sb}\right)}{H_{\rm sb}/4}\right) \tag{2.15}$$

Here $n(r,z)$ is the total density as defined by Equation 2.10.

The energy injection rate ($\dot{E}$) is directly related to the mechanical luminosity of the starburst by

$$\dot{E} = \epsilon\dot{E}_{SN+SW}, \tag{2.16}$$

with ϵ the thermalization efficiency and $L_\star$ the mechanical luminosity (Veilleux et al. 2005). The exact value of ϵ depends on the local environment of the stars in the starburst and is time dependent (Freyer et al. 2003; Veilleux et al. 2005; Strickland & Heckman 2009; Kim & Ostriker 2015). Freyer et al. (2003) show that the thermalization efficiency varies over time, ranging from 0.1 immediately after star formation to ~ 0.01. Strickland & Heckman (2009) mention that 0.1 is the practical lower limit for the thermalization efficiency and conclude that a proper value for M82 ranges from 0.3 to just shy of 1.0. However, Kim & Ostriker (2015) find efficiency ranging from 0.1 to 1.0, but highly time dependent with rapid shifts between 1.0 and 0.1-0.3. Unless explicitly stated, for simplicity I set $\epsilon = 1$. For my models, energy is injected only as internal energy, not kinetic energy.

Like most high-resolution simulations (Suchkov et al. 1996; Cooper et al. 2008; Strickland & Heckman 2009), I combine contributions of stellar mass loss with that ablated from cold molecular clouds that are unresolved in my simulations as given in Equation 2.17.

$$\dot{M} = \dot{M}_{SN+SW} + \dot{M}_{cold} = \beta\dot{M}_{SN+SW}, \tag{2.17}$$

with β the mass loading factor. $\dot{M}_{SN+SW}$ is the total mass returned to the ISM from supernovae and stellar winds. It is called the central mass loading by Suchkov et al. (1996), or the mass injection rate by Cooper et al. (2008) and Strickland & Heckman (2009). I call it the mass loading rate.

Starburst99 population synthesis models (Leitherer et al. 1999) can model a starburst as either a single instantaneous starburst (SIB) or assuming continuous star formation (CSF). The energy and mass output of a SIB is dominated by stellar winds for the first 3 Myr until the first supernovae detonate. Because $\dot{E}_{SN+SW}$ and $\dot{M}_{SN+SW}$ calculated by Starburst99 are roughly constant for the first 3 Myr of a burst (Figs. 2.7, 2.8), for models that employ a SIB I inject mass and energy into the ISM at constant rates. The initial energy

and mass input from a SIB scales with starburst stellar mass as,

$$\dot{E}_{SN+SW} = 7.261e40(\text{erg s}^{-1})(M_{tot}/10^7\text{M}_\odot) \tag{2.18}$$

$$\dot{M}_{SN+SW} = 0.01866(\text{M}_\odot\text{yr}^{-1})(M_{tot}/10^7\text{M}_\odot) \tag{2.19}$$

with $\dot{E}_{SN+SW}$ the energy input in units of erg s^{-1}, $\dot{M}_{SN+SW}$ the mass input in units of M$_\odot$ yr^{-1}, and M_{tot} the total mass of the SIB in units of M$_\odot$.

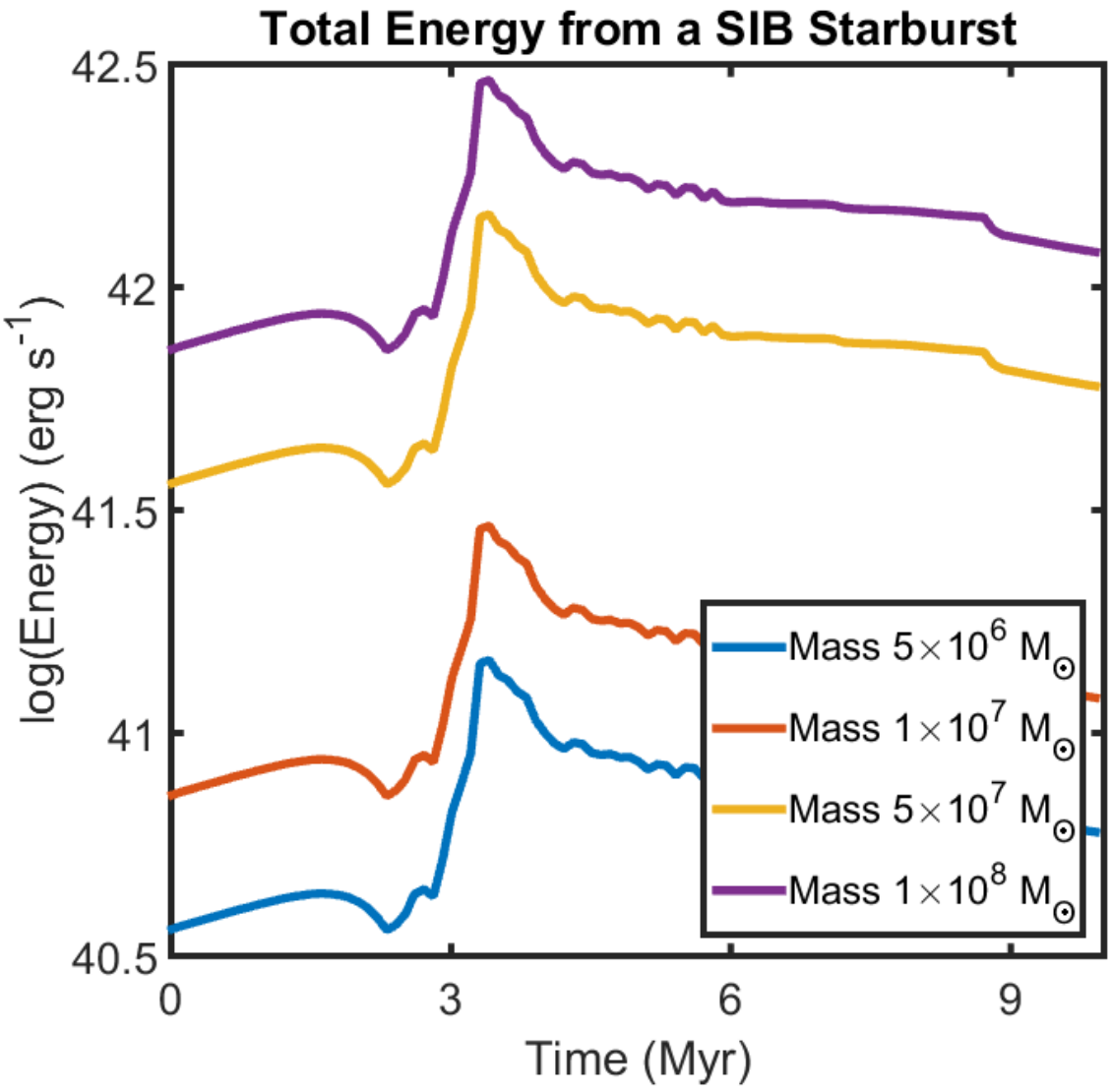

Figure 2.7: $\dot{E}_{SN+SW}$ (erg s^{-1}) for SIB starbursts with initial mass ranging from 5×10^6M$_\odot$ to 1×10^8M$_\odot$. From Starburst99 population synthesis models (Leitherer et al. 1999). All my analysis is done at 1.5 Myr when all models have achieved a steady-state solution, but before supernovas explode. Therefore I only consider a constant energy input.

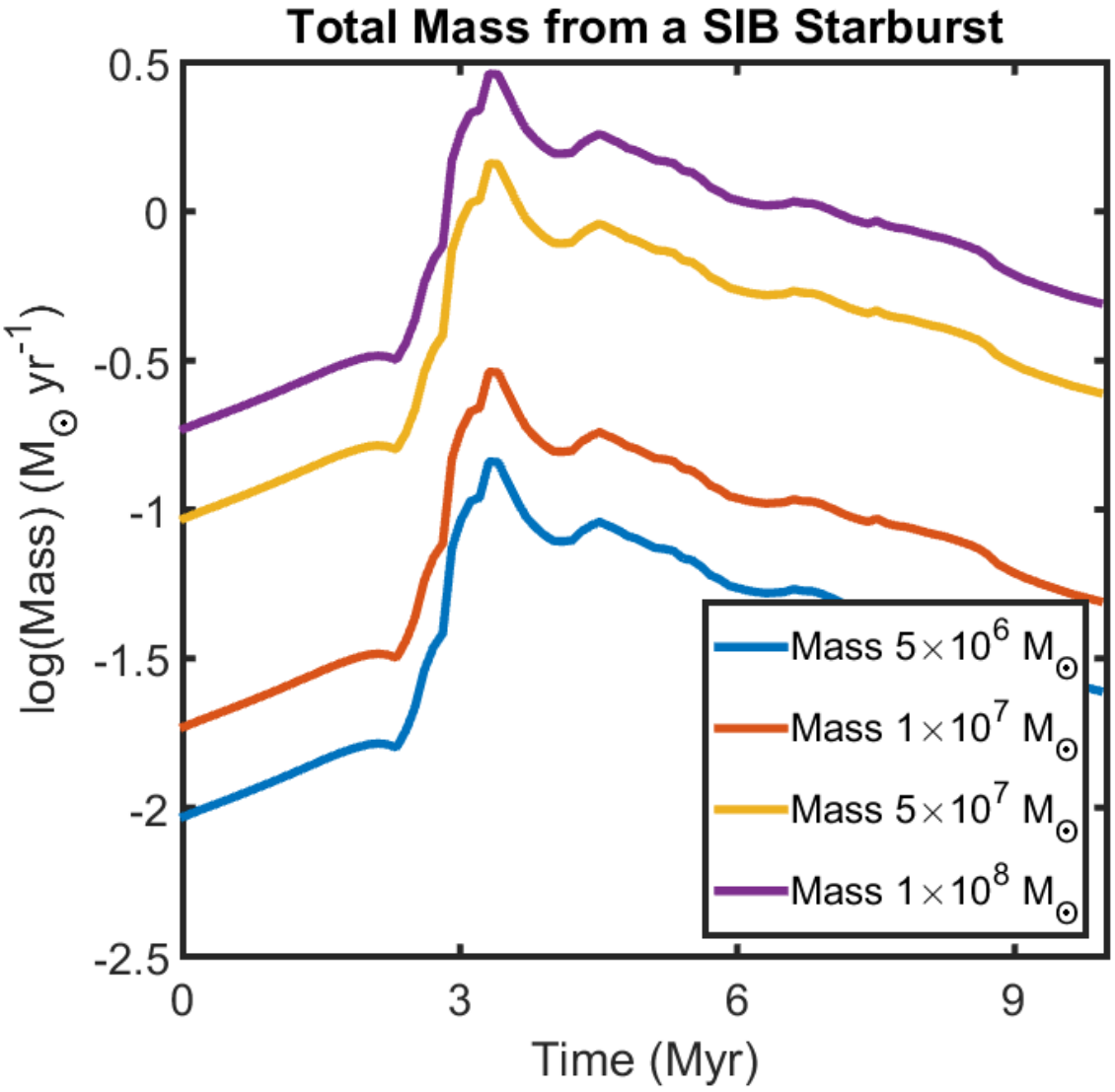

Figure 2.8: $\dot{M}_{SN+SW}$ ($M_\odot$ yr^{-1}) for SIB starbursts with initial mass ranging from $5 \times 10^6 M_\odot$ to $1 \times 10^8 M_\odot$. From Starburst99 population synthesis models (Leitherer et al. 1999).

For CSF, energy increases for the first 5 Myr, then remains constant thereafter due to a constant supernovae rate. Thus for my models that assume CSF, I simulate starting 5 Myr after the onset of star formation. While this is after the onset of SNs, I do not have sufficient resolution to accurately model individual SNs. Kim & Ostriker (2015) modeled individual SN inside a three phase ISM and determined that estimates of the thermalization efficiency and energy losses due to radiative cooling associated with a single SN are not accurate for grid resolutions $\gtrsim 0.1$ pc. Because my finest spacial resolution is 2.0 pc, I do not attempt to simulate individual SN. Future work with a more accurate sub-grid model, or greater resolution would alleviate this issue.

After a starburst with CSF has achieved a steady state, the energy and mass input rates are related to

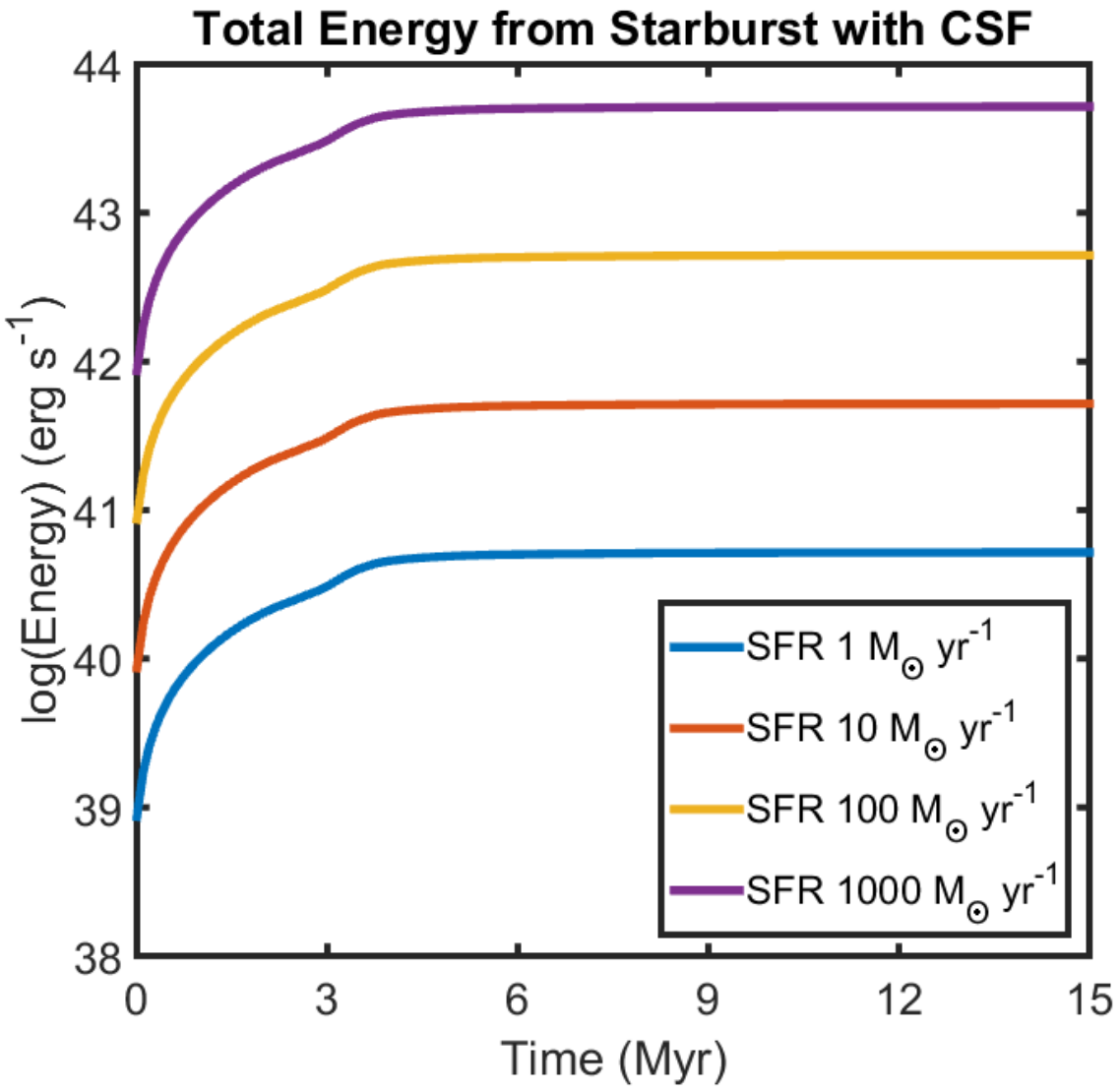

Figure 2.9: $\dot{E}_{SN+SW}$ (erg s^{-1}) for starbursts with CSF with SFR ranging from 1 M$_\odot$ yr^{-1} to 1000 M$_\odot$ yr^{-1}. From Starburst99 population synthesis models (Leitherer et al. 1999).

the SFR (in units of M$_\odot$ yr^{-1}) by

$$\dot{E}_{SN+SW} = 4.324e41 \text{ (erg s}^{-1}\text{) (SFR/M}_\odot \text{ yr}^{-1}\text{)} \tag{2.20}$$

$$\dot{M}_{SN+SW} = 0.1902 \text{ (M}_\odot \text{ yr}^{-1}\text{) (SFR/M}_\odot \text{ yr}^{-1}\text{)} \tag{2.21}$$

2.8 Model Parameters

All my models span a cube 1 kpc on a side. My models are divided into six series labeled M, K, S, R and F.

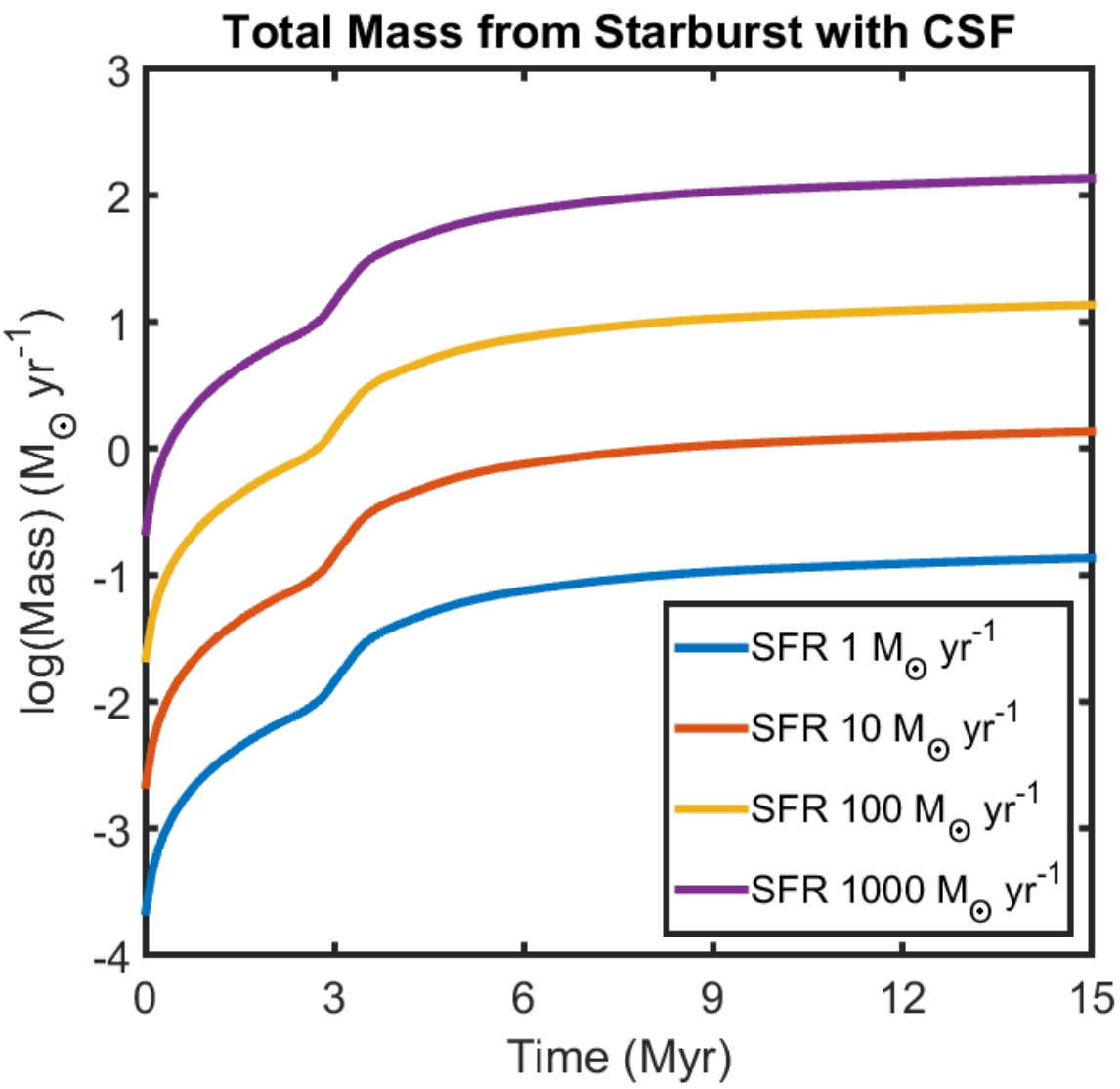

Figure 2.10: $\dot{M}_{SN+SW}$ ($M_\odot$ yr^{-1}) for starbursts with CSF with SFR ranging from 1 $M_\odot$ yr^{-1} to 1000 $M_\odot$ yr^{-1}. From Starburst99 population synthesis models (Leitherer et al. 1999).

Models for series M assume a SIB and are divided into 128^3, 256^3, or 512^3 fixed cells with spatial resolution 7.8, 3.9, or 2.0 pc respectively. My low resolution models vary $0.5 \leqslant \dot{M} \leqslant 3.5$ $M_\odot$ yr^{-1} in steps of 0.5 $M_\odot$ yr^{-1}, and $5 \times 10^{40} \leqslant \dot{E} \leqslant 1 \times 10^{42}$ erg s^{-1} in steps of 0.25 dex. Nine medium resolution models range from $1.0 \leqslant \dot{M} \leqslant 2.0$ $M_\odot$ yr^{-1} and $1 \times 10^{41} \leqslant \dot{E} \leqslant 5 \times 10^{41}$ erg s^{-1} with another medium resolution model at $\dot{M} = 1.0$ $M_\odot$ yr^{-1}, $\dot{E} = 1 \times 10^{42}$ erg s^{-1}. These ranges straddle the transition from blowout to no blowout. Two high resolution models use $\dot{M} = 1.5$ $M_\odot$ yr^{-1}, $\dot{E} = 2.5 \times 10^{41}$ erg s^{-1} and $\dot{M} = 1.0$ $M_\odot$ yr^{-1}, $\dot{E} = 1 \times 10^{42}$ erg s^{-1}. The former was chosen to study a low energy GW, while the latter was chosen to study a high energy GW and for comparison to Cooper et al. (2008) who use the same mass and energy injection rates.

Table 2.4: $\dot{M}$ and $\dot{E}$ used for Fig. 3. Index refers to model number. First index in model number corresponds to $\dot{M}$, second to $\dot{E}$.

Index	$\dot{M}(M_{\odot}yr^{-1})$	$\dot{E}(erg\ s^{-1})$
1	0.5	5.0e40
2	1.0	7.5e40
3	1.5	1.0e41
4	2.0	2.5e41
5	2.5	5.0e41
6	3.0	7.5e41
7	3.5	1.0e42

Using equation 2.18, the energy injection rates in my M series models yield a mass scale of $5 \times 10^6 < M < 1 \times 10^8 M_{\odot}$. Barker et al. (2008) give a total mass for the starburst in M82 of $\sim 4 \times 10^7 M_{\odot}$. Thus my simulations exceed the range of SIBs comparable in mass to the starburst in M82 to adequately investigate the limit of a superbubble blowout.

Fujita et al. (2009) explored mass loading rates ranging from 1.7 $M_{\odot}$ yr^{-1} to 120 $M_{\odot}$ yr^{-1}. Strickland & Heckman (2009) explored a much smaller range and determined a mass flow rate corresponding to M82 to be $1.4 \lesssim \dot{M} \lesssim 3.6$ $M_{\odot}$ yr^{-1}. I choose mass loading values that are similar to Strickland & Heckman (2009). This corresponds to values $2 \lesssim \beta \lesssim 15$ for the most energetic starbursts and $35 \lesssim \beta \lesssim 242$ for the smallest.

The simulations for series M, with associated energy and mass inputs, are given in Table 2.11. Model numbers denote grid resolution, $\dot{M}$, $\dot{E}$ and cooling used. Models starting with "M1", "M2" or "M5" correspond to 128^3, 256^3, and 512^3 cells respectively. Postfix indicies designate $\dot{M}$ and $\dot{E}$ respectively, see Table 2.4 column 1. T4 models cool to 10^4 K, T1 models to 10 K. To summarize my nomenclature, model "M1_34T4" has 128^3 cells with $\dot{M} = 1.5$ $M_{\odot}$ yr^{-1}, $\dot{E} = 2.5 \times 10^{41}$ erg s^{-1}, and cooling limited to $T > 10^4$ K.

7	3.5	128	128	128	128	128	128	128
6	3.0	128	128	128	128	128	128	128
5	2.5	128	128	128	128	128	128	128
4	2.0	128	128	128, 256	128, 256	128, 256	128	128
3	1.5	128	128	128, 256	128, 256, 512	128, 256	128	128
2	1.0	128	128	128, 256	128, 256	128, 256	128	128, 256, 512
1	0.5	128	128	128	128	128	128	128
		5.0e40	7.5e40	1.0e41	2.5e41	5.0e41	7.5e41	1.0e42
		1	2	3	4	5	6	7

Figure 2.11: The models are arranged with increasing mass loading (in $M_{\odot}$ yr^{-1}) on the vertical and increasing mechanical luminosity (in erg/s) on the horizontal. The indices on the horizontal and vertical axes correspond to the indices listed in Table 2.4 and identify the models. This arrangement is also used for Figure 4.1.

I ran the 49 combinations of $\dot{M}$ and $\dot{E}$ in Table 2.4 with 128^3 cells, ten combinations with 256^3, and two

with 512^3. Each model was run twice, once with cooling to 10^4 K then to 10 K, for a total of 122 models for series M.

Series K, S, R, and F use SMR (see §2.6) with the same configuration for all models. I use two two levels of refinement with the base grid divided into 64^3 cells, the first level divided into $64 \times 64 \times 112$ cells, and the second level divided into $128 \times 128 \times 160$ cells. This gives spatial resolution of 15.6 pc on the base and 7.8 and 3.9 pc on each level of refinement. Thus the highest level of refinement has the same resolution as the medium resolution M series models.

The K series assumes an SIB and fixed mass loading rate either 1.5 or 3.5 $M_\odot$ yr^{-1} and sets the energy input to achieve a set analytic wind velocity (see §3.2, eq. 3.1). The velocity ranges from 200 to 500 km s^{-1} in steps of 25 km s^{-1}, and then from 600 to 2200 km s^{-1} in steps of 100 km s^{-1} for a total of 60 models. Model numbers denote first the mass loading rate, then the velocity. Thus model number K_15_1800 corresponds to mass loading rate 1.5 $M_\odot$ yr^{-1} and analytic velocity 1800 km s^{-1}.

The S series assumes CSF and varies the SFR from 1 to 100 $M_\odot$ yr^{-1} in steps of 0.1 dex. Each model in the S series has a fixed analytic wind velocity of 1000, 1500 or 2000 km s^{-1} for a total of 63 models. Model numbers denote first the analytic wind velocity then the SFR. Thus model number S_15_79 has analytic wind velocity 1500 km s^{-1} and SFR 7.9 $M_\odot$ yr^{-1}.

The R series assumes CSF and varies the radius of the starburst (R_{SB}) from 50 to 500 pc in steps of 0.1 dex. Each model in the R series has a fixed SFR of 10, 50 or 100 $M_\odot$ yr^{-1} for a total of 33 models. Model numbers denote first the SFR then the starburst radius. Thus model number R_50_79 has SFR 50 $M_\odot$ yr^{-1} and starburst radius 79 pc.

The F series assumes CSF and varies the thermalization efficiency (eq. 2.16) between 0.2 and 1.0 in steps of 0.2, and varies the mass loading factor (eq. 2.17) from 1.0 to 10.0 in steps of 0.1 dex. Each model in the F series has a fixed SFR of 10 or 50 $M_\odot$ yr^{-1} for a total of 110 models. Series F is similar to series M in that I vary the mass and energy injection rates, but I set ranges of the thermalization efficiency and the mass loading factor to match the parameter space explored by Strickland & Heckman (2009) with their 2D and 1D models. Model numbers denote first the SFR, then the thermalization efficiency, then the mass loading factor. Thus model number F50_2_79 has SFR 50 $M_\odot$ yr^{-1}, thermalization efficiency 0.2, and mass loading factor 7.9.

The different series are summarized in Table 2.5. All series are run for 1.5 Myr, unless otherwise noted. All analysis is performed at 1.5 Myr after the start of the simulation. Basic data cubes of all series at 1.5

Table 2.5: Series of simulations run with basic information on each series.

Series	Starburst Type	Grid Type	Variable(s) Tested
M	SIB	Single Grid	Mass loading rate, Energy injection rate, Cooling, Resolution
K	SIB	SMR	Analytic wind velocity
S	CSF	SMR	SFR
R	CSF	SMR	Starburst radius
F	CSF	SMR	Thermalization efficiency, Mass loading factor

Myr after the start of the simulation will be available on my website[2].

[2]http://user.physics.unc.edu/∼rjtanner/data/simulationdata/

CHAPTER 3: Blowout Conditions and Structure

3.1 Wind Structure

Figures 3.1 and 3.2 show a "typical" GW in my highest resolution models (M5_34T1 and M5_27T1). They plot at 1.5 Myr a yz-slice of temperature and density together with column integrated Hα and soft X-ray emission. The mass and energy injection rates of model M5_27T1 powers a GW of terminal velocity ~ 1420 km s^{-1}. My M5_34T1 model with a quarter the energy injection but 50% higher mass injection rate still forms a GW but with terminal velocity ~ 540 km s^{-1}. After 1.5 Myr, model M5_34T1 has accumulated enough energy to blow out (Fig. 3.1) but insufficient to clear the entire volume as model M5_27T1 does.

Models that blow out have a hot ($\gtrsim 10^6$ K) free-wind region where the velocity is set by $\dot{E}$ and $\dot{M}$. Embedded in the free wind are dense (> 10 particle cm^{-3}) filaments of warm and cold gas (< 5000 K) surrounding dense cores (> 100 particle cm^{-3}) that have been swept up by the wind. These filaments are discussed in Chapter 5. The swept-up gas substrate is shock heated to $\gtrsim 10^7$ K and surrounds the free wind as a shell.

3.2 Outflow Wind Speed

The analytic terminal wind speed of a blowout is related to $\dot{E}$ and $\dot{M}$ (see Fujita et al. 2009, based on Weaver et al. (1977) and McCray & Kafatos (1987)) as

$$v_A \equiv \left(2 \frac{\int \dot{E} dt}{\int \dot{M} dt} \right)^{1/2} . \tag{3.1}$$

It is related to the simulated wind speed (v_w) by

$$v_w = \xi^{1/2} v_A \tag{3.2}$$

Fujita et al. (2009) give $\xi = 5/11 \approx 0.45$ which is the fraction of $\dot{E}$ that drives the kinetic energy within a bubble that is embedded in a uniform ISM (Weaver et al. 1977). For comparison to analytical results, I determine ξ from my model set (Fig. 3.3). Eq. 3.2 is generally reproduced by my models: T4 models when $\xi = 0.650 \pm 0.007$; T1 models when $\xi = 0.68 \pm 0.03$ for $v_A > 600$ km s^{-1}.

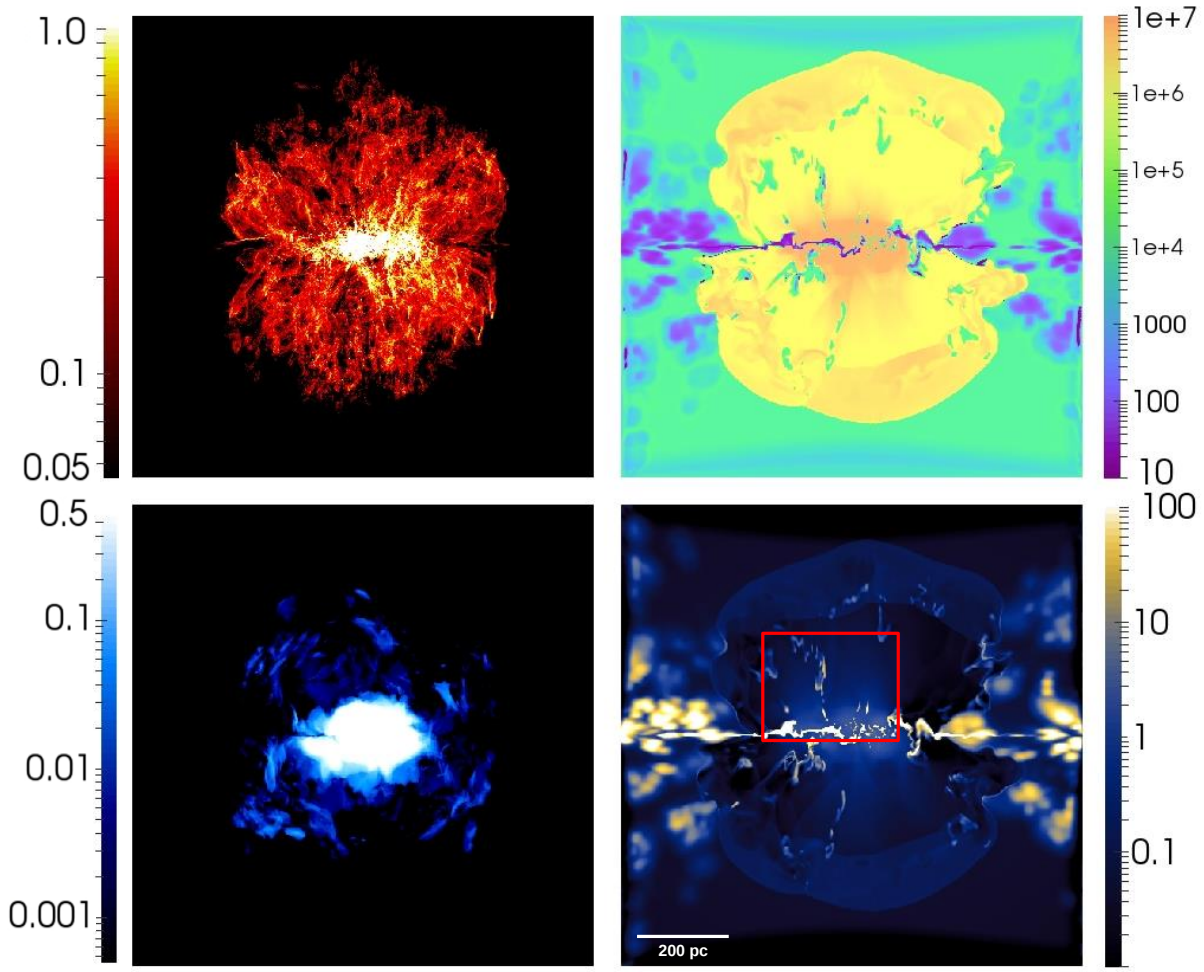

Figure 3.1: A slice in the yz plane through the center of the galaxy for model M5_34T1 at 1.5 Myr. Clockwise from top left: Hα emission (log erg s^{-1} cm^{-2}) and temperature (log K), density (log cm^{-3}), and soft X-ray emission scaled as log(erg s^{-1} cm^{-2}). Red box in bottom right image indicates the zoomed-in region of Figure 5.2.

The escape velocity from the model galaxy is $v_e \approx 490$ km s^{-1}. For $v_A < v_e$, my simulations do not blow out. For $v_A > 1.5v_e$, my T4 and T1 series are identical, and increased resolution does not alter the wind speed. In the transition $v_e < v_A < 1.5v_e$, my T4 models have higher simulated wind speeds than T1 models (Fig. 3.3 inset); both deviate from the relation in Eq. 3.2.

Using Equations 2.16 and 2.17 I can relate the analytic wind speed to the energy and mass injection rates from Starburst99 population synthesis models (Leitherer et al. 1999).

$$v_w = \left(2\xi \frac{\int \epsilon \dot{E}_{SN+SW} dt}{\int \beta \dot{M}_{SN+SW} dt} \right)^{1/2}. \tag{3.3}$$

I can further simplify this using Equations 2.18 and 2.19 to get a relationship for the analytic wind speed for

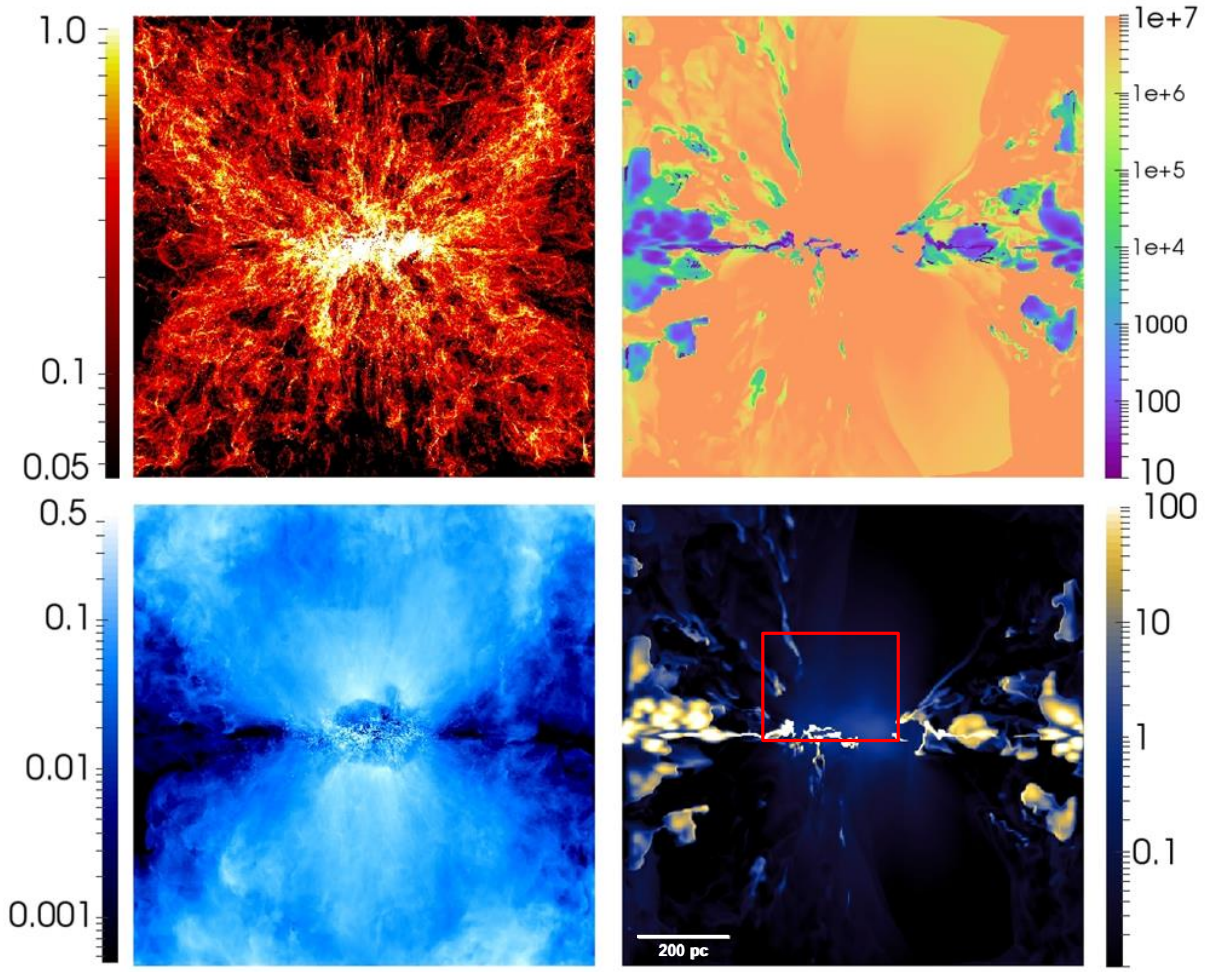

Figure 3.2: Same as Figure 4, but now for model M5_27T1 at 1.5 Myr. Red box in bottom right image indicates the zoomed-in region of Figure 5.3.

the first $\sim$ 3 Myr of a SIB. Because both Equations 2.18 and 2.19 depend on the total mass of the starburst, the mass cancels out and we see that the terminal wind speed depends only on the thermalization efficiency and the mass loading factor.

$$v_w = (2,478 \text{ km s}^{-1})\sqrt{2\xi\frac{\epsilon}{\beta}} \tag{3.4}$$

Doing the same for CSF using Equations 2.20 and 2.21 gives,

$$v_w = (1,894 \text{ km s}^{-1})\sqrt{2\xi\frac{\epsilon}{\beta}}. \tag{3.5}$$

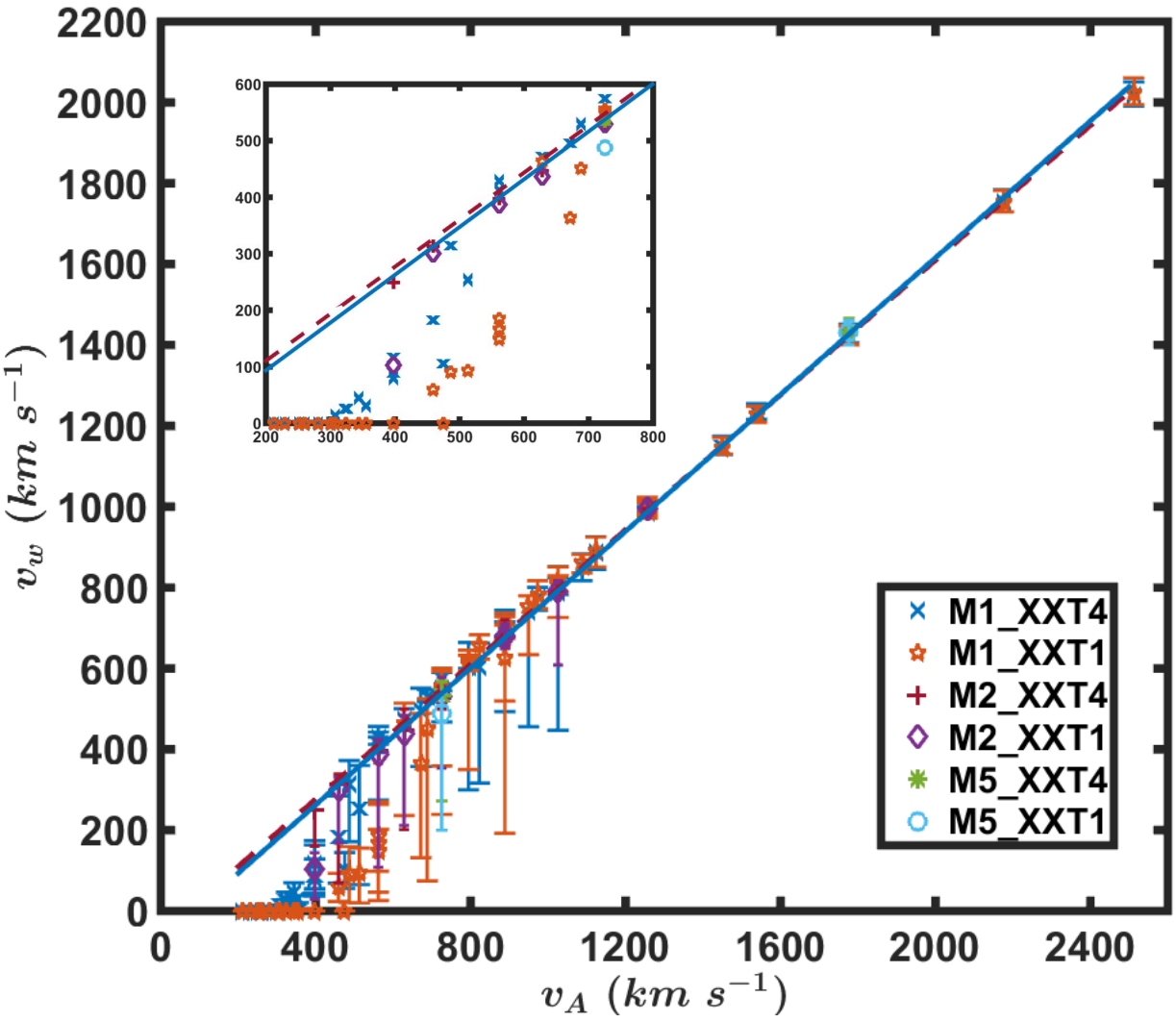

Figure 3.3: Analytical wind speed (from Eq. 3.1) vs. simulated vertical wind velocity (v_w) 100 pc above the disk plane at 1.5 Myr. Linear fits are shown for all simulations having $v_A > 500$ km s^{-1}. Inset: Close up of the break where analytical wind speed deviates from the simulated value.

CHAPTER 4: Emission as Blowout Tracer

When viewing starburst galaxies edge on we use emission from the superbubble to determine if a blowout has occurred. In this chapter I investigate how to use the emission from the starburst and associated superbubble to infer starburst properties. Figure 4.1 maps emission of Hα and soft X-rays for the M1_XXT1 models, viewed edge-on. Note:

1. Emission morphology reveals the threshold $\dot{M}$ and $\dot{E}$ for a blowout. As expected from Eq. 3.1, larger $\dot{M}$ inhibits blow out but larger $\dot{E}$ promotes it.

2. Soft X-rays delineate the starburst and shell of the superbubble, and fill the free wind region (Fig. 3.1). X-rays brighten with increasing $\dot{M}$. For low $\dot{M}$ but high $\dot{E}$ the starburst emits few X-rays. With higher $\dot{M}$ the hot free wind has higher mass, boosting the X-ray emissivity.

To determine which emission bands can trace a blowout I define Δ as the ratio of total emission in the lower halo ($z > 85$ pc) to the disk ($z < 85$ pc). Figure 4.2 compares Δ for different emission bands to the terminal wind speed v_w. Simulations with $v_w > 300$ km s^{-1} have clearly experienced a blowout. Results in the blowout regime suggest the relation

$$\Delta = \alpha v_{wind}^{\kappa}. \tag{4.1}$$

Here α and κ are constants. All bands follow this relation except for the cold gas (top right panel of Figure 4.2). Wind speed does not significantly affect cold gas emission, though there may be increased cold gas emission when $v_w > 1000$ km s^{-1}. For M series models only two simulations (M1_17 and M1_27) produced hard X-rays so I was not able to establish a relationship between wind speed and Δ. I note that the Hα emission calculated here represents a lower bound because I do not include ionizing radiation from the stellar disk, the starburst, and other sources.

The X-ray bands have the strongest relationship between wind velocity and Δ. While Hα has a similar relationship, measuring total Hα emission will be complicated by other sources of emission such as stars and disk material. Thus X-ray emission is preferred for establishing a blowout, the blowout strength, and wind speed when viewing starburst galaxies edge on.

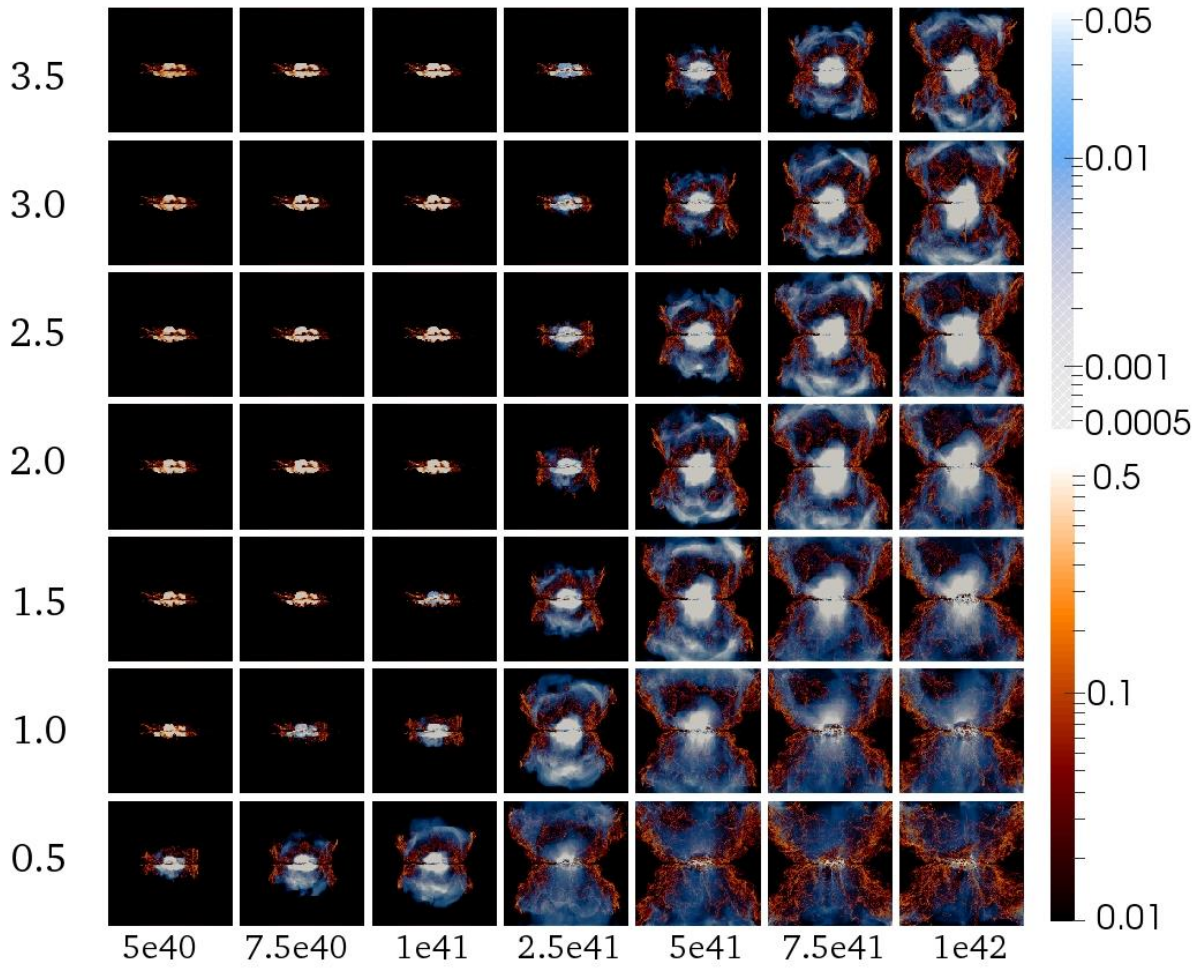

Figure 4.1: Low-resolution M1_XXT1 models at 1.5 Myr. Models are arrayed with increasing $\dot{M}$ (in $M_\odot$ yr^{-1}) vertical and increasing $\dot{E}$ (in erg s^{-1}) horizontal. Values on axes are the same as in Table 2.4 and correspond to indices in model numbers. Hα (red) and soft X-ray (blue) emission scaled as log(erg s^{-1} cm^{-2}) is shown.

4.1 How Does the Cooling Function Alter Emission?

I use three measures to determine how the different cooling limits affect the gas transported out of the galactic disk. I compare how T1 and T4 cooling affects the relation between v_w and gas mass in the lower halo ($z > 85$ pc), gravitationally unbound mass, and Δ.

Figure 4.2 shows that the different cooling limits do not affect Δ for soft and mid X-rays, whereas for Hα both Δ and κ differ drastically between series T4 and T1. For T4 models Hα emission in the disk is ten thousand times brighter than the lower halo, whereas for T1 models the disk is only ten times brighter. Cold gas in the lower halo ($< 10^2$ K) emits only in T1 models. Still, lower halo emission from cold gas remains 4-8 dex below that from the disk.

I sum the gas mass present in the lower halo ($z > 85$ pc) over the central 500 pc. I also sum the gravitationally unbound gas mass present in the disk and lower halo over the entire computational domain. Similar to Strickland & Stevens (2000) I consider gas to be gravitationally unbound if

$$|v_z(r,z)| + v_{therm}(r,z) > v_{escape}(r,z) \tag{4.2}$$

where $|v_z(r,z)|$ is the bulk velocity in each cell in the vertical direction, $v_{therm}(r,z) \equiv \sqrt{3k_BT(r,z)/m_H}$ and $v_{escape}(r,z)$ is the escape velocity for each cell. Figure 4.3 plots unbound gas mass and gas mass in the lower halo vs. wind speed v_w for both cooling limits. For $v_w > 500$ km s^{-1} there is no significant difference in the unbound mass for all temperature regimes between the T4 and T1 models. Below 500 km s^{-1} the T4 models still have $\sim 2 \times 10^5$ M$_\odot$ of unbound mass. This mass is hot, thermally unbound, non-ballistic gas. The artificially high cooling limit of the T4 models keeps the disk gas hot and thermally unbound.

Figure 4.3 reveals no difference in the total gas mass present in the lower halo between the T4 and T1 models. For all wind speeds, warm Hα emitting gas dominates in T4 models but not in T1 models. Gas mass decreases in both at high v_w because the models with highest wind speed have small $\dot{M}$ but large $\dot{E}$. Thus the wind, and by extension the lower halo, does not have as much mass.

Temperature-density plots in Figure 4.4 demonstrate differences in model series T1 and T4: three models (M2_43, M2_34, M2_25, with $\dot{M}$ $(2.0, 1.5, 1.0)$ M$_\odot$ yr^{-1}, and $\dot{E}$ $(1.0, 2.5, 5.0) \times 10^{41}$ erg s^{-1}) of series T1 are down the left column, and repeated for series T4 on the right. T4 models reproduce the Hα "shelf" at $\sim 10^4$ K of Strickland & Stevens (2000) and Creasey et al. (2013). The shelf is barely evident in T1 models. It comprises shocked gas cooling to much lower values. Reduced shelf mass explains reduced Hα gas mass in Figure 4.3.

Note the differing X-ray regime for model M2_43T1 vs. M2_43T4. In T1, cooling dominates and suppresses

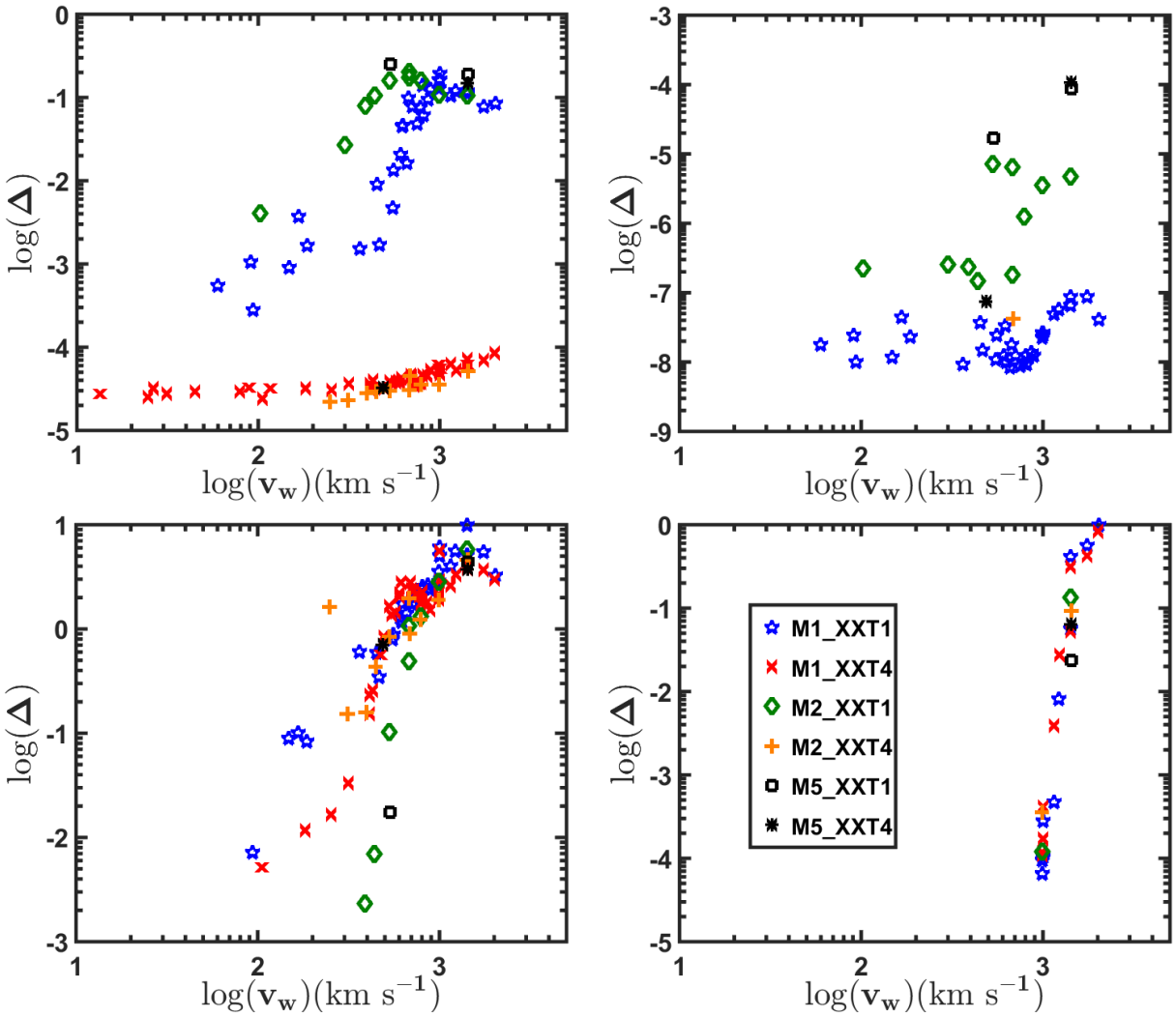

Figure 4.2: Total emission lower halo/disk (Δ) vs. simulated wind speed at 1.5 Myr for M series models. Counterclockwise from upper right: cold gas, Hα, soft X-ray, mid X-ray.

outflow as evidenced by an absence of hot gas in the lower halo. This model sits in the bottom of the intermediate regime shown in the inset in Figure 3.3.

4.2 Resolution

To examine the effect of resolution I ran my MX_34 and MX_27 models at three resolutions, and compared the wind velocities, lower halo mass, and unbound mass in the different temperature regimes. As noted in Section 2.5.2, the same initial density distribution was used for all models and was coarsened for the lower resolution models. Additionally my M5_27 and M2_27 models use the same parameters and resolutions as model numbers M01 and M04, respectively from Cooper et al. (2008).

For my MX_34 and MX_27 models I find no difference in wind velocity within the uncertainty once a

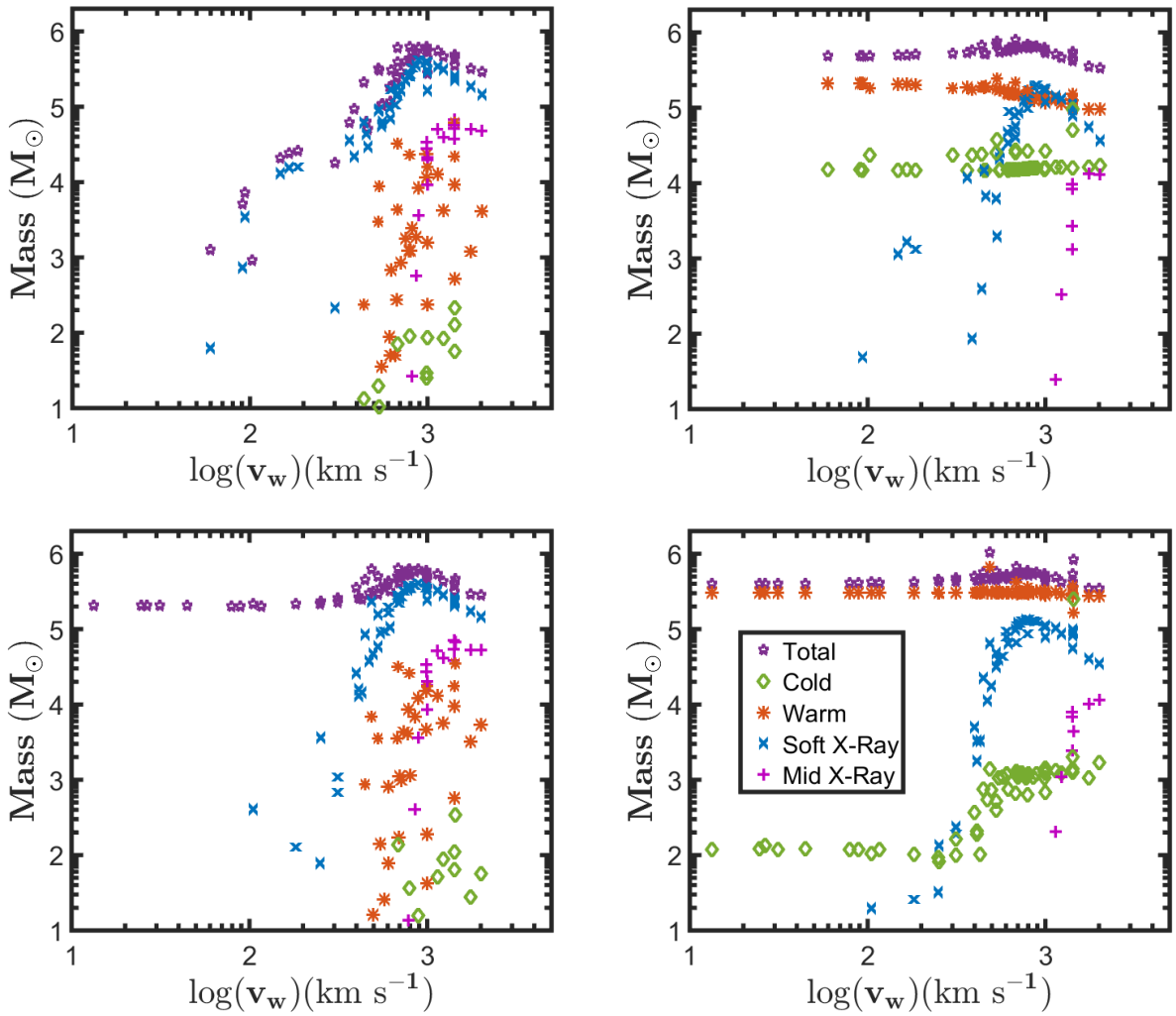

Figure 4.3: Gas mass vs. simulated wind speed for M series models. Graphs on the left show gas gravitationally unbound from the galaxy. On the right, gas present in the lower halo ($z > 85$ pc). Graphs on the top show T1 models, on the bottom T4 models. Mass measured at 1.5 Myr.

steady state wind had formed after 1.5 Myr. For all MX_34 models $v_w \approx 550$ km s^{-1} and for all MX_27 models $v_w \approx 1420$ km s^{-1}. As shown in Figure 3.3 for $v_w > 500$ km s^{-1} the relation given in Equation 3.2 holds irrespective of resolution. Thus the wind kinematics of a sufficiently powerful starburst are not affected by numerical resolution. But note, when $v_w < 500$ km s^{-1} (see Figure 3.3 insert) wind formation depends on the resolution. Lower resolution models may experience enhanced cooling due to greater average density from unresolved features. Thus for models on the edge of a blowout, increased resolution is important for determining if a galactic wind will form.

As shown in Figure 4.5, similar to the wind speed noted above, increased resolution does not significantly change the total unbound and lower halo mass, with the exception of the M1_34 model. The M1_34 model is

just above the limit of $v_w < 500$ km s^{-1} where resolution begins to affect the kinematics. This is evident as a slight decrease in the total unbound mass at the lowest resolution. The unbound mass of soft X-ray gas is not affected by resolution for both sets of models, but for my MX_34 models there is marked decrease in soft X-ray gas mass in the lower halo. This is due to the increased resolution of bow shocks and hot envelopes surrounding filaments, which decreases the amount of mass in that temperature regime. This effect is not seen in the MX_27 models because the superbubble has expanded to fill the entire lower halo volume. Here the mass contribution of bow shocks and hot envelopes surrounding filaments is not as significant. Related to this is an increase in unbound, warm, Hα emitting gas from ablata off of ballistic filaments. This corresponds to increased cold gas in the lower halo as higher resolution models form more well defined filaments containing cold gas.

Because there is not a significant difference in velocity and total outflow mass between my M2 and M5 models I determined that a grid resolution of 3.9 pc suffices for studying the effect of starburst and galaxy parameters on the resulting outflow. Thus for my series that employ SMR, I use a grid resolution of 3.9 pc on the highest refinement level.

4.3 Using Total Emission to Infer Starburst Properties

Figure 4.1 reveals increased X-ray emission with increasing mass loading. Using 2D and 3D models Strickland & Heckman (2009) inferred starburst properties of M82 using total X-ray emission from their models. Here I use my M and F series models to investigate the effect that $\dot{M}$, $\dot{E}$, the mass loading factor (β see eq. 2.17), and the thermalization efficiency (ϵ see eq. 2.16) have on the total emission from the superbubble in different temperature regimes as given in Table 2.1.

Figures 4.6 and 4.7 show total halo emission, defined as all emission from gas $z > 85$ pc, for my M series models. The models are arrayed as in Figure 4.1 with increasing $\dot{E}$ horizontal, and increasing $\dot{M}$ in the vertical, so that each "pixel" represents a single simulation. Figure 4.6 shows total emission from cold, warm and Hα emitting gas, while Figure 4.7 shows total halo emission from hot UV, soft, mid, and hard X-ray emitting gas.

Figures 4.8 and 4.9 are the direct analogs of Figures 4.6 and 4.7 but for my F series models. Instead of varying total energy ($\dot{E}$) and mass input ($\dot{M}$) directly as with series M, series F assumes a constant SFR with constant energy ($\dot{E}_{SN+SW}$) and mass ($\dot{M}_{SN+SW}$) from stellar winds and SN, and then varies ϵ and β. This employs the insight from Equation 3.5 that the wind velocity does not depend on the SFR, but only on ϵ and β. Thus Figures 4.8 and 4.9 plot total halo emission for different temperature regimes with each "pixel" being a single model. Models with increasing ϵ (ranging from 0.2-1.0) are horizontal and models with

increasing β (ranging from 1.0-10.0) are vertical.

With a SFR of 10 $M_\odot$ yr^{-1} , the $\dot{E}$ and $\dot{M}$ of my F10 series correspond roughly to the M series simulations in the two right most columns of Figure 4.1, the highest energy models, but with a larger total mass loading range. The absence of X-ray halo emission for models with high $\dot{M}$ and low $\dot{E}$ indicates that the outflow from the starburst has been quenched. Despite the absence of an outflow, the quenched models still have trace amounts of cold, warm and Hα emitting gas, while quenched models do not produce X-ray emission. Only three of my F series models had their outflows quenched, compared to 19 of my M series. In the quenched models cooling dominates to prevent a wind from forming.

In Figure 4.10 I compare soft and mid X-ray halo emission for my F10_XX_XX models with a SFR of 10 $M_\odot$ yr^{-1}, and my F50_XX_XX models with a SFR of 50 $M_\odot$ yr^{-1}. The F50 models have higher total halo emission, but as can be seen in the soft X-ray panels the same models are quenched regardless of SFR. A starburst with a higher SFR inputs more energy and this can be seen by comparing the mid X-ray emission. More models have mid X-ray halo emission.

Inside each panel of Figures 4.6, 4.7, 4.8, and 4.9 wind velocity increases from top left to bottom right, with the simulation situated in the bottom right corner having highest velocity. While the total halo emission from all bands generally increases with higher velocity winds, the models with the highest velocity outflows do not always have the highest total emission. This is evident for hot UV and soft X-ray emission from my M series, and is even more evident in all bands for my F series, with the exception of mid and hard X-rays. In all of these models, higher velocity is achieved by increasing $\dot{E}$ relative to $\dot{M}$, which increases the fraction of the gas at higher temperature. As gas is pushed to higher temperatures, total Hα, UV and soft X-ray emission is decreased, while mid and hard X-ray emission increases.

For both my M and F series, the greatest Hα, hot UV and soft X-ray emission comes from models with wind velocity $\sim$ 1500 km s^{-1}. Above this, the total halo emission and Δ decrease, indicating that the relationship between total emission and wind velocity given in Equation 4.1 only holds for Hα, hot UV and soft X-ray emission when wind velocities $< 1,500$ km s^{-1}. Above that point mid or hard X-ray emission can infer wind velocity and starburst properties such as $\dot{E}$ and $\dot{M}$ or ϵ and β for starburst galaxies.

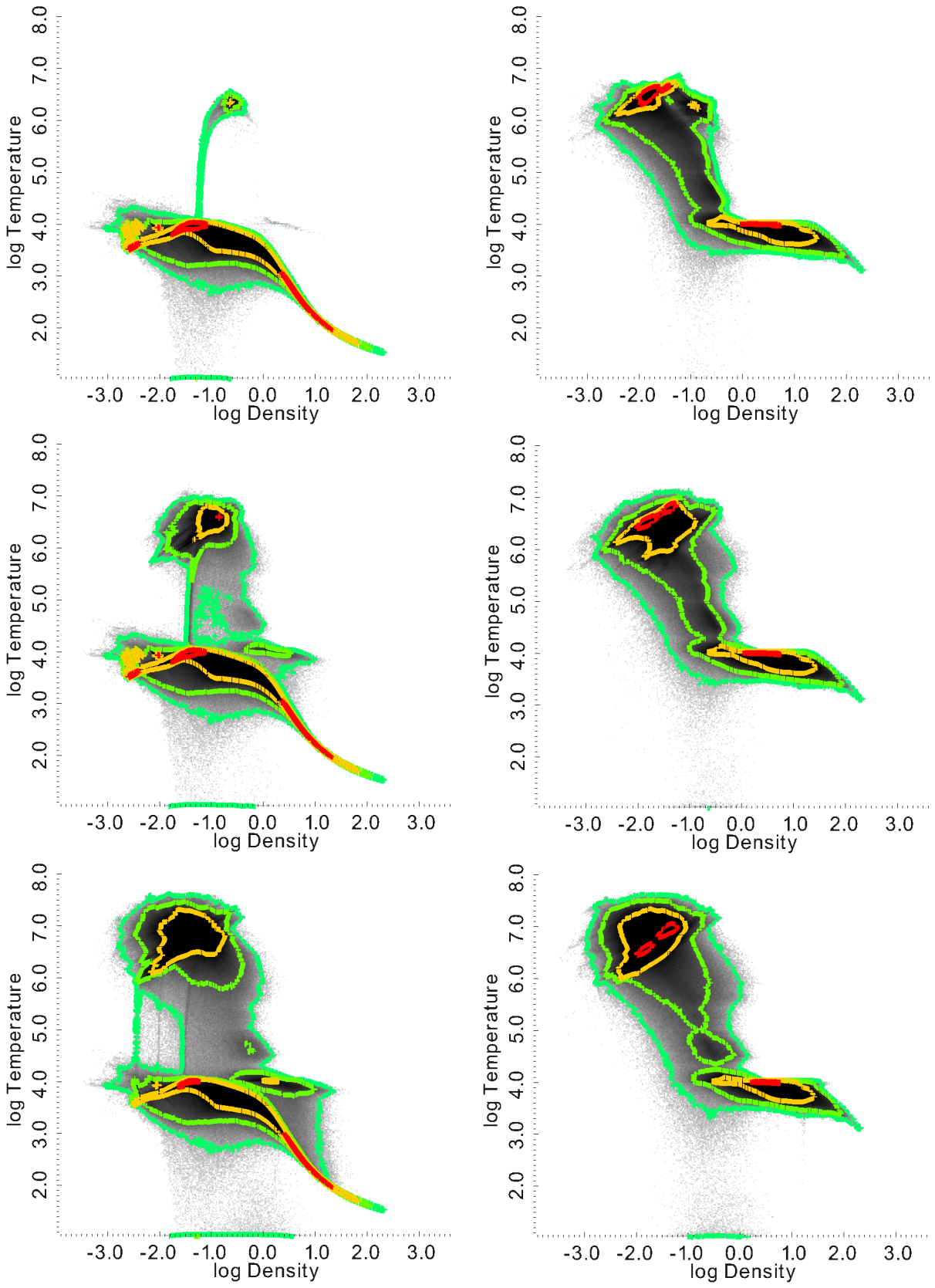

Figure 4.4: Lower halo gas mass in the temperature-density plane at 1.5 Myr. Left: T1 models, right: T4. Top to bottom: M2_43, M2_34 and M2_25. Contours at 10 (cyan), 10^2 (green), 10^3 (yellow), 10^4 (red) $M_\odot$.

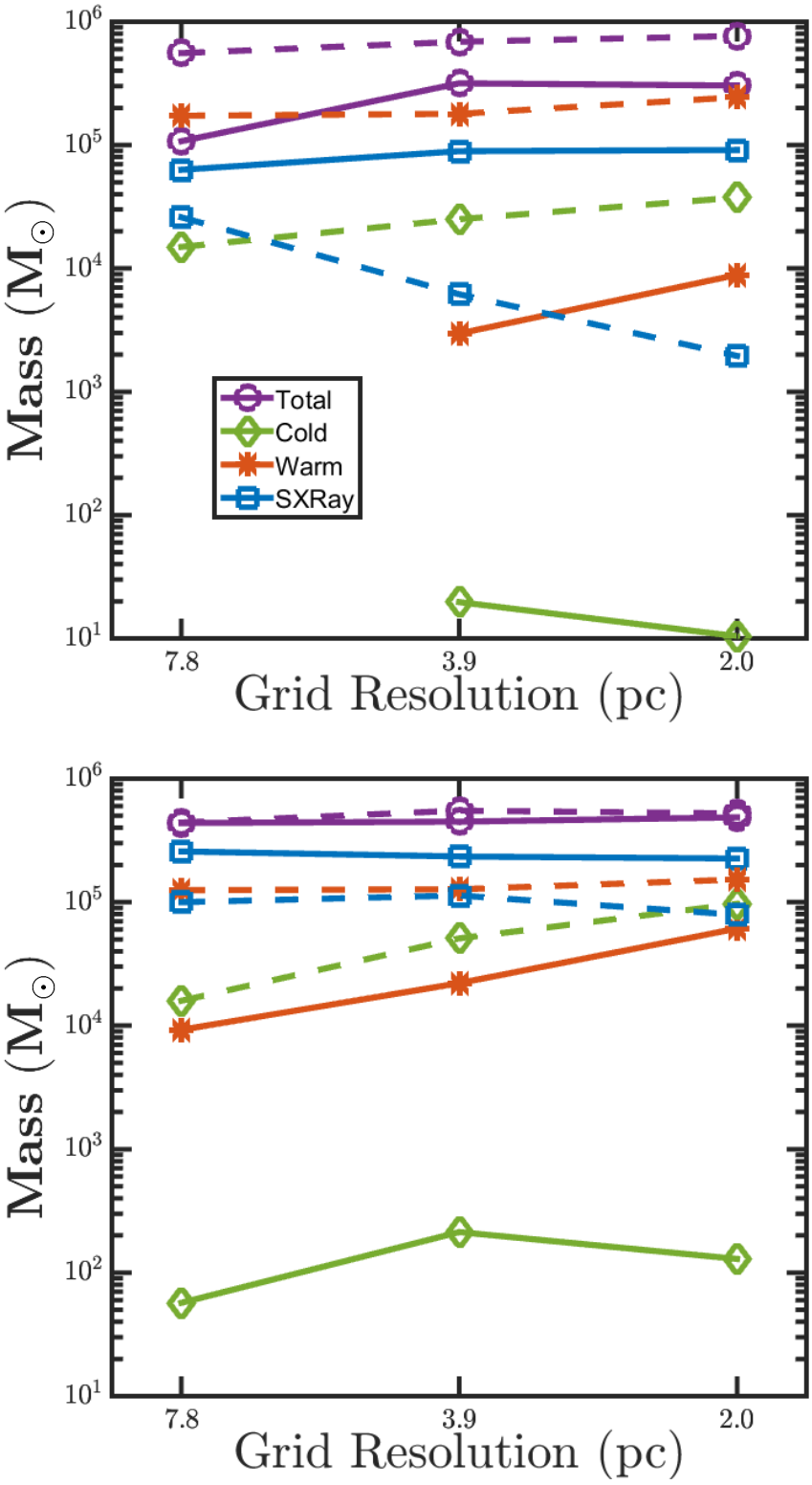

Figure 4.5: Lower halo and unbound gas mass at different grid resolutions. Solid lines indicate unbound mass, dashed lines indicate lower halo mass. Top MX_34T1 models, bottom MX_27T1 models.

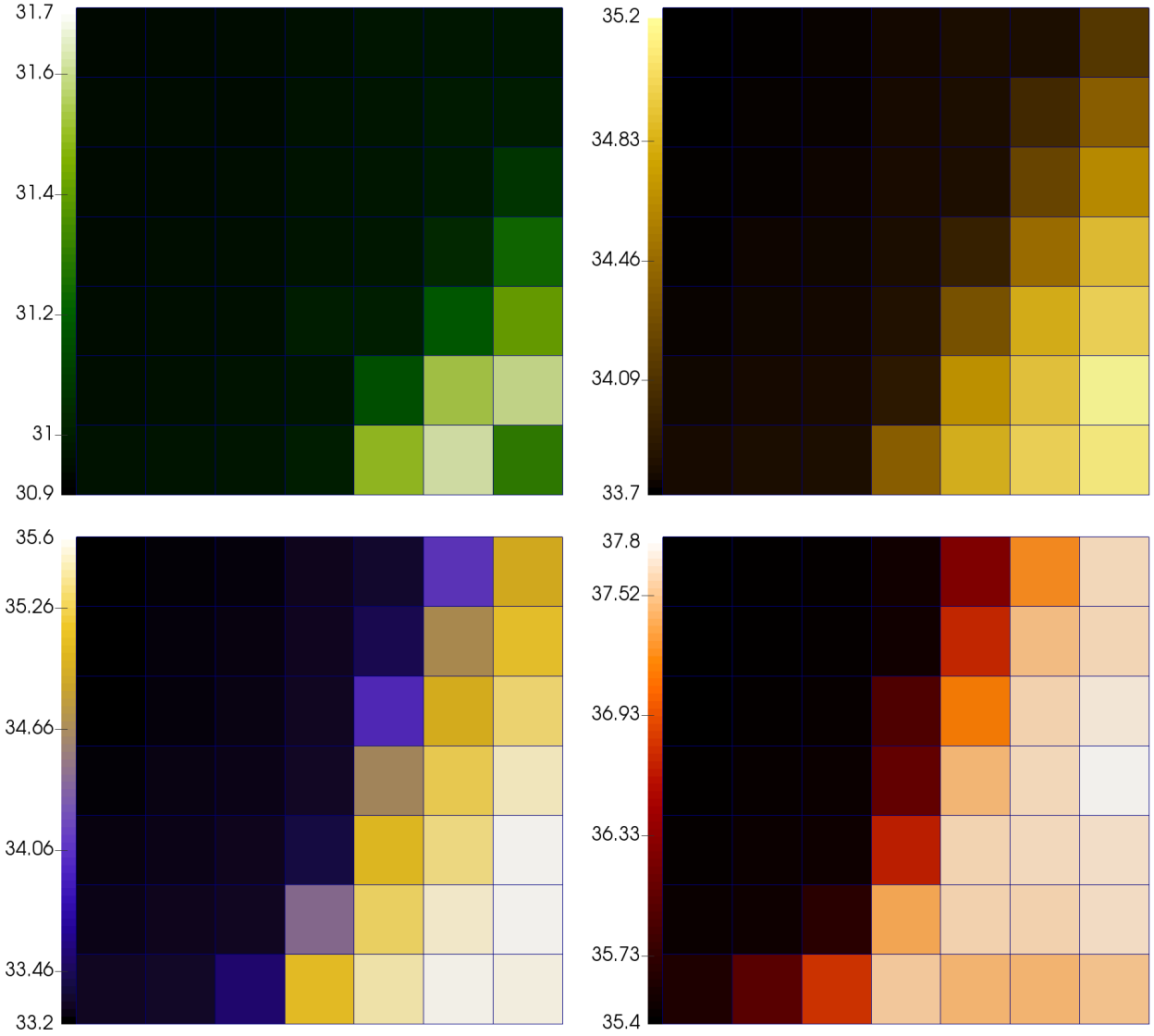

Figure 4.6: Total halo emission from M series models arrayed in same configuration as Figure 4.1 so that each "pixel" represents a single simulation, with increasing $\dot{E}$ horizontal, and increasing M in the vertical. Clockwise from top left total emission in erg s^{-1} for cold, warm low, Hα, warm high gas.

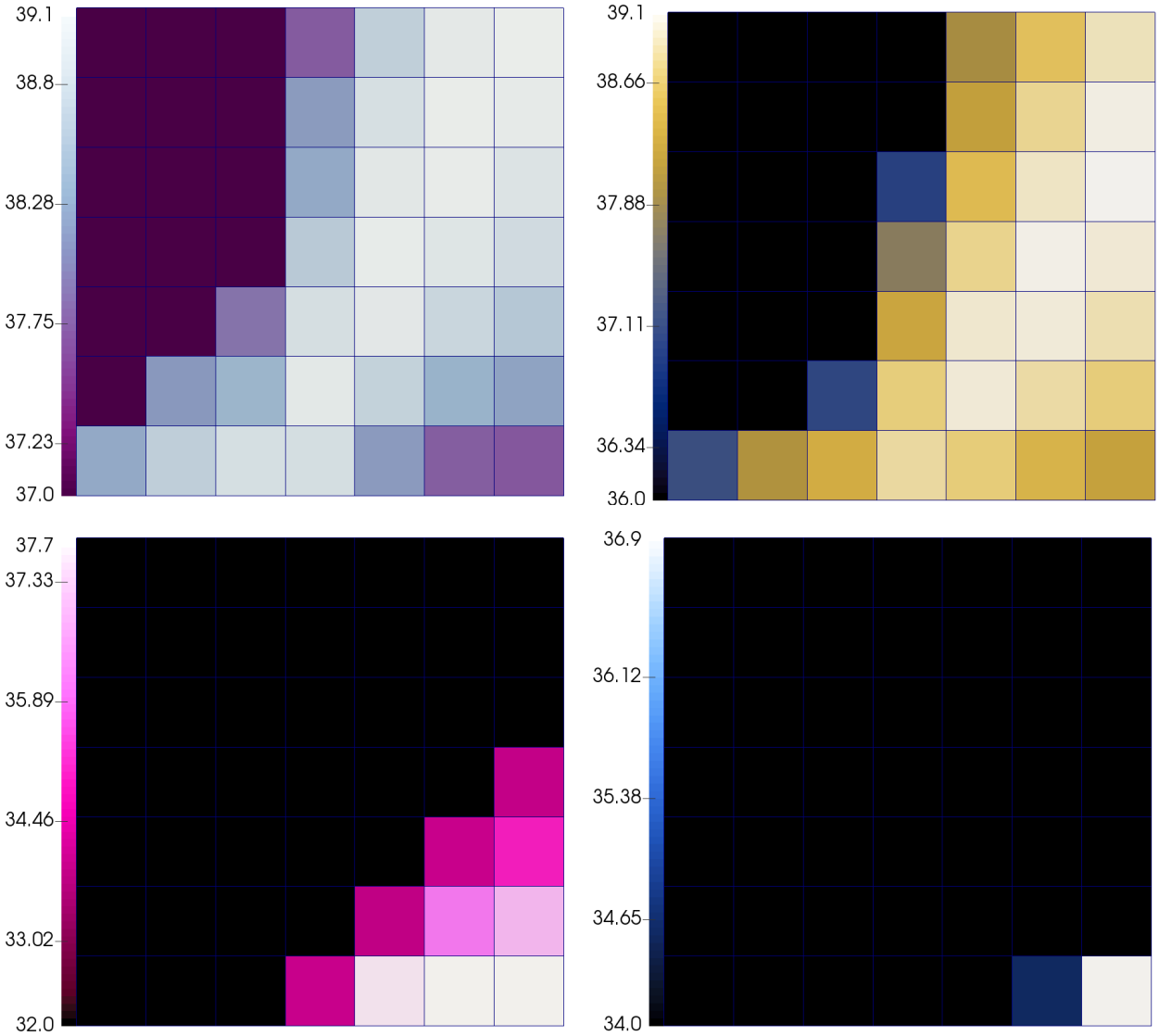

Figure 4.7: Total halo emission from M series models arrayed in same configuration as Figure 4.1 with increasing $\dot{E}$ horizontal, and increasing $\dot{M}$ in the vertical. Clockwise from top left total emission in erg s^{-1} for hot UV, soft X-ray, hard X-ray, mid X-ray gas. While the color bar assigned to each emission band has a lower limit, the actual emission from models at the lower limit is 0 erg s^{-1}. The lower limit has been set to just below the model with the lowest non-zero total emission.

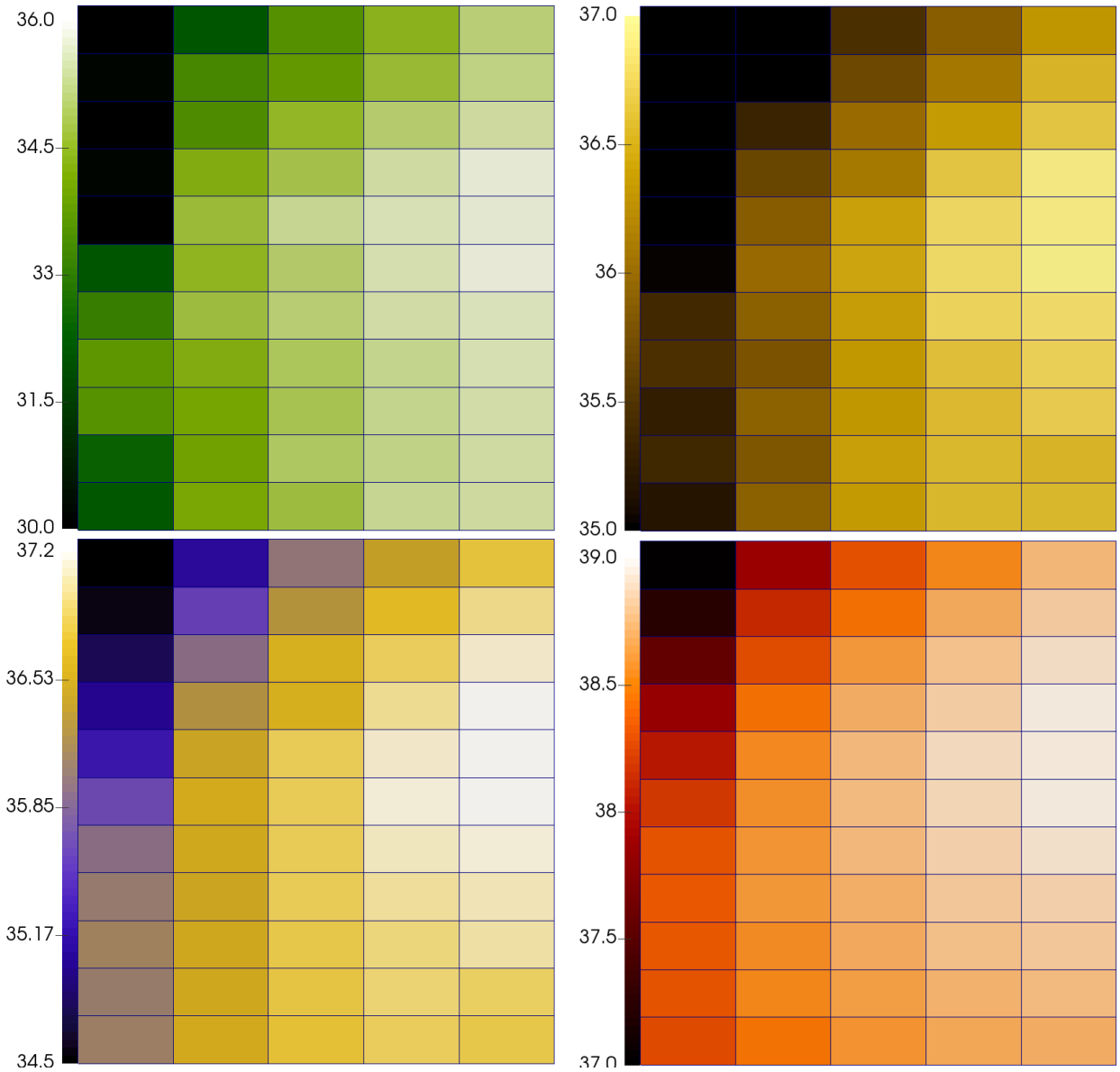

Figure 4.8: Total halo emission from F series models arrayed with increasing thermalization efficiency (ϵ) horizontal, and increasing mass loading factor (β) in the vertical. Clockwise from top left total emission in erg s^{-1} for cold, warm low, Hα, warm high gas. While the color bar assigned to each emission band has a lower limit, the actual emission from models at the lower limit is 0 erg s^{-1} with the exception of warm high gas emission. The lower limit has been set to just below the model with the lowest non-zero total emission.

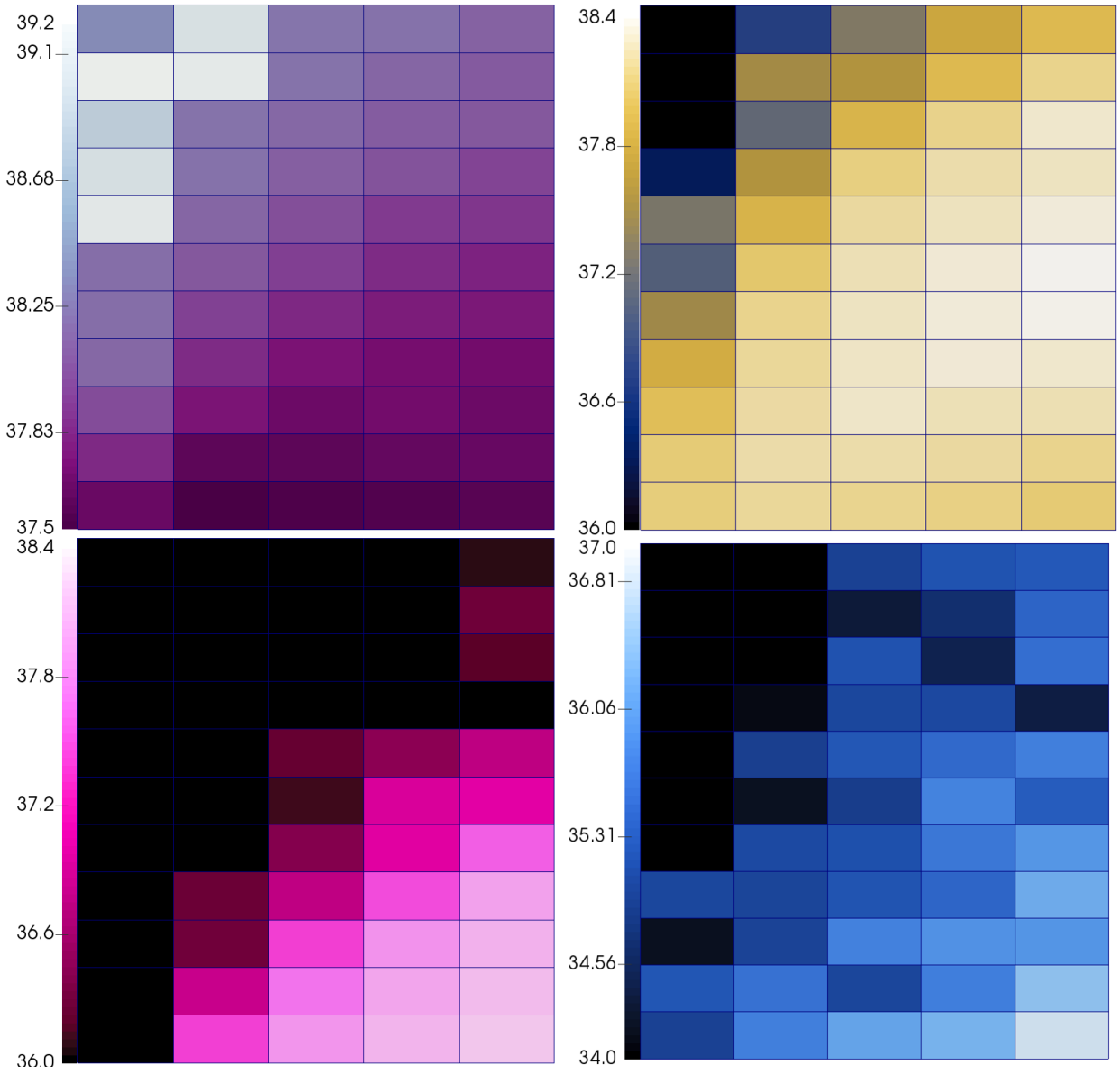

Figure 4.9: Total halo emission from F series models arrayed with increasing thermalization efficiency (ϵ) horizontal, and increasing mass loading factor (β) in the vertical. Clockwise from top left total emission in erg s^{-1} for hot UV, soft X-ray, hard X-ray, mid X-ray gas. While the color bar assigned to each emission band has a lower limit, the actual emission from models at the lower limit is 0 erg s^{-1} with the exception of hot UV gas emission. The lower limit has been set to just below the model with the lowest non-zero total emission.

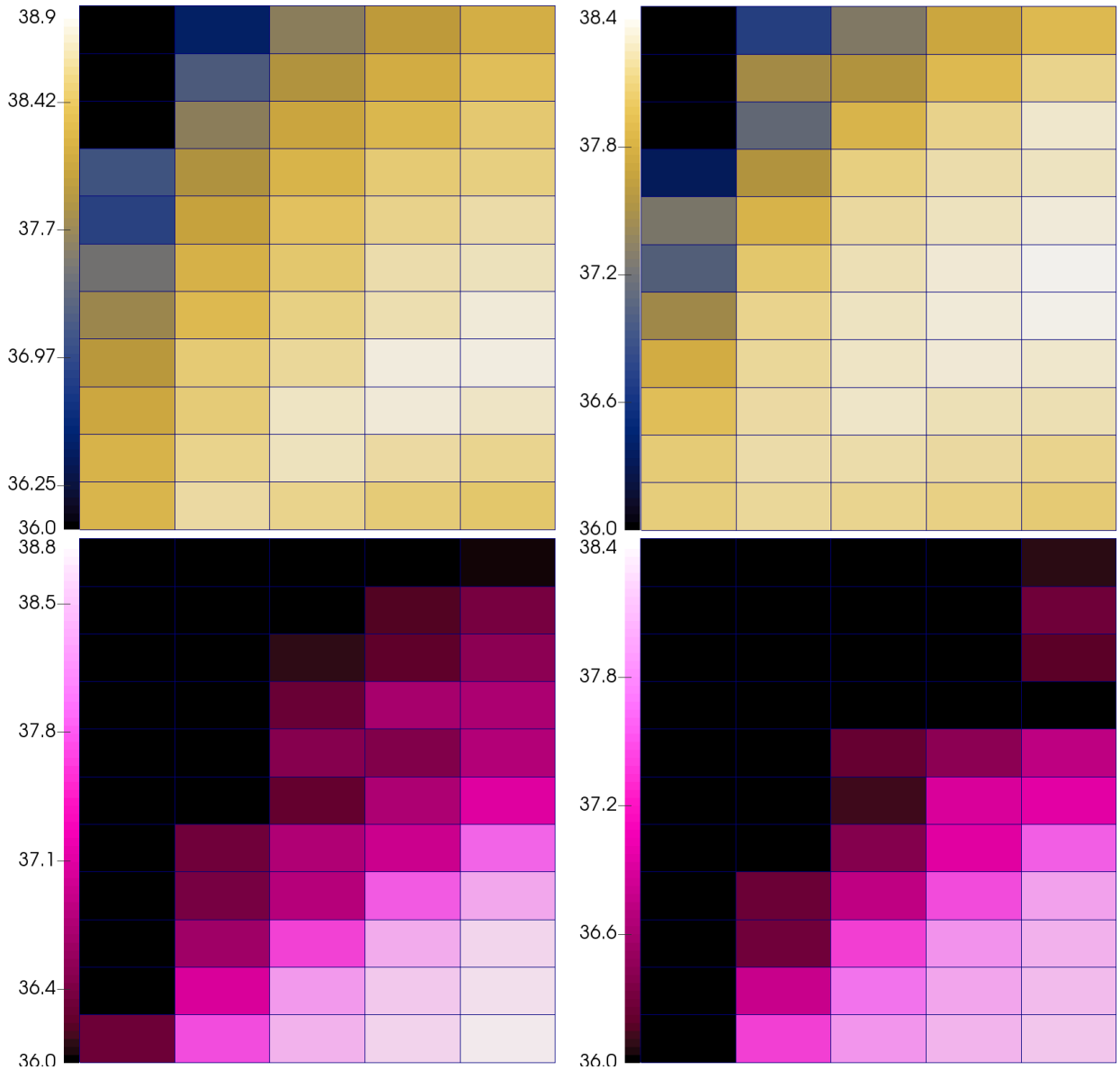

Figure 4.10: Panels on the right are soft and mid X-ray emission from Figure 4.9 from models F10_XX_XX with a SFR of 10 $M_\odot$ yr^{-1}. Panels on the left are from soft and mid X-ray emission from models F50_XX_XX with a SFR of 50 $M_\odot$ yr^{-1}.

CHAPTER 5: Embedded Filaments

5.1 Expanding Bubbles

Many GWs contain long optical and X-ray emitting filaments (Bland & Tully 1988; Veilleux et al. 1994; Shopbell & Bland-Hawthorn 1998; Devine & Bally 1999; Strickland et al. 1997, 2002). In my simulations, filaments appear by a combination of three processes.

1. Limb brightening from the shocked edge of the superbubble (Cecil et al. 2002).

2. Disruption of a cool dense cloud by the supersonic wind (Cecil et al. 2002; Cooper et al. 2009).

3. Merging bubbles that rise from the starburst region (Joung & Mac Low 2006; Melioli et al. 2013).

Limb brightened filaments appear in Figures 4.1 and 3.2 at the edge of the shocked region; they are broad ($100-200$ pc) without well defined boundaries. They have no significant vertical motion because they represent the edge of the wind region. Embedded in these regions may be smaller filaments formed through processes 2 and 3 as discussed below.

Cold dense clouds are overrun by the supersonic hot wind, which exerts a ram pressure on the cloud, disrupting it, stripping off material and elongating it into a filament. Examples of disrupted clouds can be seen in the density plots in Figures 3.1 and 3.2. While these disrupted clouds are present in my simulations, to fully resolve them would require resolution < 0.1 pc (see Cooper et al. (2009)) compared to my maximum of 2 pc.

Due to inhomogeneities in the starburst, multiple bubbles form that sweep up and squeeze the ISM. With continued expansion, the shells merge to coalesce the gas into thin ($<$ 50 pc) filaments. In my models, many of these filaments emit little Hα before dispersing within a Myr by shock heating and ablation, or disrupting by Kelvin-Helmholtz instabilities.

A few filaments persist when a cool dense cloud is present along the bubble merger interface. The additional mass allows the filament to persist longer before disrupting entirely. If the filament is anchored to a mass loading site within the starburst, the dense gas in the filament can be replenished continuously to survive for > 1 Myr and stretch for > 100 pc. Figure 5.1 sketches this last scenario, which is a combination of processes 2 and 3 above.

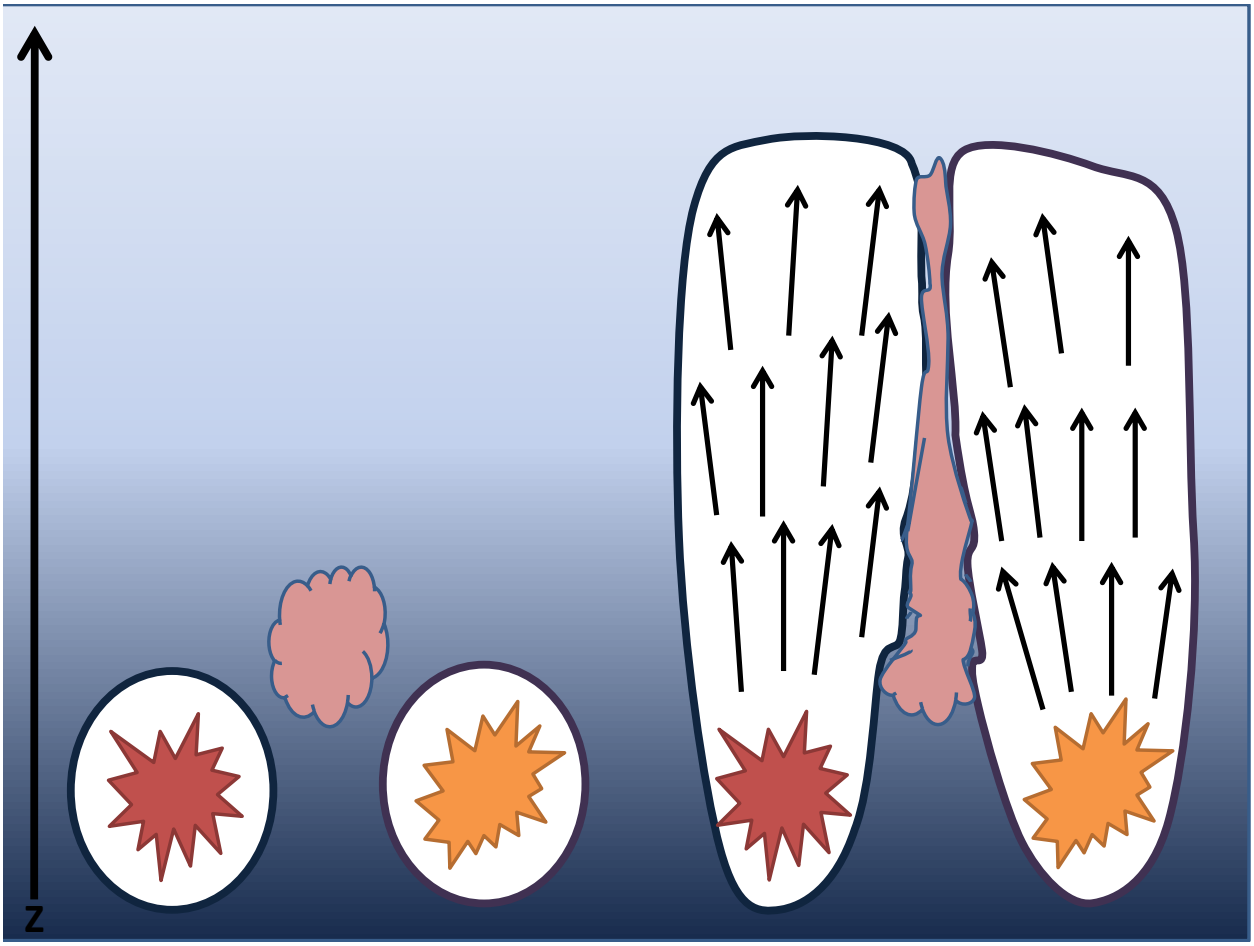

Figure 5.1: Cartoon of two merging superbubbles viewed side-on, combining filament formation scenarios 2 and 3. Their contact forms a filament from ISM swept up and compressed by the wind. To persist, this filament must be anchored to a mass loading source to continuously replenish its shocked, dense gas.

Figures 5.2 and 5.3 compare models M5_34T1 and M5_27T1 respectively to show examples of filaments forming through a combination of cloud disruption and merging bubbles. These filaments are embedded in a GW of $400 < v < 2000$ km s^{-1}. The densest material has a velocity of $\lesssim 50$ km s^{-1} whereas ablated material $200 < v < 500$ km s^{-1}. Thus the dense cores of the filaments are hardly moving with respect to the disk. The wind flows by, ablating and collimating the filaments. The velocity gradient of its ablata resembles the homologous $v(r) \propto r$ velocity gradient mapped in NGC 3079, although velocities are lower than the 1500 km s^{-1} observed (Cecil et al. 2001, 2002).

The strength of the GW determines how filaments evolve. I note two interesting cases outlined below.

5.2 Mass Anchors

Model M5_34T (Fig. 5.2) has sufficient energy to form a GW, but the wind does not disrupt all filaments. As shown in Figure 5.2, two distinct bubbles emerge from the central starburst. Their boundaries merge to form a dense filament that stretches > 100 pc back to anchor on the starburst reservoir. The 540 km s^{-1} wind ablates mass off the reservoir, and pushes it into the filament that by 1.5 Myr has extended > 400 pc above the disk plane to drift along at only $50 - 100$ km s^{-1}. Due to continual mass loading at its base, the filament stays anchored allowing it to persist and grow. At some point the filament should disrupt entirely due to either Kelvin-Helmholtz instabilities or heating and evaporation. But my resolution is insufficient to maximize filament survival time (see Cooper et al. 2009).

5.3 Filament Lift Off

In model M5_27T1 (Fig. 5.3) the filament again forms along the bubble contact. But now, after 1 Myr it detaches from the disk reservoir and lofts into the free-flowing wind of the now merged bubbles. This filament differs from its slow counterpart model M5_34T1; it has a larger cross section to the impinging wind, so it fragments more due to Kelvin-Helmholtz instabilities. The surrounding wind flows at 1420 km s^{-1} while the filament moves at $0 - 50$ km s^{-1} before lift off but attains $200 - 500$ km s^{-1} thereafter. This filament would be analogous to the disrupted clouds studied by Cooper et al. (2009).

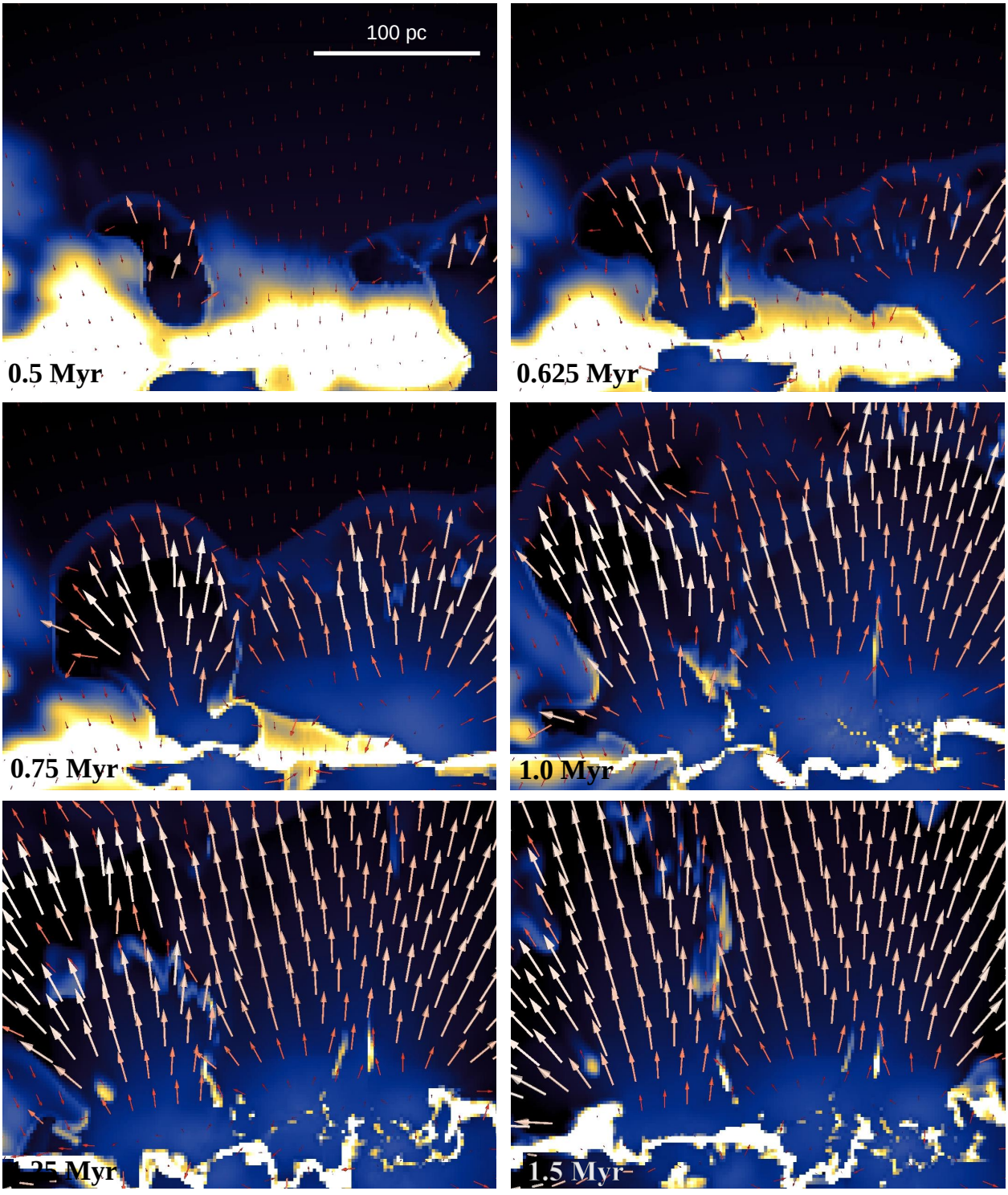

Figure 5.2: Close-up of the filament forming region delineated in Figure 3.1 (model M5_34T1, bottom right panel). The starburst covers the bottom third of each image. Red velocity vectors are $v_w \approx 20$ km s^{-1} and white $v_w \approx 500$ km s^{-1}. The filament is forming just left of center where the two bubbles are merging.

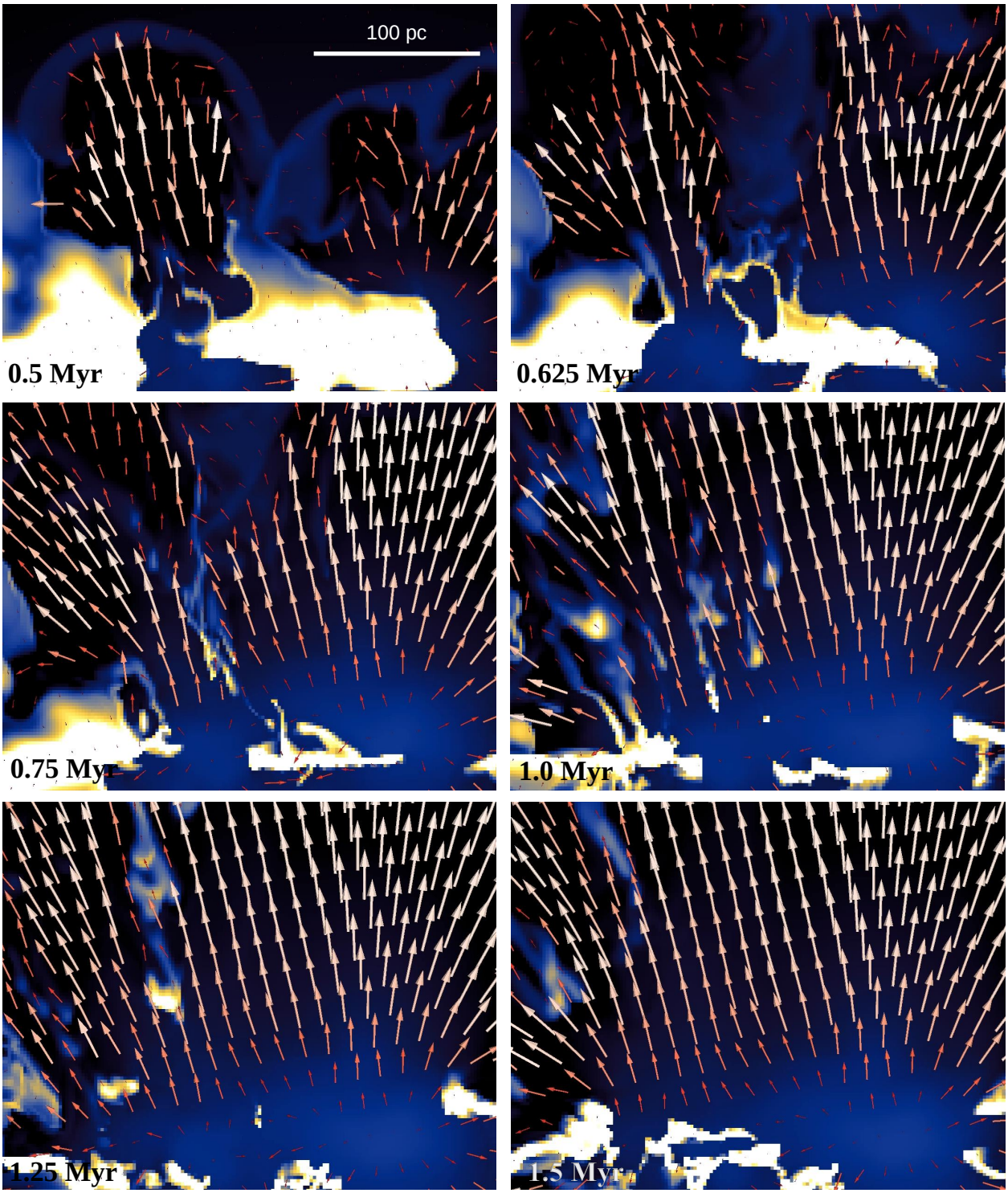

Figure 5.3: Same as Figure 5.2, for model M5_27T1. Velocity vectors are color-coded, ranging from 20 km s^{-1} to 1500 km s^{-1}.

CHAPTER 6: Synthetic Absorption Lines

In Chapter 4 I showed how total halo emission can be used to infer galactic wind velocity and starburst properties for edge on galaxies. For face on galaxies, absorption lines can probe kinematic properties of the three phase medium of the galactic wind. To probe cold, warm, and hot gas phases I synthesize absorption lines of various ions. Typically only the warm phase has been probed using absorption lines (Heckman et al. 2000; Martin 2005; Rubin et al. 2014; Chisholm et al. 2015, 2016), but more recent work (Ho et al. 2016, e.g.) and future surveys using ALMA and the Square Kilometer Array will focus on absorption from colder, molecular and atomic gas. All surveys cited above have noted the presence of asymmetric absorption profiles from warm and cold gas entrained in the galactic wind.

To help the interpretation of absorption profiles, I first use a simple formulation in Section 6.1 to generate asymmetric profiles seen in observations, then in Section 6.2 I give a more general formulation to generate absorption lines of specific ions, and finally in Section 6.3 I study relationships between SFR, SFR density ($\Sigma_{\rm SFR}$) and the analytic wind velocity.

6.1 Simple Absorption Profiles

For my simple formulation I synthesize absorption lines for three temperature regimes, denoted "molecular", "warm", and "soft X-ray", that correspond to the cold, Hα and soft X-ray temperature ranges in Table 2.1. A trivial, optically thin line source function suffices for kinematical signatures of the three temperature regimes. Absorption spectra are derived by integrating optical depth in N cells along the column viewed perpendicular to the disk

$$\tau(v_{ch}) = \sum_{i}^{N} \tau_i(v_{ch}). \tag{6.1}$$

The velocity channels have a resolution of 10 km s^{-1} and range from -1800 km s^{-1} to 200 km s^{-1}.

Absorption profiles are shown in Figure 6.1 for models M5_27T1 (top panel) and M5_34T1 (bottom). The "soft X-ray" line shows the structure of the hot free-wind inside the expanding bubble. The velocity at maximum absorption is the average speed of the free wind. The long tail of the profile back toward galaxy systemic velocity, especially prominent in model M5_27T1, reveals hot gas being accelerated off of warm filaments. Hot gas flowing radially at the average speed of the free wind but not entirely along our line of sight also contributes to the asymmetry of the line. Determining which of these two processes dominates

the asymmetry would require running additional models to study how the number of filaments affects line asymmetry. My K series used initial conditions that produced more filaments than my M series and as seen in Figure 6.5 the absorption line from hot gas does not have as much asymmetry. This would indicate that the asymmetry of absorption lines in hot gas depends more on the number of filaments in the wind. Model M5_34T1 shows two spikes in this absorption profile. The faster spike corresponds to the free wind inside the expanding bubble, the slower to absorption in the bubble shell. This shell has left the computational grid in model M5_27T1.

The "warm" line traces filaments and clouds caught in the gas but moving much slower, so maximum extinction is at much lower velocity. The long tail of this profile traces ablata accelerating off the filaments.

The "molecular" line shows a similar tail, although that absorption is more varied because multiple clouds contribute. In both the "warm" and "molecular" profiles shown in Figure 6.1 there is absorption at positive velocities. These features result from clouds initially at the edge of the lower halo, but not directly above the starburst. They were perturbed by the shock from the starburst but not blown out by it and have begun to fall towards the disk. For absorption from an arbitrary ion found in the neutral medium, I would expect an acceleration tail similar to that in the warm and molecular lines.

The asymmetric "warm" and "molecular" absorption line profiles are similar to observed Si II, Si III, O I, C II (see Wofford et al. 2013, Fig. 11, especially KISSR 242 and KISSR 1578), and Lyα (see Jones et al. 2012, Figs. 5 and 6) profiles in starburst galaxies. The shape also matches analytical predictions (Scarlata & Panagia 2015).

6.2 Full Absorption Profiles

I now calculate absorption profiles for specific ions to probe the kinematics of the three phase medium in the galactic wind.

The absorption coefficient for a single velocity channel (v_{ch}) is,

$$\kappa(v_{ch}) = N(v_{ch})a(v_{ch}) \tag{6.2}$$

where $N(v_{ch})$ is the column density and $a(v_{ch})$ is the absorption per atom. Assuming contributions from Doppler broadening and spontaneous radiative transitions $a(v_{ch})$ is given as,

$$a(v_{ch}) = \frac{\pi e^2}{m_e c}\frac{1}{\sqrt{\pi}}\frac{1}{\Delta\nu_{1/2}} f H(v_{ch}). \tag{6.3}$$

Here m_e is the mass of an electron, c is the speed of light, $\Delta\nu_{1/2}$ is the half width half maximum (HWHM) of

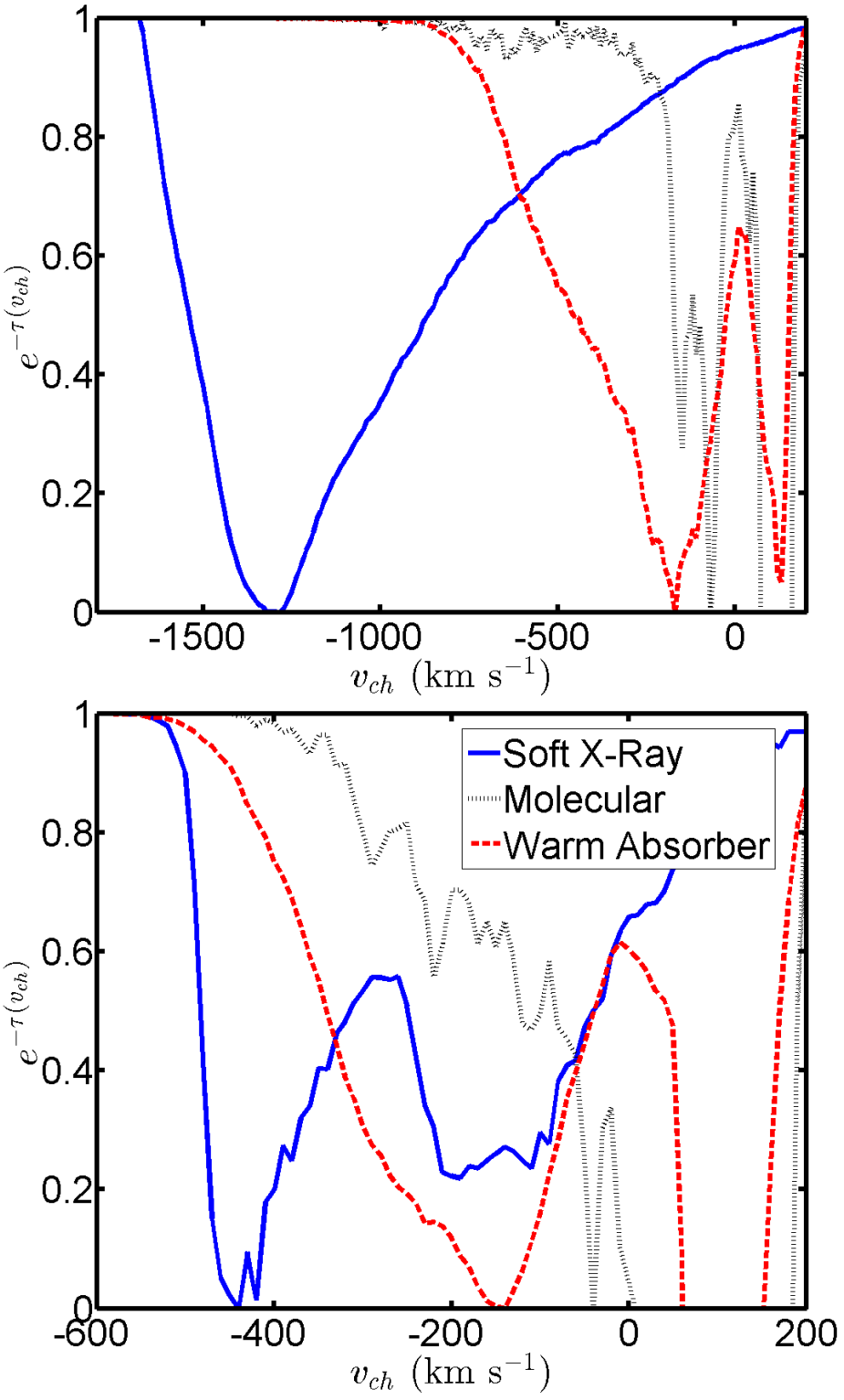

Figure 6.1: Synthetic absorption line profiles for model M5_27T1 (top) and M5_34T1 (bottom). Absorptions are calculated for "soft X-ray", "molecular", and "warm" gas. Vertical normalization is arbitrary.

the Gaussian component, f is the oscillator strength, and $H(v_{ch})$ is a Voigt profile. The Gaussian HWHM is calculated using Equation 5.70 from Kwok (2007),

$$\Delta\nu_{1/2} = \frac{2}{c}\sqrt{\frac{2k_BT}{m}\ln(2)}\nu_0 \tag{6.4}$$

with k_B Boltzmann's constant, T the gas temperature, m the atomic mass of the ion, and ν_0 the frequency of the line center from the NIST Atomic Spectra database (Kramida et al. 2015). I calculate the Voigt profile ($H(v_{ch})$) using Matlab code[1] written by Dr. Nikolay Cherkasov that employs the method of Schreier (2011). The method uses the complex error function to quickly generate an approximate Voigt profile using the HWHM of the Gaussian and Lorentzian components. The Lorentzian HWHM comes from the sum of all possible Einstein coefficients (Einstein 1905) that gives the transition strength for each quantum level (Kwok 2007, see eq. 5.59). Transition and oscillator strengths of each line are in the NIST Atomic Spectra database. An example of a Voigt profile is shown in Figure 6.2.

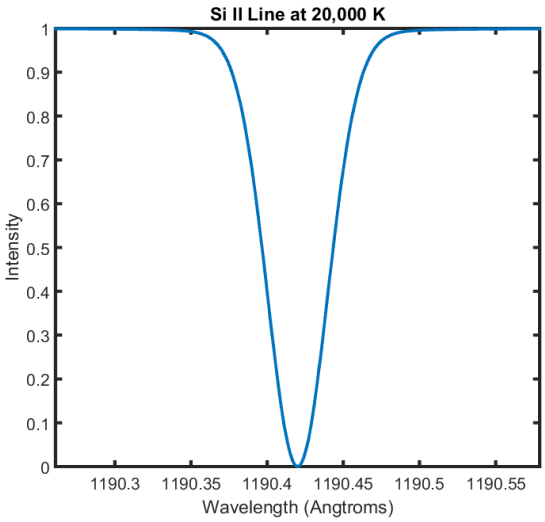

Figure 6.2: Example of a Voigt profile for the 1190 Å Si II line at 20,000 K.

I calculate a normalized Voigt profile for the gas in each cell directly above the starburst ($z > 100$ pc) and the profile is Doppler shifted using the z velocity of the gas in the cell. The Doppler shift for each cell is calculated with respect to the systemic velocity of the galaxy, with negative velocities toward the observer and positive velocities away from the observer. All calculations assume face on orientation to the galactic disk. I then calculate an absorption coefficient for each cell (Eqn. 6.2) using the ion density, which depends

[1]http://www.mathworks.com/matlabcentral/fileexchange/45058-deconvolution-mordenite-zeolite

on the cell density and the ionization fraction (Mazzotta et al. 1998). Examples of the computed ionization fractions for Si I-XIII are shown in Figure 6.3. I then use the absorption coefficient for each cell for each to calculate the optical depth using,

$$\tau_i(v_{ch}) = \kappa_i(v_{ch})dz. \tag{6.5}$$

The optical depth is then summed along the line of sight. The absorption profile for a given ion along a line of sight is,

$$I(v_{ch}) = I_0(v_{ch})\mathrm{e}^{-\tau(v_{ch})} \tag{6.6}$$

The resulting profile is then averaged over all lines of sight directly over the starburst and then re-normalized. Figure 6.4 gives an example of a synthetic absorption profile for the O I 1302.17 Å line. I use a channel resolution of $\Delta v_{ch} = 0.25$ km s^{-1}.

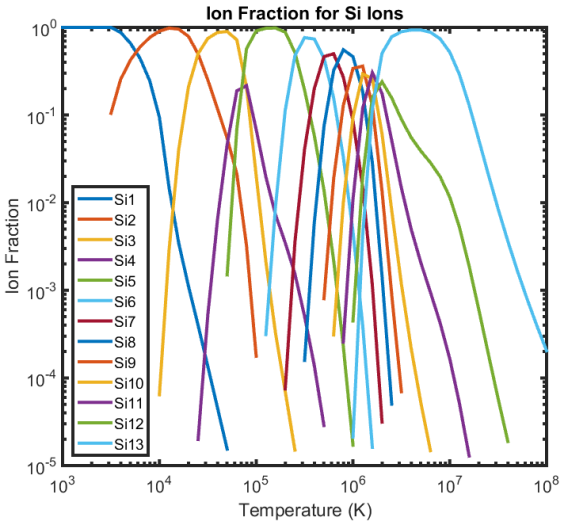

Figure 6.3: Ionization fractions for Silicon ions (Mazzotta et al. 1998).

Following the method of Chisholm et al. (2015) I calculate the $v_{\rm cen}$ and v_{90} velocities from the line. The $v_{\rm cen}$ velocity at half of the FWHM, and v_{90} is the velocity where the absorption profile returns to 90% of full intensity. Thus $v_{\rm cen}$ measures the bulk velocity of the absorbing gas for a particular temperature range and gas phase, and v_{90} measures the maximum velocity of the gas phase and temperature range. I use these velocity measures to determine relationships between gas in the galactic wind and starburst and galaxy properties.

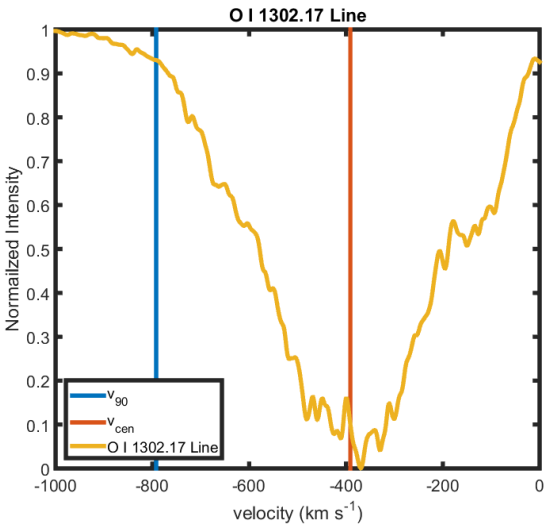

Figure 6.4: Synthetic absorption profile for the O I 1302.17 Å line. S_20_100 model with an analytic wind velocity of 2,000 km s^{-1} and a SFR of 10 M$_\odot$ yr^{-1}. Vertical lines indicate $v_{\rm cen}$ and v_{90} velocities.

6.3 Relationships from Absorption Profiles

In this section I use my K, S, and R series to investigate the relationships between $v_{\rm cen}$ and v_{90} velocities, and the analytic wind velocity (v_A from Equation 3.1), the SFR, and the SFR density ($\Sigma_{\rm SFR}$), along with the outflow velocities of the multi-phase medium.

In Figure 6.5 I plot synthetic absorption lines for Si I, II, VII, and XIII. These four lines probe gas temperature ranges corresponding to $< 1e4$ K, $1e4 - 2.5e4$ K, $4.5e5 - 7e5$ K, and $2e6 - 1e7$ K respectively. The gas producing the Si I and II absorption lines is moving $\sim$ 300 km s^{-1} slower than the hotter gas producing Si VII and XIII absorption. In Chapter 5 I noted that the dense gas inside the filaments is moving much slower than the hot, diffuse gas. That same difference in velocity is observed here in my synthetic Si lines. The difference between the Si I and XIII lines is even greater if we consider the v_{90} velocities, a difference of $\sim$ 700 km s^{-1}.

Additionally the Si I and II lines have a jagged shape created by cold and warm gas that is fragmented and clumpy. This is due to the presence of several filaments inside the wind region. Measurable absorption at zero and positive velocities results from gas inside dense cores embedded in the filaments. These cores have been elevated above the galactic disk but their vertical movement has stalled causing them to appear to move at the systemic velocity of the galaxy. As these cores are disrupted, the cold gas is ablated and accelerated to a higher velocity while being heated by the wind. This produces the asymmetric profiles of the Si I and II lines, as observed in several galaxies (Jones et al. 2012; Wofford et al. 2013; Chisholm et al. 2015).

The Si VII and XIII lines are also asymmetric but smooth. The smooth shape indicates that the hot gas transitions seamlessly through different velocities as it accelerates from the galaxy. Because the hot gas fills the inside of the superbubble, it is not fragmented and clumpy unlike the cold gas. The asymmetries are still present due to the hot gas being accelerated as it moves off of the plane of the galaxy.

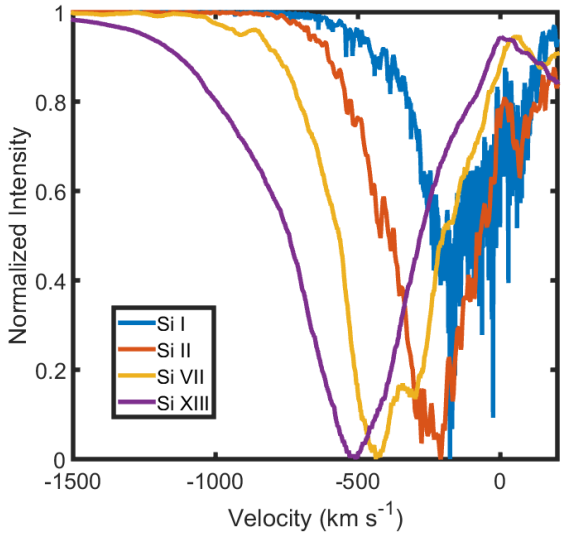

Figure 6.5: Synthetic absorption lines for Si I, II, VII, and XIII from my K_15_1800 model, which has a v_A of 1800 km s^{-1}.

To understand how the velocity of the gas changes with increasing temperature, I plot in Figures 6.6 and 6.7 the $v_{\rm cen}$ and v_{90} velocities respectively for Si I-XIII from my S series models. The plots include data from models with v_A of 1000, 1500, and 2000 km s^{-1} at SFR of 10, 50, and 100 M$_\odot$ yr^{-1}.

In Figure 6.6 we see three distinct velocity regimes corresponding to Si I-II, Si III-XI, and Si XII-XIII. These correspond to temperatures $< 2.5e4$ K, $2.5e4 - 2e6$ K, and $> 2e6$ K, respectively. As is noted by Equation 3.5, the wind velocity does not depend on the SFR. For models with $v_A = 1000$, 1500 km s^{-1} there is no significant difference in $v_{\rm cen}$, except for the model with SFR 10 M$_\odot$ yr^{-1} and $v_A = 1500$ km s^{-1}. In this case the $v_{\rm cen}$ for the midrange ions is ~ 200 km s^{-1} lower than the models with SFR 50 or 100 M$_\odot$ yr^{-1}. For models with $v_A = 2000$ km s^{-1} there is a difference in $v_{\rm cen}$ for all ions and for all SFR with increasing velocity for increased SFR.

In Figure 6.7 I show the v_{90} velocities for the same models as in Figure 6.6. A similar trend is evident with the three distinct velocity regimes, though less obvious for models with $v_A = 1000$. The velocities for different SFR are similar, indicating that the maximum velocity for a giving ion depends on the wind velocity not the SFR. The only exception is for low SFR where cooling may dominate.

Figure 6.8 plots the v_{90} velocity of Si IV for my S series models. This measures how the maximum

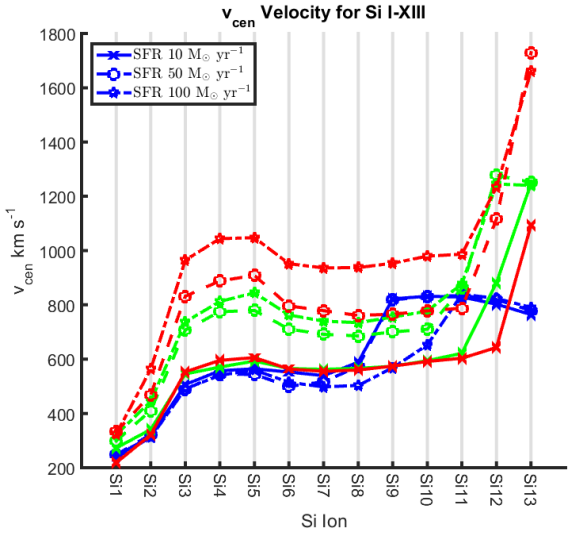

Figure 6.6: The $v_{\rm cen}$ velocity of all Si ions for select S series models. Blue lines are for models with $v_A = 1,000$ km s^{-1}, green for $v_A = 1,500$, and red for $v_A = 2,000$. Solid lines with 'x' indicate models with SFR of 10 M$_\odot$ yr^{-1}, dashed lines with circles indicate a SFR of 50 M$_\odot$ yr^{-1}, and dot dashed lines with pentagrams indicate models with SFR of 100 M$_\odot$ yr^{-1}.

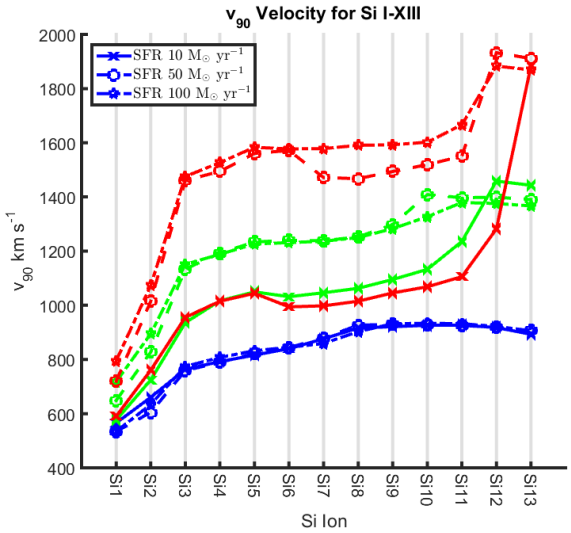

Figure 6.7: The v_{90} velocity of all Si ions for select S series models. Blue lines are for models with $v_A = 1,000$ km s^{-1}, green for $v_A = 1,500$, and red for $v_A = 2,000$. Solid lines with 'x' indicate models with SFR of 10 M$_\odot$ yr^{-1}, dashed lines with circles indicate a SFR of 50 M$_\odot$ yr^{-1}, and dot dashed lines with pentagrams indicate models with SFR of 100 M$_\odot$ yr^{-1}.

velocity of the warm gas is affected by different v_A and SFRs. For a given v_A, the v_{90} velocity increases with increasing SFR until $\lesssim 0.8 v_A$. But according to Equation 3.5 the outflow velocity should not depend on the SFR.

To resolve this dilemma in Figure 6.9 I plot the v_{90} velocity of Si XIII for my S series models. This shows that the maximum outflow velocity of the hot gas does not depend on the SFR. Therefore Equation 3.5 is

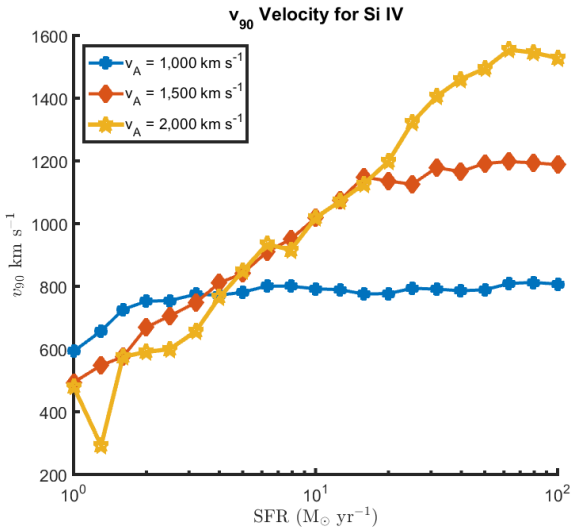

Figure 6.8: The v_{90} velocity for Si IV vs SFR for all S series models.

still satisfied. For hot gas, the v_{90} velocity is roughly constant at $\lesssim 0.9v_A$ for all SFRs. But as we see from Figure 6.8, the warm gas does depend on the SFR while $v_{90} \lesssim 0.8v_A$.

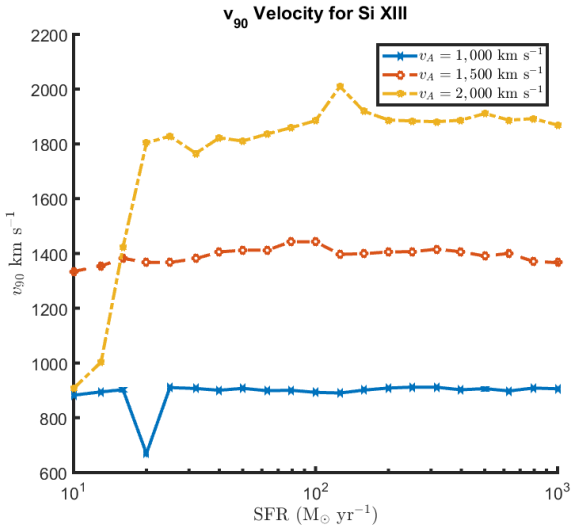

Figure 6.9: The v_{90} velocity for Si XIII vs SFR for all S series models.

To compare my results to observations, I plot in Figure 6.9 the v_{90} velocity of Si IV (same data as in Figure 6.8) on a log-log scale, and perform a linear fit to the data. I fit each set of models with the same v_A then fit all three combined. These fits give the following scaling relationship,

$$v \propto \mathrm{SFR}^{\delta} \tag{6.7}$$

The scaling relation is steepest for models with a $v_A = 2,000$ km s^{-1} ($v_{\rm cen} \propto {\rm SFR}^{0.351\pm0.081}$) and nearly flat for models with a $v_A = 1,000$ km s^{-1} ($v_{\rm cen} \propto {\rm SFR}^{0.136\pm0.076}$). For all data combined the fit falls between those two extremes ($v_{\rm cen} \propto {\rm SFR}^{0.248\pm0.044}$). In Tables 6.1 and 6.2 I give scaling relationships for Si I-IV, and XIII $v_{\rm cen}$ and v_{90} velocities, for my three sets of v_A values in my S series models, and fit values for all combined S series models.

The δ values of the fits for my low v_A models are consistently lower than the high v_A models. If I fit exclusively galaxies with $v_{90} < 0.75 v_A$, I get consistent δ values that range from $.3 - .4$ for the ions Si I-IV, with Si I having $\delta \sim .4$ and Si IV $\delta \sim .3$. Thus colder gas has a greater δ value than warmer gas.

From their spectra, Rupke et al. (2005) find $v_{90} \propto {\rm SFR}^{0.21}$, Martin (2005) find $v_{\rm cen} \propto {\rm SFR}^{0.35}$, Weiner et al. (2009) find $v_{90} \propto {\rm SFR}^{0.38}$, and Chisholm et al. (2015) find $v_{\rm cen} \propto {\rm SFR}^{0.22}$. Martin (2005) and Weiner et al. (2009) used samples of ULIGs or high red-shift luminous galaxies, while Rupke et al. (2005) and Chisholm et al. (2015) studied local starburst galaxies. Based on my results, the lower fit values come from a combination of starbursts with high and low mass loading factors, and therefore a mix of terminal outflow velocities. In contrast, the samples with higher fit values come from galaxies with exclusively low mass loading factors, and exclusively high velocity winds.

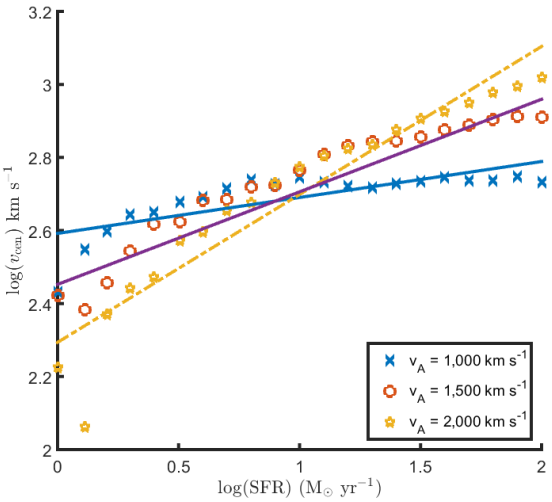

Figure 6.10: The $v_{\rm cen}$ velocity for Si IV vs SFR for all S series models. Fit lines are shown for $v_A = 1,000$ (blue), $v_A = 2,000$ (yellow) models and for all models together (purple). Fit coeficients are shown in Table 6.1.

Using my R series I look at how $\Sigma_{\rm SFR}$ affects the outflow velocity. As seen in Figures 6.11 and 6.12 for a constant SFR the outflow velocity for all Si ions decreases with increasing starburst radius. But the three phase structure of the outflow is still present. As can be seen in Figures 6.13, 6.14 and 6.15 there is a relation between $\Sigma_{\rm SFR}$ and $v_{\rm cen}$ until $\Sigma_{\rm SFR} \approx 10^{-3}$ M$_\odot$ yr^{-1} pc^{-2}, where the relation flattens out. This appears to

Table 6.1: Fit data for v_{cen} velocities from the S series.

Ion	v_A (km s^{-1})	Slope (δ)	Intercept (γ)
Si I	1,000	0.131 ± 0.040	2.045 ± 0.084
Si I	1,500	0.212 ± 0.042	1.952 ± 0.088
Si I	2,000	0.261 ± 0.035	1.857 ± 0.072
Si I	All	0.201 ± 0.029	1.951 ± 0.060
Si II	1,000	0.136 ± 0.065	2.157 ± 0.140
Si II	1,500	0.221 ± 0.047	2.043 ± 0.100
Si II	2,000	0.293 ± 0.051	1.912 ± 0.110
Si II	All	0.217 ± 0.036	2.037 ± 0.075
Si III	1,000	0.124 ± 0.070	2.385 ± 0.150
Si III	1,500	0.275 ± 0.053	2.135 ± 0.110
Si III	2,000	0.323 ± 0.052	2.051 ± 0.110
Si III	All	0.241 ± 0.040	2.190 ± 0.083
Si IV	1,000	0.136 ± 0.076	2.399 ± 0.159
Si IV	1,500	0.257 ± 0.036	2.212 ± 0.076
Si IV	2,000	0.351 ± 0.081	2.016 ± 0.170
Si IV	All	0.248 ± 0.044	2.209 ± 0.091
Si XIII	1,000	0.093 ± 0.065	2.663 ± 0.136
Si XIII	1,500	0.179 ± 0.085	2.657 ± 0.178
Si XIII	2,000	0.327 ± 0.069	2.326 ± 0.144
Si XIII	All	0.200 ± 0.055	2.549 ± 0.116

Table 6.2: Fit data for v_{90} velocities from the S series.

Ion	v_A (km s^{-1})	Slope (δ)	Intercept (γ)
Si I	1,000	0.191 ± 0.091	2.269 ± 0.189
Si I	1,500	0.273 ± 0.071	2.142 ± 0.148
Si I	2,000	0.333 ± 0.089	2.028 ± 0.185
Si I	All	0.266 ± 0.048	2.146 ± 0.100
Si II	1,000	0.097 ± 0.066	2.564 ± 0.138
Si II	1,500	0.226 ± 0.062	2.349 ± 0.129
Si II	2,000	0.239 ± 0.046	2.354 ± 0.096
Si II	All	0.187 ± 0.037	2.423 ± 0.078
Si III	1,000	0.062 ± 0.039	2.730 ± 0.081
Si III	1,500	0.194 ± 0.031	2.550 ± 0.065
Si III	2,000	0.248 ± 0.033	2.472 ± 0.069
Si III	All	0.168 ± 0.034	2.584 ± 0.071
Si IV	1,000	0.054 ± 0.033	2.767 ± 0.069
Si IV	1,500	0.190 ± 0.032	2.580 ± 0.068
Si IV	2,000	0.281 ± 0.060	2.415 ± 0.125
Si IV	All	0.175 ± 0.038	2.587 ± 0.080
Si XIII	1,000	0.001 ± 0.003	2.954 ± 0.007
Si XIII	1,500	-0.003 ± 0.007	3.153 ± 0.016
Si XIII	2,000	0.013 ± 0.011	3.244 ± 0.026
Si XIII	All	0.004 ± 0.076	3.117 ± 0.172

be true for all ions, and is not related to the SFR. Again the hottest gas plateaus at $v_w \approx 0.9 v_A$ similar to the S series.

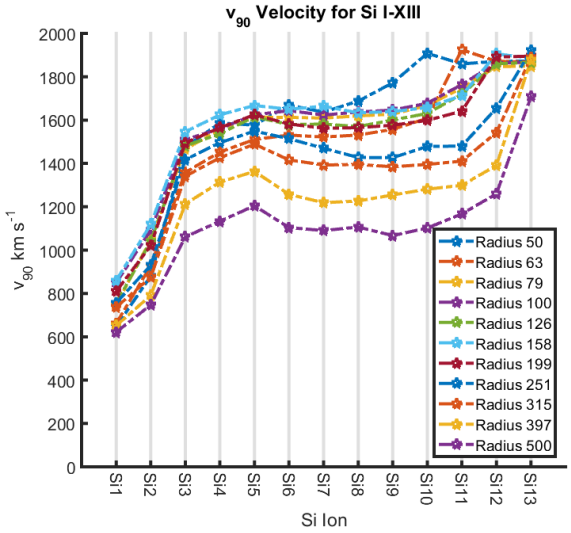

Figure 6.11: The v_{90} velocity for all Si ions for R series models with a SFR of 100 $M_\odot$ yr^{-1}. Radius is in pc.

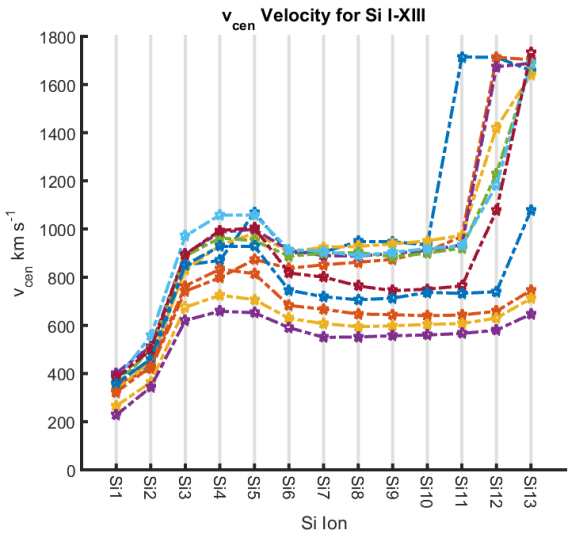

Figure 6.12: The $v_{\rm cen}$ velocity for all Si ions for R series models with a SFR of 100 $M_\odot$ yr^{-1}. Legend given in Figure 6.11.

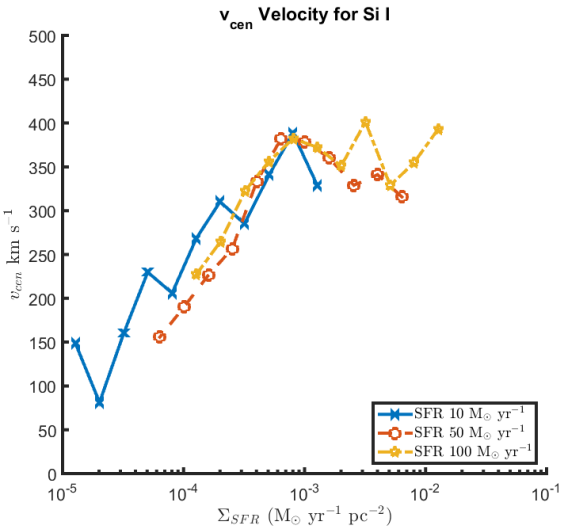

Figure 6.13: The $v_{\rm cen}$ velocity for Si I ions for all R series models.

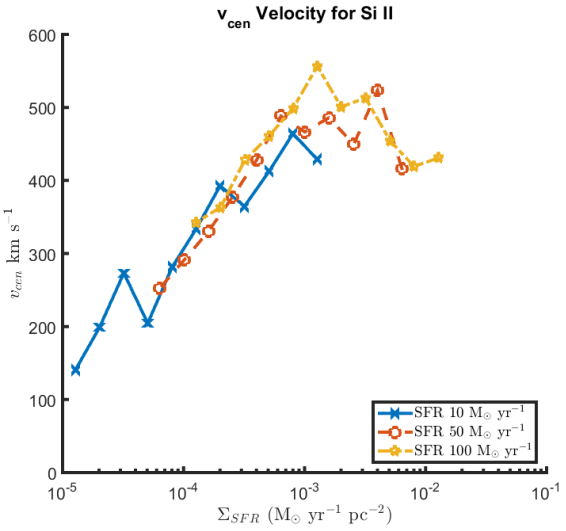

Figure 6.14: The $v_{\rm cen}$ velocity for Si II ions for all R series models.

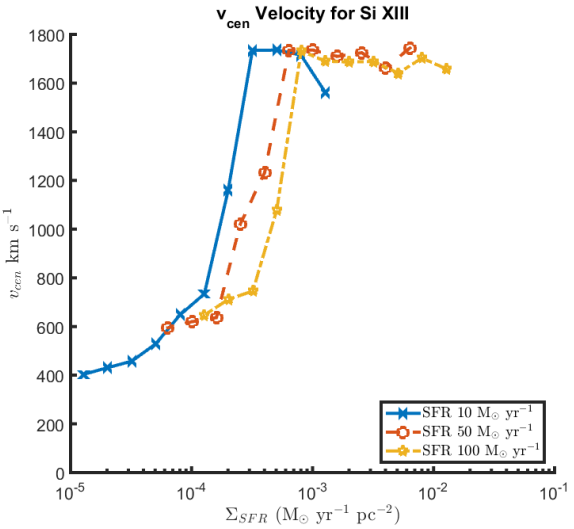

Figure 6.15: The $v_{\rm cen}$ velocity for Si XIII ions for all R series models.

CHAPTER 7: Discussion and Conclusion

7.1 Blowout Conditions

In Eq. 3.2, ξ measures the fraction of $\dot{E}$ converted into wind kinetic energy. Fujita et al. (2009) calculated $\xi = 0.45$ whereas my models found 0.67. The difference between my value of 0.67 and the analytic 0.45 can be attributed to two causes:

1. More starburst $\dot{E}$ goes into the kinetic energy of the wind because less energy is being expended to push through the inhomogeneous ISM.

2. More loaded mass ($\dot{M}$) ends up in filaments and is not accelerated to the terminal wind speed (§5), and therefore is not draining starburst energy.

My simulations cannot establish which of these dominates. The specific value of ξ may depend on parameters such as gas surface density (Creasey et al. 2013) and ambient ISM pressure (Mac Low & McCray 1988).

When considering the analytic wind speed (v_A from Eqn. 3.1), there is a transition ranging from escape velocity (v_e) to $1.5v_e$ where a wind can form but its evolution is set by cooling and resolution (Fig. 3.3 inset). Within this region my T4 models have faster winds while the corresponding T1 models sometimes have no wind. This difference arises because my T1 models lose more energy to cooling. Above the transition, cooling has no effect on blowout kinematics, in agreement with Fujita et al. (2009); moreover, increased resolution does not alter the measured wind speed.

Across the transition, higher resolution models form a GW at low v_A but the corresponding lower resolution models do not; e.g. both M2_33T4 and M2_33T1 formed a wind but the M1_33T4 and M1_33T1 models did not. But at a lower v_A the M2_43T4 model formed a wind while the M2_43T1, M1_43T4, and M1_43T1 did not despite having the same calculated v_A. This explains the absence of hot gas in the upper left panel of Figure 4.4. Higher resolution models form more filaments and dense cores, which decreases overall cooling efficiency. Lower resolution models over-estimate cooling losses. I did not run mid- or high-resolution models below the escape velocity, so cannot say if a starburst will blow out if the analytic wind speed is below v_e.

While my analysis was done at 1.5 Myr, my low resolution models ran to 4 Myr. If a blowout is absent at 1.5 Myr, it is also absent at 4 Myr. I conclude that an instantaneous starburst with constant mass and energy injection will reach terminal wind speed before 1.5 Myr.

7.2 Effect of the Radiative Cooling Limit

Numerical studies of starbursts with radiative cooling have focused on the warm wind plasma at $T > 10^4$ K (Strickland & Stevens 2000; Sutherland & Bicknell 2007; Cooper et al. 2008; Wünsch et al. 2011; Creasey et al. 2013; Melioli et al. 2013; Williamson et al. 2014), with a few addressing 100 K gas (Joung & Mac Low 2006; Fujita et al. 2009; Hill et al. 2012).

My results are consistent with those of Fujita et al. (2009) that T4 cooling suffices if one is interested only in kinematics and when $v_A > 1.5 v_e$; galactic wind formation depends only on mechanical luminosity of the starburst and associated mass loading from the stellar winds. Histograms in Figure 4.4 for T4 cooling resemble Figure 3 of Creasey et al. (2013), showing a "shelf" of Hα emission at 10^4 K. But Figure 4.4 with T1 cooling shows that the Creasey et al. (2013) "shelf" is an artifact of T4 cooling and I showed in §4.1 that the galactic wind composition changes significantly. The galactic wind is no longer dominated by Hα emitting gas; instead, in agreement with Bolatto et al. (2013), is dominated by neutral, molecular, and X-ray emitting gas.

The ratio of X-ray emission in the lower halo to that in the disk is unaffected by T1 cooling, but there is a change of 1-3 dex in the ratio of Hα emission.

7.3 Total Emission

For galaxies viewed edge on, total UV and X-ray emission can infer starburst properties directly such as total energy injection ($\dot{E}$) and total mass loading ($\dot{M}$), and by extension the thermalization efficiency (ϵ) and mass loading factor (β) (Strickland & Heckman 2009). While UV and X-ray emission generally increases with increasing $\dot{E}$, a low $\dot{M}$ will result in a hotter outflow that increases mid and hard X-ray emission, but decreases UV and soft X-ray emission. Higher ϵ increases total UV and X-ray emission for a constant β. But for low values of β the outflow gas has higher mid and hard X-ray emission and decreased UV and soft X-ray emission. Thus for the highest velocity winds there is a decrease in the total UV and soft X-ray emission and a corresponding increase from mid and hard X-ray gas.

From my models, the strongest Hα, hot UV and soft X-ray emission comes from models with wind velocity ~ 1500 km s^{-1}. Above this the total halo emission and Δ decrease indicating that the relationship between total emission and wind velocity given in Equation 4.1 only holds for Hα, hot UV and soft X-ray emission when wind velocities < 1500 km s^{-1}.

7.4 Filaments

Chapter 5 listed three origins of emitting filaments in my simulations. The longest filaments are from limb brightening and trace the bottom half of the expanding superbubble. Filaments from disrupting cold clouds or merging bubbles are thinner and shorter. Filaments from merged bubbles have higher densities and more optical emission (see Joung & Mac Low 2006), thus do not just arise from projection like limb brightened filaments.

My model resolution sufficed only to outline filaments. As Cooper et al. (2009) note, better resolution of filaments merely increases gas fragmentation and number of cloudlets, but does not change their kinematics. While Cooper et al. did not include thermal conduction in their simulations they noted that it should decrease cloud fragmentation by suppressing Kelvin-Helmholtz instabilities (Vieser & Hensler 2000, 2007). They concluded that it should increase cloud survival time despite increased mass lost by evaporation. They found that radiative cooling contributes to filament survival. They used MAPPINGS III (based on Sutherland & Dopita 1993), which only extends down to 10^4 K. If cooling below 10^4 K is allowed, more cloudlets would survive to transport cold gas into the galactic halo. While Cooper et al. (2009) considered the disruption of a cloud embedded in a galactic wind, an interesting extension of their work would be to model a cloud anchored to a mass loading region as explained in §5.2.

I find that the cold mass blown into the lower halo does not depend on starburst strength. Melioli et al. (2013) showed that denser packing of young clusters within a starburst leads to more filaments. A higher cluster density in the starburst region would lead to more contact regions between expanding bubbles, thus resulting in a higher number of filaments (see Chapter 5). This may be due to more contact between expanding bubbles. I show that filaments form along contacts and persist when attached to a mass loading anchor. There is a higher probability of contacts and anchors with many star forming complexes within the starburst. Most cold mass blown into the lower halo by the galactic wind is filamentary, only a bit remains in dense clouds that are not disrupted.

It is interesting that starburst luminosity does not alter the cold mass swept up by the galactic wind. This may indicate (Melioli et al. 2013) that the cold mass blown into the lower halo is set by the initial distribution of dense ISM clouds and the density of new star clusters within the starburst.

7.5 Multiple Overlaping Scaling Relationships

In Chapter 6 I generated synthetic absorption profiles for different ions in the galactic wind. Using these profiles I probed different temperature regimes of the outflow to study how the measured outflow velocity changed with SFR and $\Sigma_{\rm SFR}$. Based on arguments outlined in Section 3.2 the outflow velocity should not

depend on the SFR or $\Sigma_{\rm SFR}$, yet several surveys (Martin 2005; Rupke et al. 2005; Weiner et al. 2009; Chisholm et al. 2015) have found, using visible and UV absorption lines, that the velocity of the gas does scale with the SFR.

Using my synthetic absorption lines for ions found in warm outflow gas I also find that the velocity of the warm gas does scale with SFR but only up to $v_w \lesssim 0.8 v_A$ where the relationship flattens out. But if ions found in hot gas (i.e. Si XIII) are used then the outflow velocity does not scale with SFR and is constant at $v_w \approx 0.9 v_A$. In Table 6.1 I show scaling relations for Si I-IV and show that for $v_{\rm cen}$ velocities the scaling parameter (δ) increases with higher number ions, while Table 6.2 shows that for v_{90} velocities δ decreases with for higher number ions.

If I restrict my analysis of $v_{\rm cen}$ and v_{90} velocities to only $< 0.8 v_A$ (i.e. only models where the scaling relation is not flat, as in Figure 6.8) then I find $\delta \sim 0.3 - 0.35$ for all models independent of the v_A used. If I included all models regardless of v_A then I found $\delta \sim .25$. But this result does not come from a single scaling relationship but rather from multiple overlapping scaling relations. This can explain the different scaling relationships found by observations. For surveys that found $\delta \sim 0.35$ this would indicate that only starbursts with a high outflow velocity were included by a kinematical selection bias, while surveys that found $\delta \sim 0.25$ contained a mix of starbursts with different outflow velocities.

7.6 Conclusions

My five series of 3D simulations explore how a wide range of energy input, mass loading, SFR and $\Sigma_{\rm SFR}$ of a nuclear starburst affects galactic wind formation in an M82 sized galaxy. I also compare how gas cooling to 10^4 K (T4) vs. 10 K (T1) affects outflow emission and loaded mass. I conclude that:

1. The threshold for a blowout is when $v_A > 1.5 v_e$ with v_A defined by Equation 3.1. Below this limit the possibility of a blowout depends on the cooling and grid resolution used. Above this limit cooling and grid resolution do not affect wind kinematics.

2. For T4 cooling, most lower halo gas is in the warm regime corresponding to peak Hα emission. But for T1 cooling, lower halo mass is predominantly neutral, cold and X-ray emitting, not warm Hα emitting gas.

3. T1 cooling of a sufficiently powerful nuclear starburst does not change galactic wind kinematics, confirming Fujita et al. (2009)

4. X-ray emission from edge-on starburst galaxies trace the strength of a galactic wind because the ratio halo/disk emission correlates with galactic wind terminal speed.

5. Total X-ray emission can infer the thermalization efficiency and mass loading factor of the starburst.

6. Emission from cold gas in the lower halo is 4-8 dex fainter than from cold gas in the disk.

7. The mass of cold gas blown into the lower halo does not depend on starburst strength. It may depend on the ISM initial state and the number of star-forming complexes (Melioli et al. 2013).

8. Bright optical filaments form in 3 ways. Observed filaments can be any combination of:

   (a) Limb brightened, shocked edge of the superbubble.

   (b) A cool dense cloud ablated by the wind.

   (c) Merged bubbles that rise from the starburst.

9. Filaments move much slower than the wind. Filaments embedded in a galactic wind of $400 < v < 2000$ km s^{-1} attain $\lesssim 50$ km s^{-1} for the densest material and $200 < v < 500$ km s^{-1} for ablata.

10. The densest filaments form molecular and "warm" absorption line profiles that are asymmetric with long tails to higher velocities from accelerating ablata. They resemble those observed in starbursts.

11. The velocity of warm and cold gas as measured by absorption lines scales as $v_w \propto \mathrm{SFR}^{\delta}$ for $v_w < 0.8 v_A$. For $v_w > 0.8 v_A$ the scaling relation is flat with no dependence on SFR. The value of δ depends on the ion used, with a higher value for increasing ionization.

REFERENCES

Aguirre, A., Hernquist, L., Schaye, J., et al. 2001, ApJ, 560, 599

Arribas, S., Colina, L., Bellocchi, E., Maiolino, R., & Villar-Martín, M. 2014, A&A, 568, A14

Barker, S., de Grijs, R., & Cerviño, M. 2008, A&A, 484, 711

Bland, J., & Tully, B. 1988, Nature, 334, 43

Bland-Hawthorn, J. 1995, PASA, 12, 190

Bogacki, P., & Shampine, L. 1989, Applied Mathematics Letters, 2, 321

Bolatto, A. D., Warren, S. R., Leroy, A. K., et al. 2013, Nature, 499, 450

Cecil, G., Bland-Hawthorn, J., & Veilleux, S. 2002, ApJ, 576, 745

Cecil, G., Bland-Hawthorn, J., Veilleux, S., & Filippenko, A. V. 2001, ApJ, 555, 338

Chen, Y.-M., Tremonti, C. A., Heckman, T. M., et al. 2010, AJ, 140, 445

Chevalier, R. A., & Clegg, A. W. 1985, Nature, 317, 44

Chisholm, J., Tremonti, C. A., Leitherer, C., Chen, Y., & Wofford, A. 2016, ArXiv e-prints, arXiv:1601.05090

Chisholm, J., Tremonti, C. A., Leitherer, C., et al. 2015, ApJ, 811, 149

Cooper, J. L., Bicknell, G. V., Sutherland, R. S., & Bland-Hawthorn, J. 2008, ApJ, 674, 157

—. 2009, ApJ, 703, 330

Creasey, P., Theuns, T., & Bower, R. G. 2013, MNRAS, 429, 1922

Dahlem, M. 1997, PASP, 109, 1298

Dalgarno, A., & McCray, R. A. 1972, ARA&A, 10, 375

Dawson, J. R. 2013, PASA, 30, 25

Devine, D., & Bally, J. 1999, ApJ, 510, 197

Einstein, A. 1905, 322, 132

Fabbiano, G. 1988, ApJ, 330, 672

Fabbiano, G., Heckman, T., & Keel, W. C. 1990, ApJ, 355, 442

Field, G. B. 1965, ApJ, 142, 531

Freyer, T., Hensler, G., & Yorke, H. W. 2003, ApJ, 594, 888

Fujita, A., Martin, C. L., Mac Low, M.-M., New, K. C. B., & Weaver, R. 2009, ApJ, 698, 693

Heckman, T. M., Armus, L., & Miley, G. K. 1990, ApJS, 74, 833

Heckman, T. M., Dahlem, M., Lehnert, M. D., et al. 1995, ApJ, 448, 98

Heckman, T. M., Lehnert, M. D., & Armus, L. 1993, in Astrophysics and Space Science Library, Vol. 188,

The Environment and Evolution of Galaxies, ed. J. M. Shull & H. A. Thronson, 455

Heckman, T. M., Lehnert, M. D., Strickland, D. K., & Armus, L. 2000, ApJS, 129, 493

Heckman, T. M., Borthakur, S., Overzier, R., et al. 2011, ApJ, 730, 5

Hill, A. S., Joung, M. R., Mac Low, M.-M., et al. 2012, ApJ, 750, 104

Ho, I.-T., Medling, A. M., Bland-Hawthorn, J., et al. 2016, MNRAS, 457, 1257

Inoue, T., Inutsuka, S.-i., & Koyama, H. 2006, ApJ, 652, 1331

Jones, T., Stark, D. P., & Ellis, R. S. 2012, ApJ, 751, 51

Joung, M. K. R., & Mac Low, M.-M. 2006, ApJ, 653, 1266

Kim, C.-G., & Ostriker, E. C. 2015, ApJ, 802, 99

Koyama, H., & Inutsuka, S. 2002, ApJL, 564, L97

Kramida, A., Yu. Ralchenko, Reader, J., & and NIST ASD Team. 2015, NIST Atomic Spectra Database (ver. 5.3), [Online]. Available: `http://physics.nist.gov/asd` [2016, February 2]. National Institute of Standards and Technology, Gaithersburg, MD.

Kwok, S. 2007, Physics and Chemistry of the Interstellar Medium (University Science Books)

Leitherer, C., Schaerer, D., Goldader, J. D., et al. 1999, ApJS, 123, 3

Mac Low, M.-M., & McCray, R. 1988, ApJ, 324, 776

Mac Low, M.-M., McCray, R., & Norman, M. L. 1989, ApJ, 337, 141

Mandal, J., & Deshpande, S. 1994, Computers & Fluids, 23, 447

Martin, C. L. 2005, ApJ, 621, 227

Martin, C. L., Shapley, A. E., Coil, A. L., et al. 2012, ApJ, 760, 127

Mathis, J. S., Whitney, B. A., & Wood, K. 2002, ApJ, 574, 812

Mazzotta, P., Mazzitelli, G., Colafrancesco, S., & Vittorio, N. 1998, A&AS, 133, 403

McCray, R., & Kafatos, M. 1987, ApJ, 317, 190

McMillan, P. J. 2011, MNRAS, 414, 2446

Melioli, C., de Gouveia Dal Pino, E. M., & Geraissate, F. G. 2013, MNRAS, 430, 3235

Miyamoto, M., & Nagai, R. 1975, PASJ, 27, 533

Raymond, J. C., Cox, D. P., & Smith, B. W. 1976, ApJ, 204, 290

Rubin, K. H. R., Prochaska, J. X., Koo, D. C., et al. 2014, ApJ, 794, 156

Rupke, D. S., Veilleux, S., & Sanders, D. B. 2002, ApJ, 570, 588

—. 2005, ApJS, 160, 115

Rybicki, G. B., & Lightman, A. P. 1986, Radiative Processes in Astrophysics

Sarazin, C. L. 1986, Reviews of Modern Physics, 58, 1

Scarlata, C., & Panagia, N. 2015, ApJ, 801, 43

Schreier, F. 2011, Journal of Quantitative Spectroscopy and Radiative Transfer, 112, 1010

Shapiro, P. R., Giroux, M. L., & Babul, A. 1994, ApJ, 427, 25

Shopbell, P. L., & Bland-Hawthorn, J. 1998, ApJ, 493, 129

Silich, S. A., Franco, J., Palous, J., & Tenorio-Tagle, G. 1996, ApJ, 468, 722

Stone, J. M., Gardiner, T. A., Teuben, P., Hawley, J. F., & Simon, J. B. 2008, ApJS, 178, 137

Strickland, D. K., & Heckman, T. M. 2009, ApJ, 697, 2030

Strickland, D. K., Heckman, T. M., Weaver, K. A., Hoopes, C. G., & Dahlem, M. 2002, ApJ, 568, 689

Strickland, D. K., Ponman, T. J., & Stevens, I. R. 1997, A&A, 320, 378

Strickland, D. K., & Stevens, I. R. 2000, MNRAS, 314, 511

Suchkov, A. A., Balsara, D. S., Heckman, T. M., & Leitherer, C. 1994, ApJ, 430, 511

Suchkov, A. A., Berman, V. G., Heckman, T. M., & Balsara, D. S. 1996, ApJ, 463, 528

Sutherland, R. S., & Bicknell, G. V. 2007, ApJS, 173, 37

Sutherland, R. S., & Dopita, M. A. 1993, ApJS, 88, 253

Tanner, R., Cecil, G., & Heitsch, F. 2016, ApJ, 821, 7

Tenorio-Tagle, G. 1979, A&A, 71, 59

Tenorio-Tagle, G., Silich, S. A., Kunth, D., Terlevich, E., & Terlevich, R. 1999, MNRAS, 309, 332

Veilleux, S., Cecil, G., & Bland-Hawthorn, J. 2005, ARA&A, 43, 769

Veilleux, S., Cecil, G., Bland-Hawthorn, J., et al. 1994, ApJ, 433, 48

Vieser, W., & Hensler, G. 2000, Ap&SS, 272, 189

—. 2007, A&A, 472, 141

Walter, F., Weiss, A., & Scoville, N. 2002, ApJ, 580, L21

Watson, M. G., Stanger, V., & Griffiths, R. E. 1984, ApJ, 286, 144

Weaver, R., McCray, R., Castor, J., Shapiro, P., & Moore, R. 1977, ApJ, 218, 377

Weiner, B. J., Coil, A. L., Prochaska, J. X., et al. 2009, ApJ, 692, 187

Williamson, D. J., Thacker, R. J., Scannapieco, E., & Brüggen, M. 2014, MNRAS, 441, 389

Wofford, A., Leitherer, C., & Salzer, J. 2013, ApJ, 765, 118

Wolfire, M. G., Hollenbach, D., McKee, C. F., Tielens, A. G. G. M., & Bakes, E. L. O. 1995, ApJ, 443, 152

Wünsch, R., Silich, S., Palouš, J., Tenorio-Tagle, G., & Muñoz-Tuñón, C. 2011, ApJ, 740, 75